

NIELS BOHR INSTITUTE
UNIVERSITY OF COPENHAGEN



PhD thesis

Peter Dahl Nissen

Spin Qubits in GaAs Heterostructures and Gating of InAs Nanowires for Low- temperature Measurements

Academic advisor: Prof. Jesper Nygård

Submitted: 31/10/12



Spin Qubits in GaAs Heterostructures and Gating of InAs Nanowires for Low-temperature Measurements

PH.D. THESIS

Author:
Peter Dahl NISSEN

Academic advisor:
Prof. Jesper NYGÅRD

NIELS BOHR INSTITUTE
FACULTY OF SCIENCE
UNIVERSITY OF COPENHAGEN
DENMARK

October 2012

*Spin Qubits in GaAs Heterostructures and Gating of InAs Nanowires for
Low-temperature Measurements*

Ph.D. Thesis

© 2012 by Peter Dahl Nissen

e-mail: pdn@nano.ku.dk

Niels Bohr Institute

Nano-Science Center

Faculty of Science

University of Copenhagen

Universitetsparken 5

DK-2100 Copenhagen Ø

Denmark

Resumé

“Spintronik” betegner elektronik baseret på kontrol over elektronens spin i stedet for dens ladning, og vil således have elektronens spin som informationsbærer i stedet for ladningen. Spin-kvantebit’en, én af de fremmeste kandidater i kapløbet om at bygge en kvantecomputer i stor skala, er en sådan komponent. Forskning i konstruktion, manipulation og kobling af spin-kvantebits spænder over mange materialesystemer i jagten på ét, hvor kravene til hurtig kontrol over og lang kohærenstid for spintilstanden kan kombineres med en effektiv kobling mellem kvantebits.

Denne afhandling beskriver elektriske målinger på to materialer, der i øjeblikket er med i fronten af spin-kvantebit feltet, nemlig InAs nanotråde og GaAs/AlGaAs heterostrukturer.

For InAs nanotråde undersøges forskellige gating-geometrier med det formål at definere stabile kvantepunkter i nanotrådene ved mK temperaturer.

Tre typer af lokale gate analyseres; tynde gates (50-100 nm) placeret oven på eller under nanotrådene, og brede gates der overlapper grænsefladerne mellem nanotråd og source- og drain-elektroder. Det vises, at påtrykning af negative potentialer på de lokale gate-elektroder inducerer justerbare barrierer på op til 0.25 eV. Udfra temperaturafhængigheden af ledningsevnen bestemmes barrierehøjden som funktion af gatespænding. Over- og under-gates ligner hinanden med hensyn til elektrostatiske koblinger ($\sim 0.1\text{--}0.2\text{ eV/V}$) og tærskelspændinger for barriereinduktion ($V_g \sim -1\text{ to } -2\text{ V}$), men lavtemperatur-gatemålinger tyder på, at prøvestabilitet kan være påvirket af forskellene i fabrikationen mellem de to gate-geometrier.

For GaAs heterostrukturer undersøges to nye idéer til at realisere spin-kvantebits i kvantepunkter.

Først inkorporeres ferromagnetisk metal i gates’ne, så de samtidigt fungerer som mikromagneter, der leverer gradienter i det magnetiske felt. Der demonstreres fuld kontrol over elektronantallet i kvantepunkterne med den magnetiske gate-struktur, kombineret med en magnetfeltsgradient på $\sim 25\text{ mT}$ bestemt ved elektrisk dipol spin resonans (EDSR) målinger. EDSR-mekanismen kunne ikke fastlægges med sikkerhed.

For samme prøve undersøges muligheden for kvantebit-funktion i multi-elektron kvantepunkter med én enkelt uparret elektron — spinkohærens for kvantebits i dette regime kunne drage fordel af skærmningseffekter. Det konkluderes at simpel, vekslende spin-fyldning ikke blev fulgt. Endvidere viser målinger af exchange-opsplitningen, J , to magnetfeltafhængige overgange, der fører til ophævelse af Pauli spin-blokade. Dette er ligeledes i uoverensstemmelse med den simpleste model for elektronspinfyldningen i kvantepunkterne. Effekten af magnetfeltsgradienterne fra den magnetiske gatestruktur kunne spille en rolle i forhold til de observerede effekter i multi-elektron dobbelt-kvantepunkter.

Abstract

“Spintronics” is used to describes electronics based on control over the spin of the electron rather than the charge; instead of having the charge as the carrier of information, the electrons spin-state should be the target for control and detection in a given device. The spin qubit, one of the contenders in the race to build a large-scale quantum computer, is such a component, and research aiming to build, manipulate and couple spin qubits is looking at many materials systems to find one where the requirements for fast control and long coherence time can be combined with efficient coupling between distant qubits. This thesis presents electric measurement on two of the materials systems currently at the forefront of the spin qubit race, namely InAs nanowires and GaAs/AlGaAs heterostructures

For the InAs nanowires we investigate different gating geometries towards the goal of defining stable quantum dots in the nanowire at mK temperatures.

Three types of local gates are analyzed; narrow gates (50–100 nm) located on top of or below the nanowire, and wide gates overlapping the interfaces between nanowire and source and drain electrodes. We find that applying negative potentials to the local gate electrodes induces tunable barriers of up to 0.25 eV. From the temperature dependence of the conductance, the barrier height is extracted and mapped as a function of gate voltage. Top and bottom gates are similar to each other in terms of electrostatic couplings (lever arms ~ 0.1 – 0.2 eV/V) and threshold voltages for barrier induction ($V_g \sim -1$ to -2 V), but low temperature gate sweeps suggest that device stability could be affected by the differences in device processing for the two gate geometries.

For the GaAs heterostructure we investigate two new ideas for realizing spin qubits in lateral quantum dots.

First, we incorporate ferromagnetic metal in the depletion gates making them double as micro-magnets supplying magnetic field gradients allowing spin qubit operation. We demonstrate full tunability of the electron occupation with the magnetic gate structure, combined with a magnetic field gradient of ~ 25 mT determined by electric dipole spin resonance (EDSR). The EDSR mechanism could not be determined with certainty.

For the same device, we investigate using single, unpaired electron spins in multi-electron quantum dots for spin qubits; qubit coherence in this regime could benefit from screening effects. We find that simple, alternating spin filling is not followed. Furthermore, measurement of the exchange splitting, J , indicate two magnetic field dependent transitions lifting spin blockade which is likewise inconsistent with the simplest model for spin filling.

The effect of the magnetic field gradients from the micro-magnet could play a role in the observed differences between the multi- and the few-electron double dots.

0.1 Preface

Firstly, I would like to thank my advisor Prof. Jesper Nygård for guidance throughout the three years and for helping to make my Ph.D. an overall very enjoyable experience. With his relaxed being as the leader of a research group filled with enjoyable colleagues, he has set the scene for a very pleasant work environment.

I would also like to thank post docs Thomas Sand Jespersen and Kasper Grove-Rasmussen for their willingness to help with more or less any problem or question that I would come to them with, as well as for taking an interest in the measurements and their analysis.

I've enjoyed many conversations about nanowires, football and tons of other stuff with my fellow Ph.D. students Shivendra Upadhyay, Peter Krogstrup and Morten Hannibal Madsen and I hope that we keep bumping into each other despite the office rearrangements. Further, I'm grateful to Peter Krogstrup, Morten Hannibal Madsen and Claus Sørensen for growing the nanowires I have been using for my experiments. I would also like to thank Claus, Nader and Morten for keeping all the facilities in the lab running smoothly.

Much of the work described in this thesis was done during eight intense months spent at Prof. Charles Marcus's lab at Harvard University. I would like to thank him for inviting me in, giving me the opportunity to learn all the spin qubit tricks from some of the best in the business. At Harvard, I worked with post doc Javad Shabani, who helped make the many hours in lab a fun experience by being a straight-up nice guy - easygoing even when returning to lab at nine in the morning after taking on a 3 am e-beam session.

I would also like to thank the rest of the Marcus Lab gang for all the time we spent in the lab, and to a lesser extent outside the lab. I wish you all all the best in your future careers.

Looking forward, I'm happy to have gotten the opportunity to dive further into the experiments on spin qubits in the truly awesome new lab in Copenhagen. Thanks to Charlie, Jesper and Karsten, the heads of the new Center for Quantum Devices (QDev), we now have no excuse for not doing the coolest (no pun intended) experiments within the field of spin qubits. I'm even more excited that we did not only get a lot of new equipment, but also some new colleagues in form of Ferdinand, Andrew and Willy who decided to make the move to Copenhagen - not only are they extremely capable, they are also very pleasant people to share a lab with. I hope I can help make them feel at home in Copenhagen.

I'm grateful for the support from family and friends, but most of all the enormous patience and love Stine has shown me throughout the last three years, and especially during the last Ph.D. "cramps". I'm looking forward to repaying you.

Contents

0.1	Preface	vi
1	Introduction	1
1.1	Nanoscale electronics: When size matters	1
1.2	New materials: Confinement and control	1
1.3	Spintronics and quantum computing	2
1.4	Organization of this thesis	4
2	GaAs/AlGaAs heterostructures and InAs nanowires for spin qubits	5
2.1	InAs nanowires	5
2.1.1	Growth and electronic characteristics	5
2.2	GaAs/AlGaAs heterostructures	8
2.3	Quantum dots: Electrons in a box	9
2.3.1	Double quantum dots	12
2.3.2	Spin states in two-electron double dots and Pauli spin blockade	17
2.4	Decoherence and relaxation	19
2.4.1	Interactions with nuclear spins: Overhauser field and dynamics	22
2.4.2	Spin-orbit coupling	26
2.4.3	Voltage noise	29
2.5	Spin qubits in quantum dots	30
2.5.1	Single-spin qubit: Loss-DiVincenzo qubit	30
2.5.2	Two-electron qubit: S - T_0 qubit	32
2.5.3	Three-electron qubit: Exchange-only qubit	33
2.5.4	Two-qubit operation and gates	33
3	Device fabrication and measurement setup	35
3.1	InAs nanowire device fabrication and measurement	35
3.1.1	InAs nanowire device fabrication	35
3.1.2	InAs nanowire measurement setup	49
3.2	GaAs/AlGaAs device fabrication and measurement	52
3.2.1	GaAs/AlGaAs heterostructure device fabrication	52
3.2.2	GaAs/AlGaAs 2DEG measurement setup	53

4	Comparing gate geometries for electrostatic barriers in InAs nanowires	55
4.1	Introduction	55
4.2	Induction of barriers by local gates	56
4.2.1	Trends in temperature dependence of conductance vs gate voltage	59
4.2.2	Thermal activation over barrier: Extraction of barrier height vs V_g	60
4.3	Gate geometry and low temperature stability	66
5	Confined electron spins in GaAs/AlGaAs heterostructure 2-DEG QDs	69
5.1	Preface	69
5.2	Introduction	69
5.3	Two-electron double quantum dots and magnetic field gradients with ferro-magnetic gates	70
5.3.1	Magnetic field gradients from magnetic gate structure	70
5.3.2	Formation of few-electron double dots and spin blockade	74
5.3.3	Spin blockade lifting with electric dipole spin resonance	76
5.4	Multi-electron double quantum dots for singlet-triplet spin qubits	81
5.4.1	Introduction	81
5.4.2	Pauli spin blockade in the multielectron regime	82
5.4.3	Measurement of exchange energy vs detuning	84
5.4.4	Dephasing of the separated singlet for T_2^* estimate	87
6	Conclusions and perspectives	91
6.1	Conclusions for the InAs nanowire studies	91
6.2	Conclusions for the GaAs/AlGaAs studies	91
6.3	Outlook	92
6.3.1	InAs nanowire studies	92
6.3.2	GaAs heterostructure studies	93
6.3.3	Perspectives for InAs nanowire and GaAs heterostructure spin qubits	93
A	Construction of a high frequency measurement setup	95
A.1	Cryogenic wiring	96
A.1.1	DC wiring	96
A.1.2	High frequency wiring	97
A.2	Reflectometry readout	105
A.3	Printed circuit board sample holders	108
A.4	List of manufacturers	109
A.4.1	Attenuators	109
A.4.2	RF parts, passive electronics, SMC	112
A.4.3	Printed Circuit Boards	115
	Bibliography	117

Chapter 1

Introduction

1.1 Nanoscale electronics: When size matters

The realm of nanoscale electronics is in fact already reality in our current computer processors and has been for some years; the Ivy Bridge microprocessor from Intel, released on the market in the spring of 2012, is based on 22 nm transistors, see Fig. 1.1, and already in 2003 a 90 nm transistor was implemented. Furthermore, 14 nm and 10 nm processors are already on the road map for 2013 and 2015, respectively [1]. In this sense, nanoscale electronics is “simply” an extension of current technology to a nanometer scale via top-down processing.

However, what the above mention of a 22 nm transistor does not reveal is that by scaling existing technologies to extreme degrees, the dominating physics of the devices changes in two ways. Firstly, as the overall size, ℓ , of an object shrinks the surface-to-volume ratio changes as ℓ^{-1} , to the point where the properties of the surface of the object dominates those of the bulk¹. Secondly, quantum mechanical effects begin to play a role, such as tunneling of electrons through insulating material.²

From one perspective, such as established technologies, these emerging properties can be a nuisance, but from the perspective of fundamental science and emerging technologies these properties form a playground full of new opportunities.

1.2 New materials: Confinement and control

Manifestations of quantum mechanics in electron transport as mentioned above have been investigated in condensed matter physics as part of the field called *mesoscopic* physics since the 1980'ies [2]. The experimental system used in many of these experiments was a two-dimensional electron gas (2-DEG), where (when cooled to \sim mK temperatures)

¹If one can speak of “the bulk” at this scale.

²In the case of the 22 nm transistor both of these effects played a role in the design, as this is the first microprocessor transistor to use a wrap-gate geometry in order to suppress the leakage current in the off state, achieving faster switching and/or lower power consumption [1].

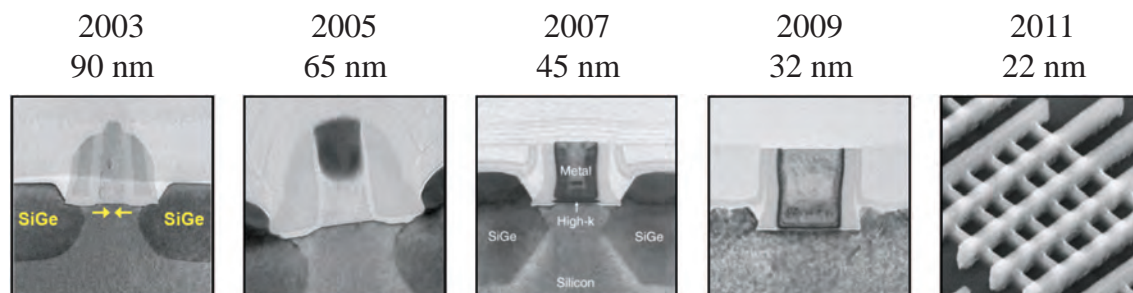


Figure 1.1: Images showing the development in the size of Intel’s transistors from 2003 to 2011. Every second year a still smaller transistor has been presented and in 2011 the 22 nm transistor was presented, breaking with the usual planar geometry. Adapted from [1]

electrons move can move along a heterostructure interface without scattering, thus keeping their phase coherence and allowing for interference effects to be observed. With the 2-DEG it also became possible to define structures further reduced in dimensions, such as one-dimensional channels and islands of electrons small enough to observe the effect of the electrons quantized charge [3, 4].

Over the last ~ 30 years inherently low-dimensional/nanoscale structures have been added to the mesoscopic toolbox; one-dimensional structures such as carbon nanotubes [5] and nanowires/nanowhiskers/nanorods[6, 7]; and zero dimensional structures such as Buckminsterfullerenes [8] and nanocrystal quantum dots [9].

Among these systems the nanowires and nanocrystal quantum dots are the most flexible, since the growth of these materials is under precise control in terms of material composition and structure, giving rise to structures with a broad range of physical properties.

The flexibility of nanowires in terms of material interfaces that can be realized makes these structures extremely interesting both from an electronic and opto-electronic point of view [10–14], and building on progress in semiconductor nanowire growth, concerning *e.g.* crystallinity [15] and composition [16–20], several advances have been made towards the use of nanowires for future generation electronics [21–23], and as low dimensional laboratories for studying quantum physics [24–26].

1.3 Spintronics and quantum computing: Spin as information carrier

The developments on the materials side have pushed the limits for the degree of control attainable in low-temperature experiments to the point where isolation of and control over single electrons is somewhat commonplace.

Even before this level of control was realized in experiments, suggestion for how to utilize it towards various ends sprouted during the 90’ies. In particular, some of these suggestions presented the idea of basing electronics on control over the spin of the electron

rather than the charge; now, the electrons spin state should be the carrier of information instead of the charge [27–30]. The term “spintronics” was coined to describe this new field.

Spintronics overlaps somewhat with another rather new field that was inspired by the visionary thoughts of Richard Feynman and others [31], namely quantum computing [32].

A quantum computer is a form of computer that bases its operation on coherent manipulation of quantum mechanical two-level systems, which the electron spin is a prime example of. Each two-level system, dubbed *qubit*, short for quantum bit, in analogy to the classical computer bit, can assume any superposition occupation of the two levels (1 *and* 0) in contrast to the classical, digital bit (1 *or* 0).

Different schemes for quantum computing exist, of which the quantum circuit model [32, 33] is the most widely used. It is beyond the scope of this thesis to explain the different schemes beyond mentioning them here; adiabatic quantum computing [34], cluster state (or one-way) quantum computing [35, 36] and topological quantum computing [37, 38]

Computation in a circuit quantum computer is based on series of single- and two-qubit operations called gates, changing the state of the target qubit in a set way or depending on the state of a control qubit, respectively [32].

What makes the quantum computer desired is theoretical results showing that a quantum computer will outperform a classical computer in solving certain problems thought to be intractable on a classical computer, due to an exponential (x^n) scaling in computational resources with the complexity (n bits input) of the problem [32]. The quantum computer will be able to solve these problems with only polynomial (n^x) resources making the process feasible [32]. The prime examples of problems for which the quantum computer will outperform the classical computer are factoring of integers by Shor’s algorithm [39] and searching unsorted databases by Grover’s algorithm [40].

In principle, any two-level quantum system can be used as a qubit, and a staggering number of different systems spanning a number of different fields of physics have been proposed and investigated; several reviews discuss the various approaches [33, 41, 42] comparing their advantages and disadvantages with respect to fulfilling the requirements for quantum computing [33, 42]. To give a sense of the width of the field an non-exhaustive list of different “flavors” in quantum computing is given below, with more details on the realizations within the field of solid state physics that the experiments in this thesis belongs to,

- Optical quantum computing (measurement based/cluster state quantum computing) [43]
- Trapped ions [44, 45] or neutral atoms [46, 47] in optical lattices
- Cavity quantum electrodynamics systems [48, 49]
- Liquid-state NMR on molecule ensembles [50–53]

- Superconductor-based quantum computers using Josephson junctions [54]
- Quantum computing with defects in semiconductors and insulators [55], such as³
 - Nitrogen-vacancy (NV) centers in diamond [56]
 - Various defect states in silicon carbide (SiC) [57]
 - Phosphorous implanted in silicon [58, 59] and
 - Rare-earth ions (*e.g.* ER^{3+}) in various insulators (*e.g.* CaWO_4) [60]
- Electron or hole spins in semiconductor quantum dots [28, 61–63], such as
 - Electrostatically defined quantum dots in GaAs/AlGaAs heterostructure, Si/SiGe heterostructures [64], InAs nanowires [25], Ge/Si core/shell nanowires [65]
 - Self-assembled quantum dots, optically controlled [66, 67].

The width of the field tells that the experimental realization of quantum computing is still in its infant days. Although there is a large spread in the progress within the different fields, no one system is regarded as the favorite for implementation of a large scale quantum computer; to this day the record in factorization is held by a optical quantum computer that recently factorized 21 [68].

1.4 Organization of this thesis

In this thesis I describe electrical transport measurements on InAs nanowires and GaAs 2-DEGs. These experiments represent steps on very different stages towards realizing spin qubits in InAs nanowires and GaAs heterostructures.

In Chapter 2 the relevant background and general theory in relation to the experiments is presented

In Chapter 3 details of sample fabrication and measurement setups are described

In Chapter 4 two geometries for local gating of InAs nanowires are compared towards the end of defining quantum dot for low-temperature experiments.

In Chapter 5 initial studies for two variations of spin qubits in GaAs 2-DEG quantum dots are presented

³Out of these, NV and SiC systems are remarkable compared to other solid state qubits in that they can be operated at room temperature [56, 57].

Chapter 2

GaAs/AlGaAs heterostructures and InAs nanowires for spin qubits

2.1 InAs nanowires

2.1.1 Growth and electronic characteristics

¹ The InAs nanowires examined in this thesis were, prior to this thesis, grown at the University of Copenhagen using molecular beam epitaxy (MBE). MBE is a ultra high vacuum (UHV) growth technique, where the wire grows from a catalyst nanoparticle (usually gold) placed on a suitable substrate, upon addition of the nanowire material from the gas phase. Detailed descriptions of the growth process can be found in references [70–72].

An InAs growth substrate is loaded into the MBE chamber via a load-lock, in order to maintain a high vacuum of $\sim 10^{-11}$ torr. In a constant flux of elemental As, the substrate is heated to $\sim 550^\circ\text{C}$ before ~ 1 nm gold is deposited by thermal evaporation of solid gold followed by thermal annealing. Due to the high temperature of the InAs substrate, the gold forms small droplets. The temperature of the substrate is lowered to the desired growth temperature ($\sim 430^\circ\text{C}$). By introducing a gas flux of In by thermal evaporation of solid elemental In, deposition of In and As takes place at the interface between the gold nanoparticle and the solid substrate, initiating the growth of the nanowire. The gold particle thus acts as a catalyst for growth of the nanowire, and also determines the width of the nanowire.

The nanowire will continue to grow as more In and As deposits at the interface of the nanowire and the gold particle, due to a continuous influx of In and As from the gas phase and for In also from surface diffusion (See figure 2.1).

Due to the size of the nanowire, the favored crystal structure of the nanowire may be an other than that of a bulk crystal. For bulk InAs only zincblende (*zb*) structure is seen,

¹Parts of this section have been adapted with minor changes from the authors Master's thesis [69]

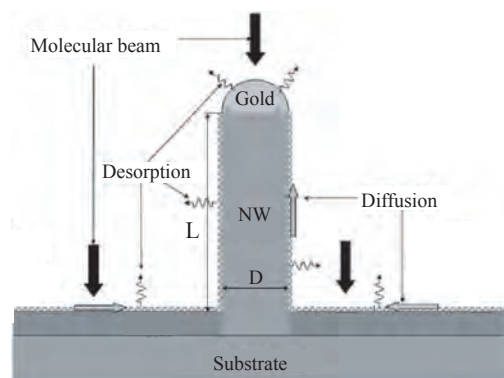


Figure 2.1: Schematic of gold catalyzed MBE growth of nanowires. The nanowire grows at the interface between gold nanoparticle and wire. The semiconductor material being incorporated into the growing wire comes both from the molecular beam and from surface diffusion. Adapted from [73] with slight modifications.

whereas for nanowires wurtzite wz structure is more common [74]. Previous analysis of the InAs nanowires grown at the University of Copenhagen show that the wires often display alternating perfect cubic zb structure and perfect hexagonal wz structure [70]. Both pure wz [75], alternating wz and zb structure [16] and pure zb structure [76] in InAs nanowires are possible depending on the growth conditions.

The nanowire grows along the wz [0001] (hexagonal) axis, which corresponds to the zb [111] (cubic) direction. Along this axis, wz has an ABABAB stacking whereas zb has ABCABC [77]. The nanowires examined in this thesis have diameters of $\sim 80\text{--}100$ nm and stacking fault densities $\sim 30\ \mu\text{m}^{-1}$, dominated by wz structure. The stacking faults can be considered as a zb stacking sequence inserted into the wz crystal. The final length of the nanowire will mainly be determined by the growth time, and can be many micrometers, see Fig. 2.2 (b).

The electronic properties for bulk InAs in terms of band gap, effective electron mass, spin-orbit coupling and g -factor are well established [78]. But for nanowires very little is known about the effects of the geometrical confinement on the band structure of zb InAs. In addition to this the crystal structure can, as described above, have partly or fully changed to wz - a structure for which very little is known for InAs. Two recent theoretical papers [79, 80] deal with the structural and electronic properties of the wz phase of InAs, and estimate an increase of the band gap of ~ 55 meV compared to the value of zb InAs of 0.417 eV at cryo temperatures [78]. The spin-orbit coupling is estimated to ~ 0.333 eV compared to the value of 0.39 eV in zb InAs at cryo temperatures [78]. The spin-orbit coupling estimate is, though, found in relation to calculations that lead to *negative* band gap for wz InAs, making it questionable. Importantly, none of the calculations take the finite size of the nanowire crystal into account, and the exact values reported should therefore not be expected to apply to nanowires.

Due to this lack of knowledge of the properties of the wire and the wz structure, reference

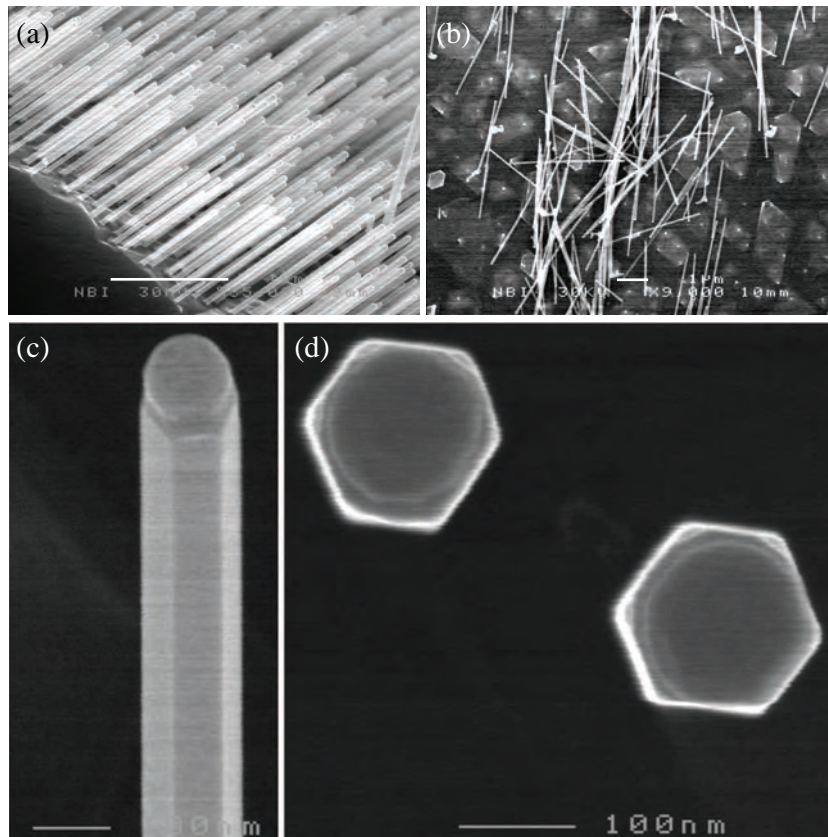


Figure 2.2: SEM micrographs of InAs nanowires on growth substrate. (a) Previous InAs nanowire growth on a [111] InAs substrate. Since the wires also grow in the $\langle 111 \rangle$ direction, the wires grow perpendicular to the surface. Scale bar $1 \mu\text{m}$. (b) InAs wires from the same growth as the wires examined in this thesis. The wires lie flat on the growth substrate ([111] InAs) after having been cleaved from the substrate (by mechanical force). The wires can be seen to be $\sim 3\text{-}6 \mu\text{m}$ long. Scale bar $1 \mu\text{m}$. (c) Tilted side view of a previous growth of InAs wires, where the side facets and the catalytic gold particle can be seen. Scale bar 100 nm . (d) Top view of same growth as in (c); the hexagonal cross section and the perpendicular orientation to the substrate is clearly seen. Scale bar 100 nm . (SEM micrographs courtesy of Martin Aagesen).

will be made to the well-established properties of the bulk *zb* InAs.

InAs has a low, direct band gap, $E_g^{zb} = 0.417 \text{ eV}$, a low effective electron mass, $m^* = 0.026 m_e$ and a strong spin-orbit coupling, $\Delta_{SO} = 0.39 \text{ eV}$. [78]

InAs is also known to make Schottky barrier free contact to gold and Ti due to pinning of the Fermi level of the metal in the conduction band of InAs creating a surface accumulation layer of electrons [81–83]. The InAs nanowires show n-type conduction, likely due to non-intentional doping and pinning of the Fermi level in the conduction band at the surface of the wire.

Due to the low effective electron mass and high spin-orbit coupling, bulk InAs has a large g -factor, $|g_{bulk}| = 14.7$ [75], leading to a large Zeeman splitting in a magnetic field. The g -factor is suppressed in confined structures [75] due to orbital momentum quenching [84–86].

2.2 GaAs/AlGaAs heterostructures

The two-dimensional electron gas (2-DEG) in a GaAs/AlGaAs heterostructure has truly been the platform for much of the mesoscopic low-temperature physics that has been conducted for the last couple of decades. What makes the GaAs 2DEG so attractive is the flexibility in the structures that can be created using standard lithographic processes (e-beam and optical) and the high electron densities and mobilities that can be achieved allowing measurement of quantum mechanical effects [2].

The GaAs heterostructure is grown by MBE, and starts from a GaAs substrate as illustrated in Fig. 2.3. On top of this substrate a superlattice of alternating layers is grown to reduce lattice mismatch and release stresses. The high density layer of high mobility electrons is formed at the interface between $\sim 800 \text{ nm}$ of “freshly grown” GaAs and a layer of $\text{Al}_{0.3}\text{Ga}_{0.7}\text{As}$, due to a difference in bandgap between the two semiconductors. Due to sharply defined region of Si donor atoms (Si δ -doping) incorporated in the $\text{Al}_{0.3}\text{Ga}_{0.7}\text{As}$ a transfer of electrons happens from the $\text{Al}_{0.3}\text{Ga}_{0.7}\text{As}$ side to the GaAs side of the interface. This transfer of charge causes a band bending, creating a potential well along interface on the GaAs side to which the electron from the Si donors are confined; this is the 2-DEG. The density of electrons depends on the donor concentration and ionization, and the high mobility of the electrons in the 2-DEG is possible due to the spatial separation between the ionized donors and the 2-DEG. This causes the 2-DEG electrons to only suffer small angle scattering from the disorder potential of the donors [87, 88]. Due to the shallowness of the potential well, only the lowest band is occupied at low temperatures.

Defining metal gates on the surface of the heterostructure enables one to deplete the 2-DEG beneath the gate in response to negative voltages applied to the gates. This will confine the electrons in the 2-DEG further and can, depending on the geometry of the depletion gates, be used to define one- dimensional structures, e.g. quantum point contacts(QPCs), and “zero” dimensional structures, i.e. structures that are confined to mesoscopic size in all dimensions, such as quantum dots [3].

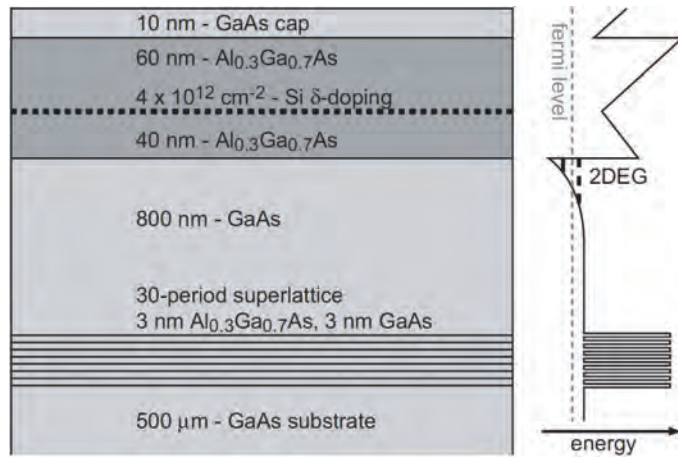


Figure 2.3: Schematic of layers in a GaAs heterostructure and corresponding conduction band diagram showing the quantum well at the GaAs/AlGaAs interface creating the 2DEG. Adapted from [89].

The 2-DEG is electrically contacted by a specific mixture of gold and germanium forming an eutectic alloy. Upon annealing, this alloy penetrates into the wafer making contact to the 2-DEG and ensuring an ohmic current-voltage response free of the Schottky barrier otherwise associated with metal-semiconductor interfaces [89]. The so-formed ohmic-contacts to the 2-DEG can now be used to make contact to the measurement setup.

2.3 Quantum dots: Electrons in a box

A quantum dot is a system which extension in all three dimensions is limited to a size such that the energy spectrum of the system is comprised of quantized levels, much like the situation in atoms, leading to the alternative name “artificial atoms” for quantum dots [90].

The relevant size scale for the quantization of energy levels is the Fermi wavelength; level quantization effects set in when the size of the system is comparable to the Fermi wavelength, which again is related to the electron density. Hence, for metals (electron densities $\sim 10^{27} m^{-3}$) level quantization only becomes significant for dots with a size of a few nanometers, whereas for semiconductors (2DEG electron densities of the order $\sim 10^{15} m^{-2}$) level quantization sets in for dots on the order of ~ 100 nm. Further, in semiconductors such as GaAs and InAs the small effective electron masses — 0.067 and $0.023m_e$, respectively — increase quantization effects compared to metals where effective electron masses are usually $\gtrsim m_e$.

In addition to the level quantization, the small size of the quantum dots also leads to a strong electrostatic interaction between the electrons on the dot, meaning that the addition of an electron to the dot raises the energy of the system by the Coulomb charging energy, $E_C = e^2/C$, where C is the capacitance of the quantum dot.

For semiconductor quantum dots of a size around 100 nm the level quantization, $\Delta E \sim$

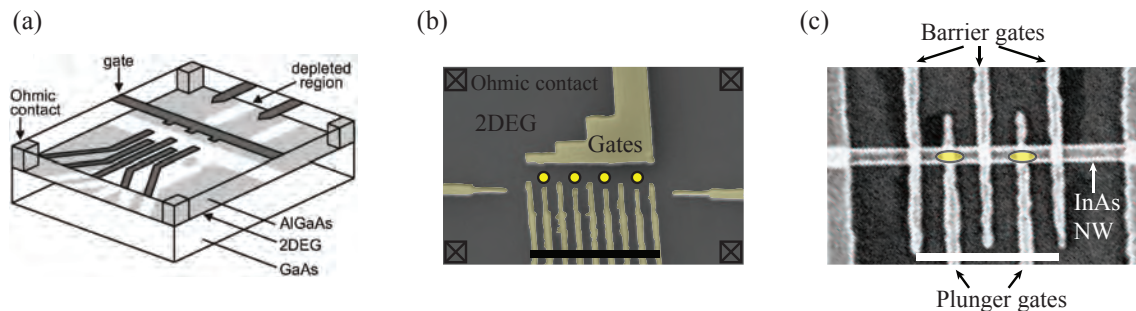


Figure 2.4: Electrostatically defined quantum dots in (a)-(b) a GaAs/AlGaAs heterostructure 2DEG and (c) an InAs nanowire. (a) is adapted from [93]

0.1 meV, and the charging energy, $E_C \sim 1$ meV, are of comparable size. Of course the exact numbers will depend on occupation, geometry/capacitance, dimensionality and materials.

For semiconductor materials such as silicon (Si), germanium (Ge), gallium arsenide (GaAs) and indium arsenide (InAs) quantum dots are formed either by growing nanocrystals [9] or by confining the electrons in a two-dimensional [3] or one dimensional system [91, 92] further by applying negative voltages to metallic gates or by growing or etching confining barriers.

The quantum dot systems investigated in this thesis are electrostatically defined in GaAs/AlGaAs heterostructure 2DEGs and InAs nanowires using metallic gates, as illustrated in Fig. 2.4(a)-(c). The dots are coupled to source and drain leads via tunnel barriers, allowing electrons to tunnel on and off the quantum dot, and individual gates give control over both tunnel barriers (barrier gates in (c)) and dot potentials (plunger gates in (c)).

A simple circuit model for a quantum dot resistively and capacitively coupled to source and drain electrodes and capacitively coupled, only, to a gate electrode is shown in Fig. 2.5. The tunnel junctions are characterized by a capacitive and a resistive link in parallel, parameterized by a tunneling resistance, R_S and R_D , and capacitance, C_S and C_D for source and drain electrodes, respectively. The coupling of the gate to the quantum dot is parameterized by the gate capacitance, C_g . As simple description of the energetics of the quantum dot in terms of these capacitances are given in the constant interaction model, see e.g. refs. [3] and [93].

For opaque tunnel barriers ($R_{S,D} \geq h/e = 25.8$ k Ω [3]) the quantization of the electron charge in terms of the elementary charge, $e = 1.602 \times 10^{-19}$ C, becomes important. The charges become localized either on the dot or in the leads as the tunneling time between leads and dot become exceedingly long; now the number of electrons on the dot is not fluctuating. Instead, the dot settles to the number of electrons, N , that minimizes the overall energy of the system of quantum dot and leads. In terms of electrochemical potentials this corresponds to the requirement $\mu(N) < \mu_{S,D} < \mu(N+1)$, where $\mu(N)$ is the electrochemical potential for the dot occupied by N electrons and $\mu_{S,D}$ are the electrochemical potentials of the source and drain electrodes, respectively, see Fig. 2.6(a). The energy needed to place an additional electron on the quantum dot will generally both include the charging energy,

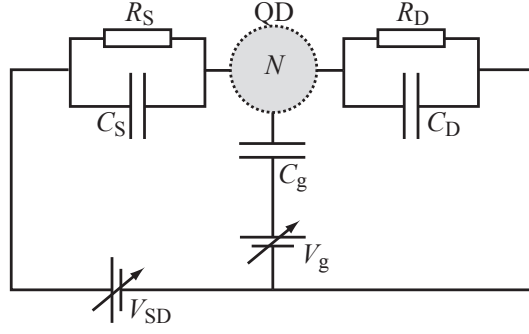


Figure 2.5: Circuit model of a quantum dot, QD, tunnel coupled to a source, S, and drain, D, electrode, and capacitively coupled to a gate electrode. A bias, V_{SD} can be applied across the source and drain, as well as to the gate electrode, V_g .

E_C , and the level quantization energy, ΔE , i.e. $E_{\text{add}} = \mu(N+1) - \mu(N) = E_C + \Delta E$.

To observe the effect of both charging and level quantization, on the equilibrium occupation of the quantum dot, the temperature must be low enough for the energy scales of the dot to dominate the thermal energy, $k_B T$, so that $\Delta E, E_C \gg k_B T$, see Fig. 2.6(a). For an dot energy scale of around 0.1 meV this translates to a temperature well below 1 K, as $k_B T = 0.086$ meV for $T = 1$ K. Therefore, electron transport measurements on semiconductor quantum dots take place in refrigerators that cool the sample to temperatures around $\sim 10 - 100$ mK.

Signs of level quantization and Coulomb repulsion in transport through a quantum dot can both be seen as a function of gate voltage, V_g , and source-drain bias, V_{SD} . For small source-drain bias, transport through the dot can only occur by transitions between successive ground state electron occupations, the criteria being that $|V_{SD}| < \Delta E$, so that only the lowest energy levels are available to the electrons occupying the dot. Electron transport from source to drain through the dot is only possible when an electrochemical potential on the dot, $\mu(N)$, is positioned between the source and drain electrochemical potentials, $\mu_S \geq \mu(N) \geq \mu(D)$, see Fig. 2.6(c). For the situation $\mu(N) < \mu_{S,D} < \mu(N+1)$, transport through the dot is blocked and the electron number on the dot is fixed, even in the presence of a source-drain bias, an effect known as Coulomb blockade, see Fig. 2.6(b) and (d). The electrochemical potentials for the different ground state transitions in the quantum dot can be tuned with the gate voltage, V_g . Sweeping the gate voltage will give a series of peaks in the current through the dot, I_{dot} . Each peak corresponds to a ground state transitions, changing the number of electrons on the dot, while the number of electrons is constant between the peaks, Fig. 2.6(d). The distance between the peaks is related to the addition energy as $E_{\text{add}} = e\alpha \Delta V_g$, where $\alpha = C_g / \Sigma C$ is the lever arm that gives the ratio between gate voltage change and energy shift.

The coulomb blockade can also be lifted by increasing the source-drain bias, V_{SD} , and for $eV_{SD} > \Delta E$ transport is no longer restricted to ground state transitions, but can involve excited states, where the electrons of the dot are not in a minimum energy configuration,

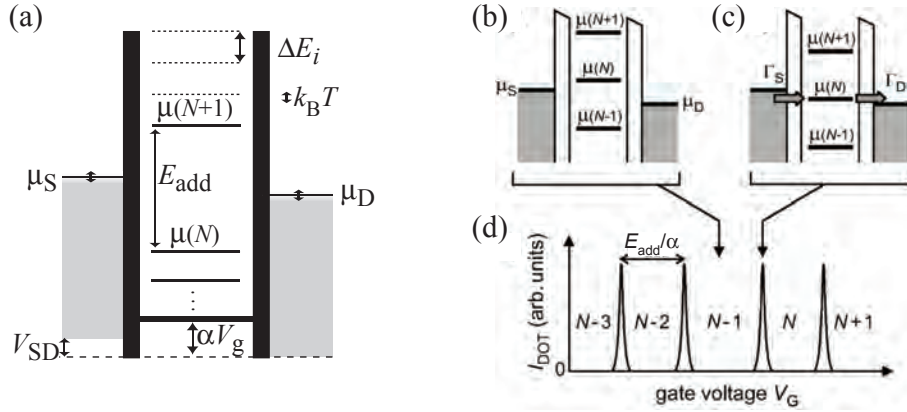


Figure 2.6: Schematics of quantum dot levels and low-bias transport. (a) Level diagram showing the electrochemical potentials of the quantum dot for adding the N 'th electron and N 'th+1 electron, including addition to excited states (dashed lines) separated by the quantization energies ΔE_i . The electrochemical potentials are tunable via the gate voltage, V_g . (b) Coulomb blockade at low bias ($< eV_{\text{SD}}$), where only ground state transitions on the dot are allowed, but none are available at the given gate voltage tuning. (c) Low-bias tunneling of electrons from source to drain through the dot by occupying the N electron ground state on the dot, corresponding to the N -electron electrochemical potential being positioned between source and drain electrochemical potentials. (d) Schematic representation of a measurement of the current through the dot as a function of V_g , the current cycling between Coulomb blockade and peaks of current, as dot electrochemical potentials are shifted with the action of the gate. (b)-(d) are adapted from [93].

gray line in Fig. 2.7(a). Fig. 2.7 (b) shows the energies, $U(N)$ and $U(N + 1)$, for N and $N + 1$ electrons in both ground (GS) and excited state (ES) configurations, and indicates possible transitions with arrows, the colors corresponding to the coloring of the electrochemical potentials for the same transitions in (c). A measurement of current or differential conductance as a function of both V_g and V_{SD} is called a bias spectroscopy or stability diagram, and Fig. 2.7(d) shows such idealized schematic representation of such a measurement, for the transitions considered in (b) and (c), with corresponding level diagrams shown for several characteristic point of the stability diagram. Lines in the diagram correspond to a change in the current through the dot. The most characteristic feature of such a stability diagram are the diamond shaped regions of Coulomb blockade (below the black lines and symmetric around $V_{\text{SD}} = 0$) where the number of electrons on the dot is constant (N and $N + 1$ in (d)). Where the lines corresponding to transport through an excited state cross the ground state transition lines (black in (d)), the corresponding level quantization energies, $\Delta E(N)$ and $\Delta E(N + 1)$, can be read off as the bias voltage translates directly into an energy.

2.3.1 Double quantum dots

As the gate configurations in Fig. 2.4 indicate, the intended experiments for this thesis are concerned with double quantum dots. Carrying over the description of one quantum dot

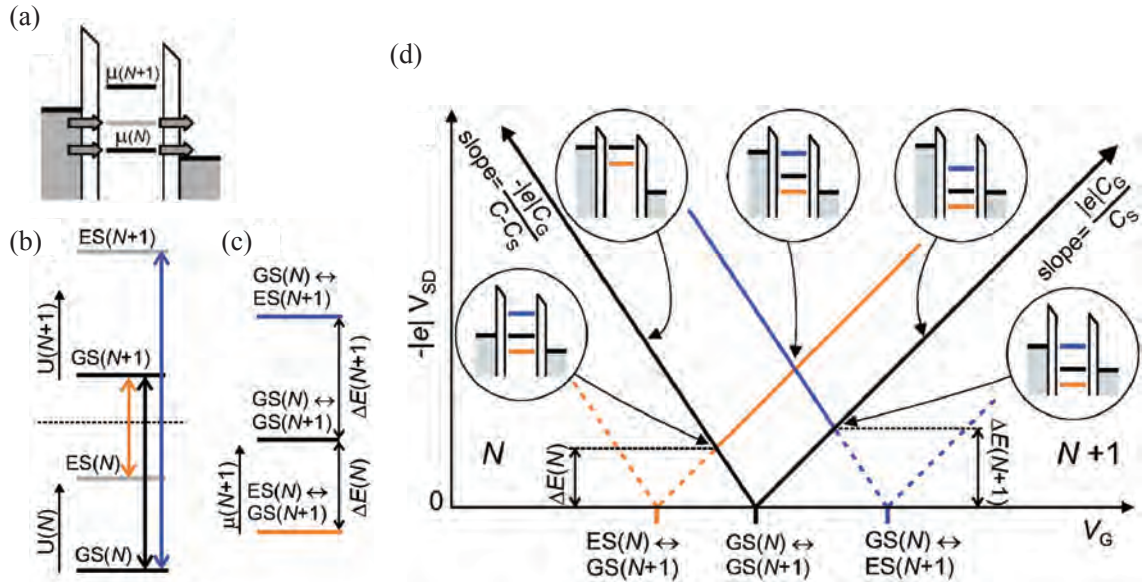


Figure 2.7: Schematics of high-bias transport. (a) With increased bias electron transport can occur via excited states (grey line) in addition to via ground states (black lines). (b) Ground state (GS) and excited state (ES) energies for N electrons ($U(N)$) and $N + 1$ electrons ($U(N + 1)$). (c) Electrochemical potentials for the transitions between N and $N + 1$ electron charge states ($\mu(N + 1)$) indicated by arrows in (b). (d) Schematic representation of a measurement of differential conductance through the dot, dI/dV_{SD} , as a function of V_{SD} and V_G ; the lines indicate where the transitions in (c) occur as a function of V_{SD} and V_G leading to a change in the differential conductance. Level diagrams indicates the alignment of chemical potentials at different positions along the transition lines. Again ground state transitions are in black and excited state transitions in colors corresponding to (c). Coulomb blockade of transport is active at $|V_{SD}|$ below the black lines that, when extrapolated to negative bias, define diamond shaped regions of well defined electron occupancy $N, N + 1 \dots$. Adapted from [93].

as an “artificial atom”, the double quantum dot system could be as an “artificial molecule”. The “inter-atomic” bond character is tunable via the gate controlling the inter-dot tunnel coupling; from ionic-like with electrons localized on each dot for weak (or no) tunnel coupling to covalent-like with electrons delocalized over both dots for strong tunnel coupling [3, 94].

Again, a simple circuit model for a double quantum dot as in Fig. 2.8 (a) is easily written up in analogy to the single quantum dot, see Fig. 2.8 (b). This allows for determining the energetics of adding electrons to each of the dots in the double quantum dot in terms of capacitances C_L , C_R and C_m , where $C_{1(2)}$ is total capacitance of dot number 1 (2), including the capacitance to dot 2 (1), the mutual capacitance C_m [94].

As for the single dot adding and removing electrons to the either of the dots is possible with the action of the gates, and Fig. 2.8(c) shows the charge stability diagram depicting the equilibrium electron occupation (N_L, N_R) as a function of gate voltages V_{gL} and V_{gR} . The grey plot shows the situation for completely uncoupled dots; cross and mutual capacitances ($C_{gL(R)x}$ and C_m , respectively, in Fig. 2.8(b)) are zero and addition of electrons to the two dots are independent of each other yielding transition lines parallel to the gate axes. For finite cross and mutual capacitance the charge transition lines have slopes due to the cross capacitance and the line crossings are separated into two points due to the mutual capacitance, that makes the addition of electrons in one dot depend on the filling of the other dot; the areas of constant electron occupation are now honeycomb shaped. The charge transition line crossings are called the triple points, as here, three charge states become degenerate.

At low bias for weakly coupled dots transport of electrons from source to drain is only possible at the triple point, where transport occurs by cycling through the three degenerate charge states, as indicated in the level schematics in Fig. 2.8(c). Here, the lower of the points (solid circle) corresponds to an electron tunneling sequentially across the double dot; the upper point (open circles) corresponds to a hole tunneling sequentially in the opposite direction. With stronger dot-lead couplings transport is also possible along lines connecting triple points by cotunneling processes, see level diagrams in Fig. 2.8(c). The effect of the inter-dot tunnel coupling strength on the transport through the double quantum dot is shown Fig. 2.8(d). This shows measurements of the logarithm of double dot conductance (dark is high conductance) as a function of plunger gate voltages, with increasing the inter-dot tunnel coupling (inversely related to R_m) through the plots 1-6. Transport along the lines connecting triple point increases with inter-dot coupling and the lines go from showing sharp kinks to showing soft wiggles accompanied by an increasing separation between triple points. This corresponds to an increasing hybridization of the charge states on the two quantum dots. With higher inter-dot coupling, the electrons become increasingly delocalized over the two dots until the two dots effectively act as one large dot, the electrons no longer being localized on one or the other, but spreading equally over both (see plot 6 in Fig. 2.8(d)) [3]. Level hybridization is not covered by the simple

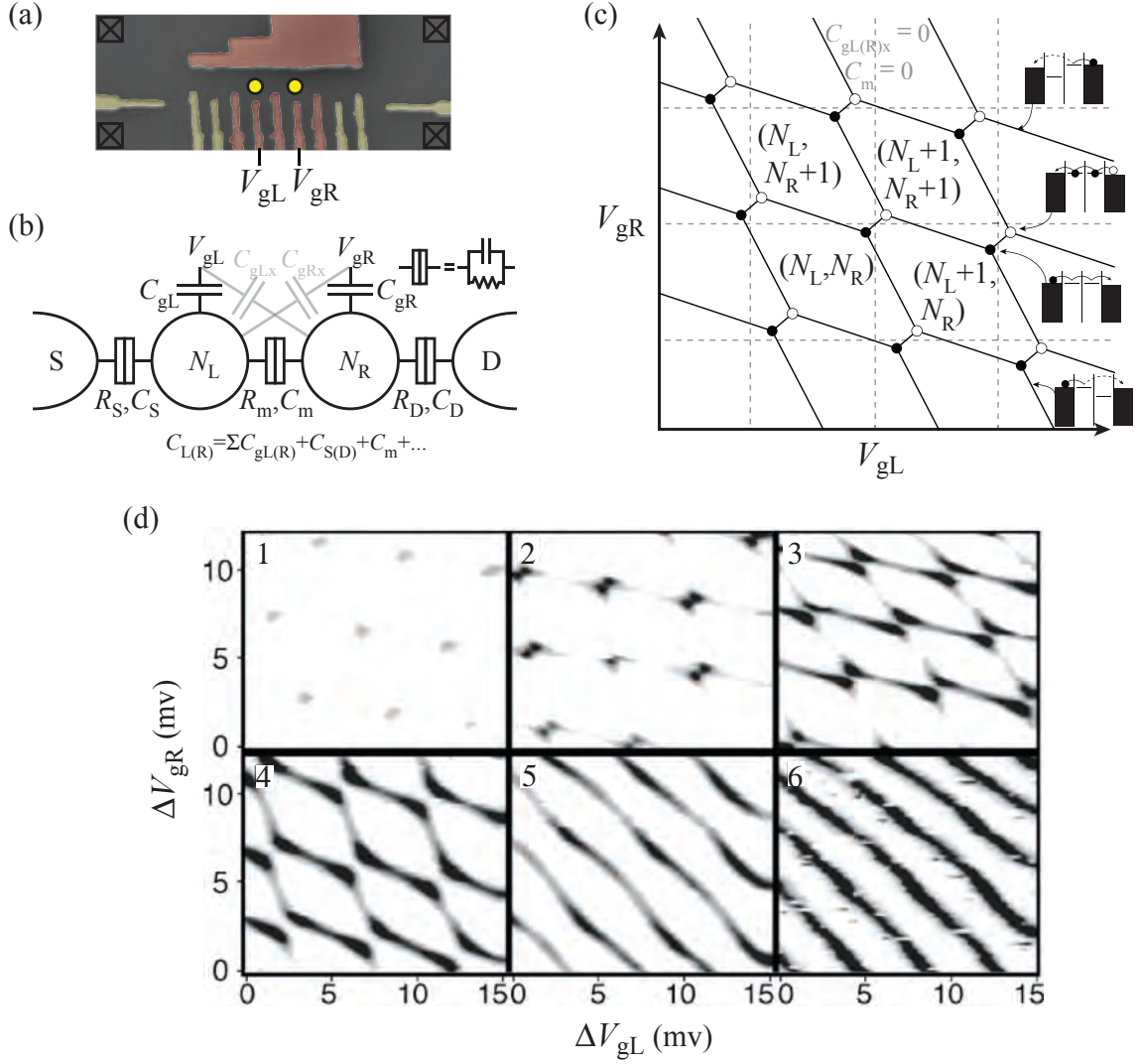


Figure 2.8: Double quantum dot circuit model and charge stability diagram. (a) Gate defined double dot in GaAs heterostructure, the dots indicated by yellow circles at positions and with coupling determined by the voltages on the active gates (red). Plunger gates, $V_{gL, gR}$, control the electrochemical potential on the dots. Electron transport through the dot is possible by applying a bias to the source and drain via the ohmic contacts (crossed boxes) (b) Circuit model for a double quantum such as that shown in (a), assuming that the tunneling barrier between the dots is sufficiently opaque that electrons are localized on either dot. In addition to the coupling of each plunger gate to its corresponding dot, there will in general also be a weaker cross capacitive coupling from left (right) plunger gate to the right (left) dot. (c). Charge stability diagram mapping the equilibrium charge occupation (N_L, N_R) as a function of plunger gate voltages $V_{gL, gR}$, the different charge states mapping out a honeycomb pattern. For weakly coupled dots electron transport through the double dot is only possible at the triple points where three charge states become degenerate, see level diagrams. With stronger coupling transport is also possible along lines connecting triple points by cotunneling processes, see level diagrams. (d) Logarithm of double dot conductance measured as a function of plunger gate voltages, and increasing the inter-dot tunnel coupling (inversely related to R_m) through the plots 1-6. Dark is high conductance. At the highest inter-dot coupling, the two dots effectively act as one large dot, the electrons no longer being localized on one or the other, but spreading over both. (d) Adapted from [3].

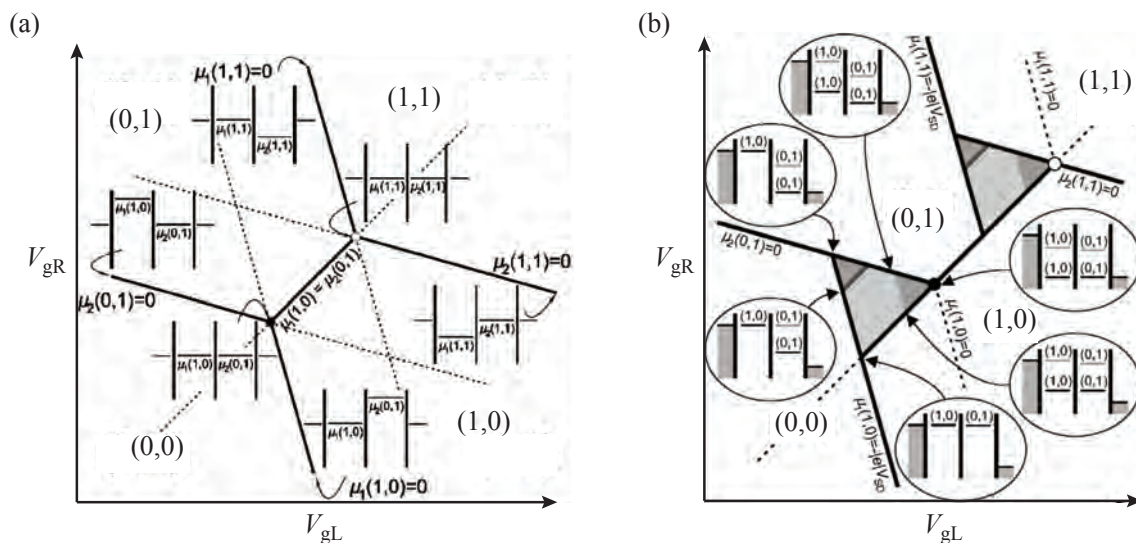


Figure 2.9: Electrochemical potentials around the triple points (a) without and (b) with bias across the double dot. $\mu_{1(2)}$ correspond to $\mu_{L(R)}$. (a) Adapted from [94], (b) from [93].

electrostatic model indicated in Fig. 2.8(b), but will be treated further in Section 2.3.2 below.

At finite bias the triple points expand into triangles within which the three charge states of the triple points are accessible within the bias window, see Fig. 2.9 (a) and (b) for comparison between the charge stability diagram around the triple points with and without a bias applied, respectively. Elastic transport through the dot for a finite bias is possible along the base of the triangle where the ground states aligned and, for $V_{SD} > \Delta E$, also when excited states are aligned, yielding lines of high current parallel to the base of the triangle at a distance corresponding to the level spacing, ΔE . Inelastic transport, when levels on the two dots are not aligned, will give rise to a current within the area of the triangle (light grey in Fig. 2.9(b)), the inelastic current increasing when additional levels enter the bias window (dark grey). The strength of the different elastic and inelastic processes (and hence their visibility in experiments) will depend strongly on the relative magnitudes of the tunnel barriers, the coupling to the environment allowing for inelastic tunneling and the relaxation within the dots [93]. Level diagrams in Fig. 2.9 (b) show the positions of electrochemical potentials at given detunings.

In many of the GaAs double dot experiments discussed later in this thesis, see Section 5, page 69, inter-dot transitions from $(N_L, N_R + 1)$ to $(N_L + 1, N_R)$ are investigated by detuning the electrochemical potentials of the two dots in a way that keeps their average constant. This corresponds to changing the plunger gate voltages along an axis that is perpendicular to the base of the bias triangle/the line between the triple points. This axis is referred to as the detuning axis, the detuning being represented by ε . For the inter-dot transitions, electrons are not exchanged with the leads and the spin of the electrons are conserved, making the inter-dot tunneling subject to the interplay between spin selection

rules, charging energy and level quantization leading to interesting phenomena such as Pauli spin blockade [95]. In the following sections I examine the spin states in the two-electron double quantum dot in order to explain the Pauli spin blockade, which is used as an important tool for spin state read-out in the GaAs double quantum dot experiments in this thesis, see Section 5, page 69.

2.3.2 Spin states in two-electron double dots and Pauli spin blockade

In the following description of inter-dot tunneling in double quantum dots we will take into account only the topmost level in each dot, neglecting the interactions of electrons in these levels with other electrons in lower lying levels. Effectively this is the same as analyzing the inter-dot transitions of the double quantum dot in the one- and two-electron occupation range, as each level can hold at most two electrons due to the Pauli exclusion principle.

For the double dot occupied by a single electron the inter-dot transitions are between the charge states $(0, 1)$ and $(1, 0)$, and both are spin doublets that are split in a magnetic field, but in zero magnetic field the inter-dot tunneling is spin independent.

For the two-electron double dot transitions are between the $(1, 1)$ and $(0, 2)$ charge states. For two electrons there are four possible spin configuration: one singlet, denoted S ; and three triplet states, denoted T_- , T_0 and T_+ corresponding to spin quantum numbers $m_S = -1, 0, 1$, respectively. The spin part of their wave functions are

$$\begin{aligned} S &= \frac{1}{\sqrt{2}}(|\uparrow\downarrow\rangle - |\downarrow\uparrow\rangle), \\ T_+ &= |\uparrow\uparrow\rangle, \\ T_0 &= \frac{1}{\sqrt{2}}(|\uparrow\downarrow\rangle + |\downarrow\uparrow\rangle), \\ T_- &= |\downarrow\downarrow\rangle, \end{aligned}$$

where the arrows denote the spin orientation of the electron. The triplet states are degenerate at zero magnetic field, Fig. 2.10(a), but are split up in a magnetic field, B , by the Zeeman energy $E_Z = g\mu_B B m_S$, where g is the electron g -factor and $\mu_B = 5.788 \times 10^{-5} \text{ eV/T}$ is the Bohr magneton, Fig. 2.10(c). In GaAs where $g = -0.43$ this means that T_+ will lower its energy with magnetic field while T_- will increase in energy.

For detuning $\varepsilon < 0$ $(1, 1)$ is the ground-state charge configuration and all four spin configuration are energetically accessible - in absence of magnetic field and for zero (negligible) coupling all states are degenerate, Fig. 2.10(a). For detuning $\varepsilon > 0$ $(0, 2)$ is the ground-state charge configuration, and due to tight confinement the spin-singlet, denoted $(0, 2)S$, forms the ground-state with the spin-triplet states split off by the energy ΔE_{ST} ($\sim 0.4 \text{ meV}$) dominated by the orbital level spacing [93]. Level diagrams above Fig. 2.10(a) show the alignment of electrochemical potentials at different detunings.

Due to a finite interdot tunnel coupling, t_c , between the two quantum dots in the DQD, the $(1, 1)$ and $(0, 2)$ charge states will hybridize near their energy degeneracy point,

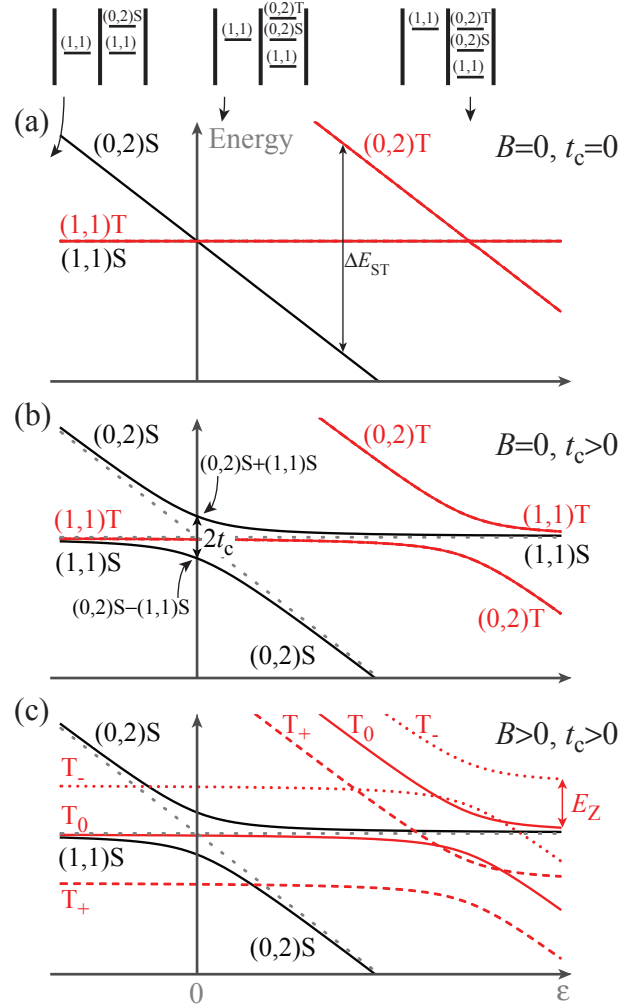


Figure 2.10: Energy spectrum for two coupled, spinful states as function of detuning, ε . The four different spin states, one singlet S and three triplets $T_{+,-,0}$, are plotted for both charge occupations $(1,1)$ and $(0,2)$ for different magnetic field, B , and interdot tunnel coupling, t_c . (a) $B = t_c = 0$. The $(1,1)$ states are degenerate and cross $(0,2)S$ at $\varepsilon = 0$ with the degenerate $(0,2)$ triplet states degenerate and separated by the singlet-triplet energy, ΔE_{ST} . (b) $B = 0, t_c > 0$. The tunnel coupling makes the $(1,1)$ and $(0,2)$ states anti cross with their spin counterparts, creating detuning dependent splittings. (c) $B > 0, t_c > 0$. A magnetic field splits off the T_{\pm} states removing the last degeneracies in the system.

making a bonding and an antibonding orbital that are linear combinations of the two unhybridized charge states and shifted respectively down and up in energy compared to their “zero-coupling” energies, Fig. 2.10(b) [94]. Due to spin conservation the $(1,1)S$ will only couple to the $(0,2)S$ at what we define as zero detuning, $\varepsilon = 0$, leaving the $(1,1)$ and $(0,2)$ triplet states to hybridize at larger detuning, Fig. 2.10(b) and (c). This means that there at the singlet degeneracy point, $\varepsilon = 0$, will be a difference in electron distribution between the singlet and triplet states, as the singlet charge distribution will be in an equal superposition of $(1,1)$ and $(0,2)$, whereas the triplet state will be fully in the $(1,1)$ state with equal electron density on each dot. This can for instance be exploited for read out of the spin state by charge detection [96] and can be used for electrostatic coupling of double quantum dot spin qubits [97, 98].

Another effect of the tunnel coupling is a detuning dependent splitting, $J(\varepsilon)$, between the $(1,1)S$ and $(1,1)T$ states equal to the strength of the tunnel coupling t_c at the singlet degeneracy point, Fig. 2.10(b). In a magnetic field the T_{pm} states are split off, thus creating an effective two-state subspace of S and T_0 , the splitting of the states, $J(\varepsilon)$, normally referred to as the exchange splitting.

Pauli spin blockade in double QDs

Due to spin conservation during inter-dot tunneling and the large difference in singlet-triplet splitting between the $(1,1)$ and $(0,2)$ charge states, *cf.* Fig. 2.10, the $(1,1)$ - $(0,2)$ transition can be blocked as illustrated in Fig. 2.11(a)-(b) for a DC measurement. For forward bias ($V_{SD} > 0$) transport occurs unhindered via the charge cycle $(0,2)S \rightarrow (1,1)S \rightarrow (0,1)$, as only the $(0,2)S$ state is energetically available upon reloading from $(0,1)$, Fig. 2.11(a). For reverse bias ($V_{SD} < 0$) transport can occur through the charge cycle $(1,1)S \rightarrow (0,2)S \rightarrow (0,1)$, Fig. 2.11(b); however, reloading from $(0,1)$ will create $(1,1)S$ and T with equal probability, and as soon as a $(1,1)T$ is loaded transport is blocked as the $(0,2)T$ is energetically inaccessible for $|V_{SD}| < E_{ST}$, Fig. 2.11(c).

So far we have ignored interaction of the spin with the environment, which can couple singlet and triplet spin states, lifting the Pauli spin blockade on time scales depending on the nature of the coupling mechanism. In the next section we will describe some of the most important mechanisms leading to spin decoherence and relaxation in (GaAs) quantum dots and the associated time scales.

2.4 Decoherence and relaxation

The terms decoherence and relaxation refer to the effects of processes by which the two-level system that is the qubit loses information. Here we focus on loss processes due to fluctuations in the environment, specifically the fluctuating nuclear spins of the host

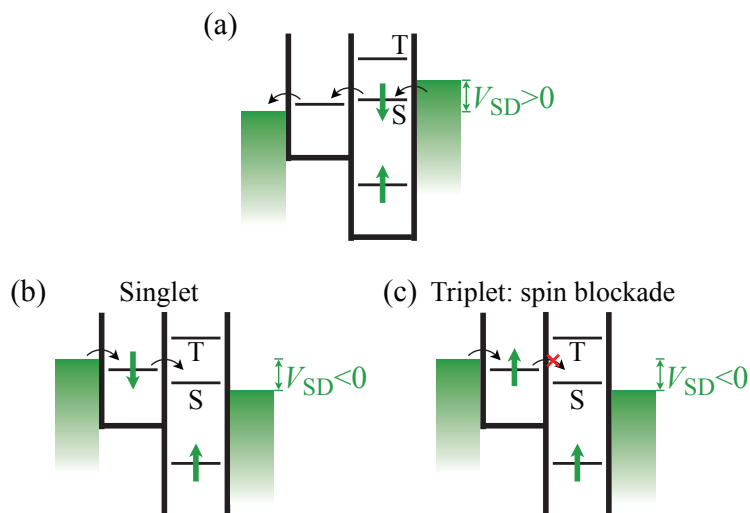


Figure 2.11: Pauli spin blockade in double quantum dot under DC bias. (a) Transport through charge cycle $(0,2)S \rightarrow (1,1)S \rightarrow (0,1)$ with positive bias. (b) Transport through charge cycle $(1,1)S \rightarrow (0,2)S \rightarrow (0,1)$ with negative bias, for loading into $(1,1)S$. (c) Pauli spin blockade of electron transport under negative bias due to loading of $(1,1)$ triplet while $(0,2)$ triplet is energetically inaccessible.

lattice². Mainly, the information contained in this section builds on the descriptions in references [77, 93, 99] which should be consulted for a more detailed discussion and further references.

Decoherence refers to the loss of phase coherence of an electron spin precessing around an external field. Decoherence conserves the energy of the system and is associated with the time scale T_2 .

Relaxation refers to energy relaxation of an electron spin from an excited state to the ground state by spin flip processes and is associated with the time scale T_1 . Since relaxation will also lead to decoherence, T_2 is limited by T_1 such that $T_2 \leq 2T_1$.

Relaxation and decoherence processes can be visualized using the Bloch sphere representation of a general spin state

$$|\psi\rangle = \cos(\theta/2)|\downarrow\rangle + \sin(\theta/2)e^{i\phi}|\uparrow\rangle, \quad (2.1)$$

where the angles θ and ϕ define a point on the surface of the Bloch sphere and the poles are the spin ground, $|\uparrow\rangle$, and excited state, $|\downarrow\rangle$, Fig. 2.12(a). Points within the Bloch sphere correspond to spin states that are not fully determined, e.g. points on the z -axis correspond to the states with unknown ϕ . Now, dephasing correspond to loss of information about ϕ so that the spin can be anywhere on the circle on the surface of the Bloch sphere defined

²Since the InAs nanowire experiments described in this thesis never proceeded to the level where spin manipulation experiments were performed, we will treat decoherence and relaxation from a GaAs perspective mainly, only briefly mentioning the large relative importance of some effects, such as spin-orbit coupling, for InAs [77].

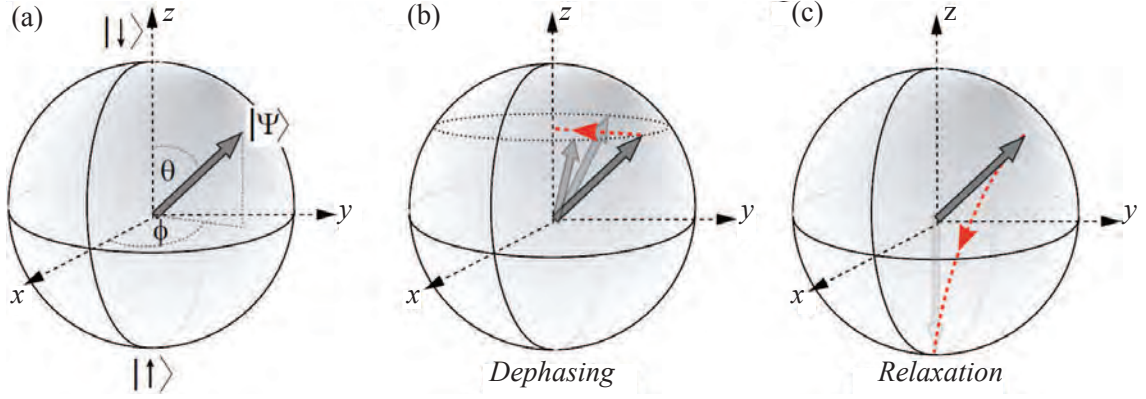


Figure 2.12: Bloch sphere representation of spin decoherence and relaxation. (a) Representation of a spin state on the Bloch sphere determined by the angles ϕ and θ . (b) Decoherence: Interactions with the environment leads to loss of the information stored in the angle ϕ . (c) Relaxation: Spin state relaxes to the ground state due to interactions with the environment involving dissipation of energy. Figure is adapted from [77].

by θ ; this is the projection of the original spin state on the z -axis, Fig. 2.12(b). Relaxation on the other hand corresponds to loss of knowledge of the angle θ , as the prepared state relaxes to the ground state associated with energy dissipation to the environment; however, as noted above, relaxation will also contribute to decoherence as ϕ is affected in the process as well, Fig 2.12(c) [77].

To describe how fluctuations in the environment in which the spin lives can affect decoherence and relaxation we look at a general hamiltonian for a fluctuating environment interacting with a split two-level spin system,

$$H_{\text{FE}} = E_Z \hat{\sigma}_z + \frac{\hbar}{2} [\delta\omega_z(t) \hat{\sigma}_z + \delta\omega_x(t) \hat{\sigma}_x + \delta\omega_y(t) \hat{\sigma}_y], \quad (2.2)$$

where E_Z is the splitting between the spin states and $\delta\omega_{x,y,z}(t)$ are fluctuations in the x, y, z -direction that couple to the spin components $\hat{\sigma}_{x,y,z}$ (Pauli matrices). The source of these fluctuations can be many such as moving charges in the substrate, electric fields from gate voltages and magnetic dipoles of the nuclear spins to name a few.

To describe the contribution of the fluctuations to spin decoherence and relaxation it is useful to describe the fluctuations in terms of noise spectral density

$$S_{x,y,z}(\omega) = \frac{1}{2\pi} \int_{-\infty}^{\infty} e^{i\omega\tau} C_{\delta\omega_{x,y,z}}(\tau) d\tau,$$

, where $C_{\delta\omega_{x,y,z}}(t-t') = \langle \delta\omega_{x,y,z}(t) \delta\omega_{x,y,z}(t') \rangle$ is the autocorrelation function for the fluctuation $\delta\omega_{x,y,z}(t)$.

Relaxation of the spin from excited state to ground state is mediated by the x, y components of the fluctuations $\delta\omega_i$, but due to energy conservation only the E_Z/\hbar frequency component of the spectral density of the fluctuations contribute, giving $1/T_1 \propto S_x(E_Z/\hbar) + S_y(E_Z/\hbar)$. For example, a spin in a static magnetic field (z) will be flipped by in-plane (x, y) magnetic field fluctuations at the Larmor frequency set by the static, splitting field.

Dephasing is mediated by longitudinal fluctuations $\delta\omega_z$, so that a spin in a superposition state precessing in the x - y plane of the Bloch sphere at the Larmor frequency set by the splitting field will experience fluctuations in the Larmor frequency, leading to a phase accumulation $\Delta\phi = \int_0^\tau \delta\omega_z(t') dt'$ during the time τ . Unlike relaxation, all frequency components of $S_z(\omega)$ will contribute to loss of phase coherence.

The timescale, T_2 , and functional form of decoherence due to fluctuations are dependent on the amplitude, distribution and frequency spectrum ($S_z(\omega)$) of the fluctuations. The amplitude of the fluctuations is related to the width of the distribution of the fluctuation, $\delta\omega_z$, e.g. nuclear field, and examples of distributions are Gaussian and Lorentzian.

Decoherence due to low frequency component of the fluctuation spectrum is referred to as inhomogeneous broadening (or dephasing) and is associated with the time T_2^* , stemming from NMR experiments where an ensemble of spins see constant, but different $\delta\omega_z$ leading to decoherence when averaging over the ensemble. For a single spin the same effect is achieved when averaging over many measurements, each of duration τ so that $S_z(\omega) \simeq 0$ for $\omega > 1/\tau$, but in total covering an interval that samples the full distribution of $\delta\omega_z$. Hence, T_2^* is related to the width of the distribution of the fluctuation (the amplitude of the fluctuation).

The effect of the low frequency fluctuations on phase coherence of an ensemble can be reversed by a Hahn echo, Fig. 2.13. If the environment is quasi static on the time scale of τ , so that $S_z(\omega) \approx 0$ for $\omega > 1/\tau$ the decohering effect of the environment, $\delta\omega_z(t)$, during period τ can be canceled. Imagine a spin sitting in the x - y -plane of the Bloch sphere (rest frame with regard to E_Z/\hbar), Fig. 2.13(a). The spin is allowed to evolve freely for a period $t \lesssim \tau/2$ causing dephasing over the ensemble due to the different $\delta\omega_z$, Fig. 2.13(b). A π -pulse is applied around y (or x), (c), and leaving the spin to evolve freely for another period of t will lead to a cancelation of the accumulated phase and an overall π rotation around z , (d). If higher frequency fluctuations are present these will still contribute to (echo) decoherence as the cancelation is only effective for $\omega < 1/\tau$; extending the timescale of the echo measurement will lead to decoherence on the time scale $T_{2,\text{echo}}$ due to the low frequency fluctuations becoming important. $T_{2,\text{echo}}$, can be much longer than T_2^* when low frequency fluctuations dominate $S_z(\omega)$.

More elaborate echo sequences with more π -pulses within the total measurement period τ (Carr-Purcell pulses) can increase the efficiency of the echo in terms of canceling the effect of higher frequency fluctuations and extend $T_{2,\text{echo}}$ [77, 100].

Following this general description of the effects of a fluctuating environment coupling to the qubit spin we now turn to the sources of fluctuations and coupling mechanisms and their relative importance.

2.4.1 Interactions with nuclear spins: Overhauser field and dynamics

The wave function of an electron in a quantum dot will overlap with many nuclei and can interact with each of them through the hyperfine interaction. The hamiltonian for the Fermi contact hyperfine interaction, dominating for s -orbital like conduction band electrons

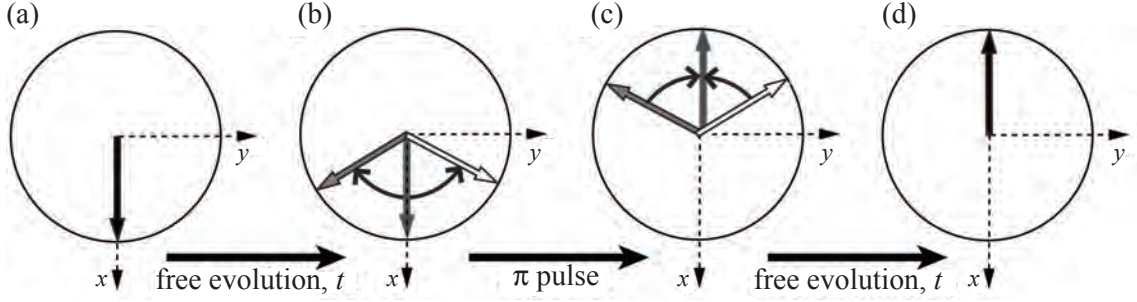


Figure 2.13: Hahn echo. Spin oriented along x -axis, (a), evolves freely for period t accumulating a phase, (b), which after applying a π pulse around y (or x), (c), is undone by evolving freely for another period t , (d). Figure is adapted from [77].

as in GaAs and InAs, is given by [93]

$$H_{\text{HF}} = \sum_{i=1}^N A_i \mathbf{I}_i \cdot \mathbf{S}, \quad (2.3)$$

where \mathbf{I}_i and \mathbf{S} are the spin operators for nucleus i and the electron spin, respectively and N is the number of nuclear spins interacting with the electron. $A_i = \nu A |\psi(r_i)|^2$ is the hyperfine coupling strength between the electron and nucleus i , with ν the volume of the unit cell containing one nucleus, A the average coupling strength and $|\psi(r_i)|^2$ the density of the electronic wave function at the position of the nucleus i . Since the electron wave function will have different overlap with the different nuclei A_i will vary for the different nuclei. The average coupling strength A ($\approx 90 \mu\text{eV}$ in GaAs) is the stoichiometric average of the coupling strengths of the different nuclear isotopes.

The interaction between electrons and nuclei goes both ways; the electron spin dynamics will, as described above, be affected by the nuclei, which we will return to later, but the nuclear spin dynamics will also be affected by the electron. However, the dynamics of the nuclei are much slower than the dynamics of the electron, so for describing the effects of the nuclei on the electron, we can to start with ignore nuclei dynamics and describe their effect as an apparent magnetic field, \mathbf{B}_N , the Overhauser field

$$H_{\text{HF}} = \left(\sum_{i=1}^N A_i \mathbf{I}_i \right) \cdot \mathbf{S} = g \mu_B \mathbf{B}_N \cdot \mathbf{S}. \quad (2.4)$$

If the nuclear spin are fully polarized $B_{N,\text{max}} \approx 5 \text{ T}$ in GaAs and $\approx 2 \text{ T}$ in InAs independent of N , but at the typical experiment temperature ($k_B T \approx 1 \mu\text{eV}$) and magnetic fields ($< 10 \text{ T}$) the nuclear spins are unpolarized and has average magnitude zero, but fluctuates in all three dimensions with a Gaussian distribution with a spread $\sigma_N = B_{N,\text{max}} \sqrt{N} = 5 \text{ mT}$ for a typical value of $N = 10^6$ for gate defined lateral quantum dots in GaAs.

The effect of the nuclear spins on the electron can thus be described as a randomly oriented magnetic field of magnitude $\approx 5 \text{ mT}$ adding to the externally applied magnetic field, B_0 . As described above this can contribute to both relaxation and decoherence of the spin.

In terms of decoherence the component of the nuclear magnetic field along the external field, B_N^z , will lead to dephasing by inducing a random phase (π -phase pick up in 83 ns for $B_N^z = 1$ mT) during free evolution. For the Gaussian distribution with spread $\sigma_N = 5$ mT the decoherence of the freely evolving spin state happens as e^{*t/T_2^*} with $T_2^* = \sqrt{2}\hbar/g\mu_B\sigma_N \approx 10$ ns. For an external field much larger than the nuclear, the transverse components of the nuclear field, $B_N^{y,z}$, will have negligible effect on the phase coherence, as they will change the precession axis by an angle $\sim B_N/B_0$ and change the Larmor frequency by $\approx g\mu_B B_N^2/2B_0$.

Driven oscillations in a spin-resonance experiment, see Section 5.3.3, page 76, will also be affected by to the random nuclear field; the longitudinal component B_N^z (parallel to external field, B_0) will shift the resonance frequency, $g\mu_B B_0/h$ for the oscillating, perpendicular field [101, 102], leading to damping of the driven oscillations for an ensemble average.

The main effect of the random nuclear field is dephasing of spin, but it will also contribute to spin relaxation through the transverse components $B_N^{x,y}$. However, the requirement is that the two relevant spin states are close in energy as the nuclear spin system can only absorb a small amount of energy. In terms of Overhauser field this is an equivalent argument as the above statement regarding the effect of $B_N^{x,y}$ on decoherence; only for $B_0 < B_N^{x,y}$ will the transverse components lead to relaxation by precession about $B_N^{x,y}$, as for $B_0 \gg B_N^{x,y}$ spins will precess about the z -axis.

However, as the instantaneous nuclear field is position dependent, relaxation will also be mediated indirectly by the hyperfine interaction, as electrical fluctuations, e.g. due to phonons, voltage noise on gates or charge fluctuations will induce an effectively oscillating Overhauser field from the perspective of the electron.

For the qubit based on the S - T_0 spin states of a double quantum dot the random nuclear field is important in terms of spin relaxation. The electron in each dot experiences a different, random field, and the difference between the fields will drive transitions between the two-electron singlet and triplet states; ΔB_N^z couples the triplet state T_0 to the singlet, S , and $\Delta B_N^{x,y}$ couple the triplet states T_+ and T_- to the singlet [96, 103, 104]. This will lead to lifting of spin blockade by relaxation from triplets to singlet depending on an interplay between interdot tunnel coupling, t_c , $(1,1)S$ - $(0,2)S$ detuning, ε , nuclear field difference and external magnetic field, Fig. 2.14. For a small tunnel coupling, t_c , and large nuclear field energy scale $E_N = g\mu_B B_N$ spin blockade is lifted in absence of external magnetic field, B_{ext} , independent of detuning ε . Applying a magnetic field will reinstate spin blockade as $T_{+,-}$ are separated from $S(1,1)$ by a Zeeman energy, E_Z larger than E_N . For a large t_c and E_N (but $t_c > E_N$) spin blockade is lifted at large detuning and $B_{\text{ext}} < B_N$, Fig. 2.14(a). With increasing detuning the exchange splitting becomes so low that $S(1,1)$ is again mixed with the triplets, whereas spin blockade is effective around $\varepsilon = 0$, due to a large exchange splitting $\approx t_c$. Applying magnetic field for $\varepsilon > 0$ will reinstate spin blockade as $T_{+,-}$ are separated from $S(1,1)$ by a Zeeman energy, E_Z larger than E_N ; however, T_0 is still coupled to S . For $\varepsilon \approx 0$, applying a magnetic field will lift spin blockade only as E_Z brings $T_{+,-}$

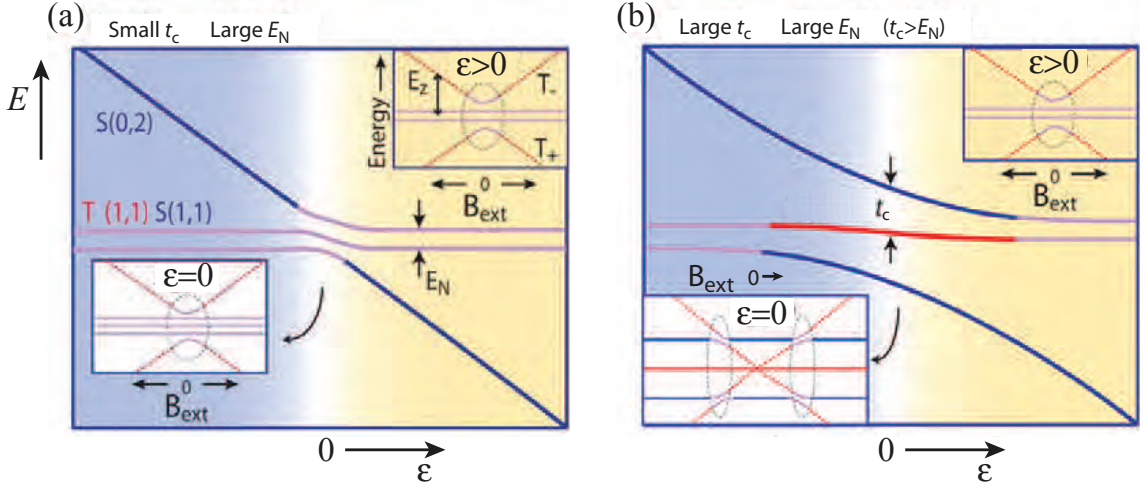


Figure 2.14: Effect of nuclear field, B_N , on spin blockade. (a) For a small tunnel coupling, t_c , and large nuclear field energy scale $E_N = g\mu_B B_N$ spin blockade is lifted in absence of external magnetic field, B_{ext} , independent of detuning ε . Applying magnetic field will reinstate spin blockade as $T_{+,-}$ are separated from $S(1,1)$ by a Zeeman energy, E_Z larger than E_N . (b) For a large t_c and E_N (but $t_c > E_N$) spin blockade is lifted at large detuning and $B_{\text{ext}} < B_N$ as exchange splitting becomes so low that $S(1,1)$ is again mixed with the triplets, whereas spin blockade is effective around $\varepsilon = 0$, due to a large exchange splitting $\approx t_c$. Applying magnetic field for $\varepsilon > 0$ will reinstate spin blockade as $T_{+,-}$ are separated from $S(1,1)$ by a Zeeman energy, E_Z larger than E_N . For $\varepsilon \approx 0$, applying a magnetic field will lift spin blockade only as E_Z brings $T_{+,-}$ within E_N of the exchange split singlet. Figure is adapted from [103].

within E_N of the exchange split singlet, Fig. 2.14(b).

Having used spin echo to annul the effect of the quasi static Overhauser field on the electron spin dynamics, one has to take into account the dynamics of the nuclear spins to account for the eventual decay of the spin (echo) coherence.

For the nuclear spin dynamics the two most important processes in GaAs are internuclear magnetic dipole-dipole interactions and the electron-nuclear hyperfine interaction. The magnetic dipole interaction between neighboring nuclear spins will have an effect on both the longitudinal, B_N^z , and the transverse, $B_N^{x,y}$, components of the nuclear magnetic field, the former through inelastic flip-flop processes while the latter through energy conserving precession. For flip-flopping nuclear spins i and j , this may be suppressed if $|A_i - A_j|$ is greater than the internuclear coupling strength. Hence, although the internuclear dipolar interaction might change $B_N^{x,y}$ on a $\sim 100 \mu\text{s}$ timescale, B_N^z might evolve more slowly ($\sim 10 - 100 \mu\text{s}$) depending on the size and thickness of the dot as, this affects the energy of flip-flops.

The hyperfine interaction between nuclei and electron will, just as it affects the electron spin, also affect the nuclear spin. The effect of the hyperfine interaction on the nuclear field is similar to that of the internuclear dipole; $B_N^{x,y}$ will evolve on a $\sim 10 \mu\text{s}$ timescale, and so will B_N^z (through electron-nuclear flip-flops) at zero magnetic field B_0 . However,

the process is suppressed in an external magnetic field due to the mismatch of the Zeeman energy scales for electrons and nuclei (about a factor of 10^3). Still, hyperfine mediated nuclear-nuclear flip-flops, where one electron-nuclear flip-flop is followed by another flip-flop between the electron and a different nucleus, can still occur (but are suppressed at even higher B_0) and will change B_N^z for $A_i \neq A_j$.

Using multiple sequences of π -pulses, so-called dynamical decoupling, the low-frequency cut-off of the dynamics of the nuclear bath by the Hahn echo can be extended to higher frequencies [105]. Power law scaling of T_2 with the number, n , of π -pulses ($T_2 \propto n^\gamma$) was found in measurements on a $S - T_0$ qubit by Medford *et al.* using concatenated, exchange mediated π -rotation [100]. This, also yielded a noise spectral density $S(f) \propto f^{-\beta}$ with $\beta = 2.6$ based on $\gamma = 0.7$. However, it could not be concluded whether these values were characteristic for Overhauser induced decay or rather a result of a specific combination of noise sources.

2.4.2 Spin-orbit coupling

For atoms, the orbital motion of the electron in the electric field of the nucleus will lead to an effective magnetic field in the rest frame of the electron, affecting the spin of the moving electron; this coupling between orbital motion and spin of the electron in an atom, is called spin-orbit coupling [106]. The effective magnetic field in the rest frame of the electron will be $B_{SO} \propto \mathbf{p} \times \mathbf{E}$, where \mathbf{p} is the momentum of the electron and $\mathbf{E} = -\nabla V(\mathbf{r})$ is the electric field, with $V(\mathbf{r})$ representing the electrostatic potential of the nucleus. Hence, the spin-orbit coupling is stronger for electrons in close proximity with the nucleus where \mathbf{E} and \mathbf{p} are greatest, and for heavier nuclei (atoms).

In semiconductors, the conduction electrons move in the electric field of the crystal lattice, and when including the periodic spin-orbit coupling potential from the lattice ions into the Hamiltonian of a perfect crystal, the Bloch eigenstates are no longer pure spin states [107]. The spin-orbit coupling couples the two spin states $|\uparrow\rangle$ and $|\downarrow\rangle$, so that the different eigenfunctions generally can be written [30, 107]

$$|\Psi \uparrow\rangle = [a_k |\uparrow\rangle + b_k |\downarrow\rangle] e^{i\mathbf{k}\cdot\mathbf{r}}, \quad (2.5)$$

and similarly for $|\Psi \downarrow\rangle$. The magnitude of the mixing depends on the magnitude of the matrix element between the different eigenstates $\langle \Psi \uparrow | H_{SO} | \Psi \downarrow \rangle$ and their separation in energy. Generally, the mixing is very subtle, so that $a \gg b = \Delta_{SO}/\Delta E \ll 1$, where Δ_{SO} is the spin-orbit coupling strength measuring the matrix element between two states and ΔE is their separation in energy. Therefore, it still makes sense to distinguish between ‘spin-up’ and ‘spin-down’ [30]. For crystals with an inversion center these new spin-up and spin-down states are degenerate [107].

The structure of the semiconductor crystal may give rise to additional spin-orbit coupling terms if it has either bulk inversion asymmetry (BIA) or structural inversion asymmetry (SIA). Bulk inversion asymmetry is present for *e.g.* zinc blende (GaAs and bulk

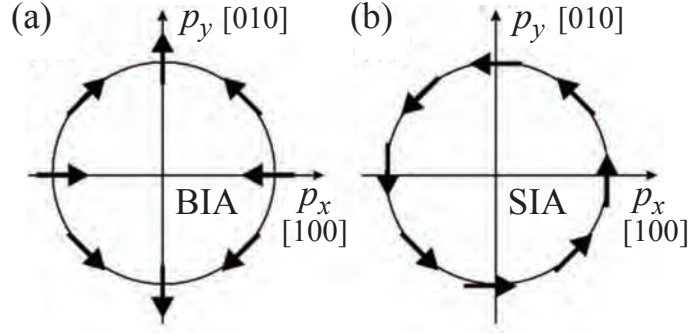


Figure 2.15: Small arrows indicate orientation of the apparent spin-orbit magnetic field B_{SO} due to the (a) Dresselhaus and (b) Rashba spin-orbit coupling for an electron traveling with crystal momentum p through an GaAs 2DEG. [xxx] denotes a crystal axis. Figure is adapted from [93].

and nanowire InAs) and wurtzite crystal structures (nanowire InAs), and structural inversion asymmetry is present in 2DEG heterostructures and likely also in InAs nanowires, due to both the structure itself and asymmetric gate coupling. The two contributions to the spin-orbit coupling are known as the Dresselhaus [108] and the Rashba [109] terms, respectively. Both lead to spin splitting of the otherwise spin degenerate mixed states in the conduction band [93, 108, 110], but differ in their order in momentum and their sign with respect to crystal axis, see Fig. 2.15. Hence, depending on the momentum of the electron, the two terms can both add to or subtract from each other, in agreement with the observed difference in the effect of spin-orbit coupling in similar devices with different orientation with respect to the crystal axis [102, 111].

The strength of the spin-orbit coupling will also depend on band structure parameters such as the band gap. Generally, the s-orbital (orbital quantum number $l = 0$) like conduction band electrons in semiconductors like GaAs and InAs should not show strong spin-orbit coupling, as the atomic basis for spin-orbit coupling can be rewritten as $\mathbf{l} \cdot \mathbf{s} = 0$ for $l = 0$. However, the top valence band holes are p-type ($l = 1$) leading to stronger spin-orbit coupling, Δ_{SO} , and for semiconductors with a small band gap, E_g , a correspondingly larger admixture of hole character in conduction electrons, will lead to increased spin-orbit coupling for the conduction band electrons. This translates to a moderate spin-orbit coupling strength for conduction electron in GaAs ($E_g = 1.52$ eV, $\Delta_{SO} = 0.34$ eV), and much stronger in small band gap materials like InAs (zinc blende) ($E_g = 0.42$ eV, $\Delta_{SO} = 0.41$ eV) and InSb ($E_g = 0.24$ eV, $\Delta_{SO} = 0.80$ eV).

The efficiency of the spin-orbit coupling in coupling momentum and spin will also depend on the size (and dimensionality) of the sample. In macroscopic systems, the semi-classical description of the effect of spin-orbit interaction as a momentum dependent magnetic field about which the spin precesses, leads to a measure of the strength of the spin-orbit interaction in terms of the distance over which the electron spin performs a π rotation, the so-called spin-orbit length ℓ_{SO} . For InAs $\ell_{SO} \sim 100$ -200 nm [112, 113] and for GaAs it is $\ell_{SO} \sim 35$ μm [111]. Now, as the size of the system is decreased below ℓ_{SO} the

effect of the spin-orbit coupling will be suppressed, and for quantum dots with a typical size in the range 10-100 nm the effect on the discrete orbital energy level spectrum can be described as a small perturbation for GaAs [93], whereas the effect is still significant for InAs dots [25, 114, 115]. For quantum dots, where $\langle p_{x,y} \rangle = 0$ as the electrons are stationary, the effect of the spin-orbit Hamiltonian on the spin split orbital levels, nl annuls since $\langle nl \downarrow | H_{\text{SO}} | nl \uparrow \rangle \propto \langle nl | p_{x,y} | nl \rangle \langle \downarrow | \sigma_{x,y} | \uparrow \rangle = 0$, but it is still effective for coupling opposite spin states with different orbital levels as well ($n'l' \neq nl$), $\langle n'l' \downarrow | H_{\text{SO}} | nl \uparrow \rangle \neq 0$. Assuming that the coupling is weak compared to the separation, the mixing may be described by perturbation theory. With $|nl\rangle$ denoting the unperturbed eigenstates in the n 'th band with momentum l , the new eigenstates $|nl\rangle^*$ can be approximated as [93, 107]

$$|nl \uparrow\rangle^* = |nl \uparrow\rangle + \sum_{n',l', \neq nl} \frac{\langle n'l' \downarrow | H_{\text{SO}} | nl \uparrow \rangle}{E_{nl} - E_{n'l'}} |n'l' \downarrow\rangle. \quad (2.6)$$

However, for the (1,1) occupation spin states of a double quantum dot, the spin-orbit coupling will couple directly, the singlet and triplet states (except for S and T_0 to first order in the interaction), as these involve different orbital states [93].

The mixing of spin and orbital components by the spin-orbit interaction is important in both single and double quantum dots, as it allows electric fields to couple to the electron spin through the effect on the orbital motion. This allows for spin manipulation by using electric fields [25, 111], but it also means that electrical noise will lead to spin relaxation. Besides electrical noise from the setup, lattice phonons can create electrical fields that can couple to the spin in the dots via the spin-orbit interaction. As the spin relaxation is associated with the emission of a phonon with the energy of the spin splitting, E_Z , the efficiency of the phonons in causing spin relaxation will be strongly dependent on magnetic field both through the phonon density of states at E_Z and the strength of phonon mediated coupling between the spin-orbit renormalized states. The latter depends on parameters such as i) the magnitude of the coupling between spin and different orbital states (cf. 2.6); ii) the electric field strength of the phonons and; iii) the strength of the phonon mediated coupling between orbital states of the quantum dot (wavelength of phonons vs size of dot).

Additionally, and importantly, the effect of a fluctuating electric field in causing spin relaxation via spin-orbit coupling is dependent on the application of an external magnetic field. Without an external field time reversibility gives that the rotation of a spin in the effective spin-orbit magnetic field during one half cycle of the oscillating electric field will be reversed during the next half cycle. With an magnetic field applied the rotations about the combined field $B_0 + B_{\text{SO}}$ in the two half cycles do not commute and a net spin rotation occurs, driving spin relaxation.

Interestingly, for a quantum dot in a 2DEG such as a GaAs heterostructure spin-orbit interaction only causes relaxation, but does not contribute to phase decoherence, so that in absence of other effects $T_2 = 2T_1$ to leading order in the spin-phonon interaction [93].

2.4.3 Voltage noise

Just like fluctuations in magnetic field lead to decoherence for spin rotations (and qubit operations in general) mediated by magnetic fields, voltage noise will cause errors for qubit operations under DC electrical control, such as the exchange operations in S - T_0 qubits [98, 116, 117] and exchange-only qubits [118, 119], and two-qubit operations in single spin [120, 121], S - T_0 [98, 122] and exchange-only qubits [123].

Charge noise in GaAs has long been recognized to have a detrimental effect on coherence, and various forms of charge noise have been identified to dominate under different conditions:

Pioro-Ladriere *et al.* found reduction of switching noise (random telegraph noise, RTN) in GaAs by applying a positive bias to depletion gates while cooling to Kelvin temperatures (called bias cooling) [124]. They proposed that this noise is due to leakage of electrons from gates into conduction band intermittently trapped at ionized donors (DX centers) near the active region. Bias cooling reduces switching noise by lowering gate operating voltages, creating thicker Schottky barrier due to frozen-in negative charge at ionized donors [124]. Likewise, Buizert *et al.* [125] showed large reduction of RTN, and noise in general, in GaAs by bias cooling and equivalently, a negative voltage on a global top gate. Without reduction noise is RTN³ with Lorentzian power spectrum, $S(f) \propto 1/f^2$ ($\partial \ln S(f)/\partial \ln f = 2$). With RTN eliminated the remaining noise showed $1/f$ power spectrum indicating an ensemble of fluctuators with a homogeneous distribution of switching times for uniform doping (for delta doping $S(f) \propto f^{-\beta}$ with $\beta < 1$ indicating non-uniform distribution of corner frequencies) [125]. Further, they confirmed trapping of charges tunneling from depletion gates through the Schottky barrier as a likely RTN source, but excluded DX centers from playing a role in charge trapping — rather, growth defects are charge traps, making this mechanism relevant beyond heterostructures [125].

The remaining noise in GaAs devices when RTN from gate leakage is suppressed, *e.g.* other sources of charge trapping/release and gate noise, will still contribute to decoherence. For a S - T_0 qubit in GaAs at temperature of 50 mK it was found that dephasing of exchange rotations was governed by voltage noise showing non-Markovian (non-white noise) behavior, leading to a power-law decay of exchange oscillations corresponding to noise spectral density $S(f) \propto f^{-\beta}$ with $\beta \sim 0.7$ and showing a temperature dependence tending to $\beta \sim 0$ for temperature of ~ 200 -300 mK [117].

Charge noise in InAs nanowires has not been investigated to nearly the same extent. RTN noise (two-level fluctuation) has been observed in InAs nanowires at temperatures between 30-80 K, and has been attributed to fluctuating occupation of defect states in the native oxide encapsulating the nanowire [126].

Measurements at a temperature of 2 K on a InAs nanowire in the open transport regime

³dominated by one or a few bi-stable charge traps close to QPC channel with characteristic switching times

indicate a $S(f) \propto 1/f$ noise spectrum changing to $1/f^2$ close to the threshold for depletion of carriers by a gate voltage for [127]. However, this behavior could change for quantum dots in nanowires and for lower temperatures.

Connections between spin state coherence and electrostatic noise in InAs nanowire quantum dots have not been investigated, but spin manipulation experiments in InAs double dots found that a fluctuating nuclear spin bath was likely the limiting factor for coherence [77]

The effect of electron occupation number of quantum dots on noise induced decoherence in general is an open question, as experiments so far have focused on a dot occupation of 1-2 electrons. In Section 5.4 data for initial studies of multi-electron double quantum dots for spin qubits are presented, preceded by a discussion of the possible beneficial effects of the multi-electron occupation on coherence.

The effect of sample processing on the low temperature gate stability for InAs nanowire devices is addressed in this thesis, see Section 4.3, page 66, however without connecting it to spin state decoherence.

2.5 Spin qubits in quantum dots

The electron spin is a promising candidate for a qubit since it is usually not coupled directly to the environment in a solid state environment, but is still, through the charge of the electron, easily confined and shuttled around via electric signals.

Since the proposal by Loss and DiVincenzo in 1998 [28] to base a quantum computer on electrons spins in quantum dots, with each qubit formed by one quantum dot containing a single electron spin, alternative proposals for qubits using electron spins in quantum dots have been put forward [97, 123, 128]. Next, I will describe the basis for the universal spin control in the single- [28] and two-electron qubits [97, 128] and briefly mention the three-electron qubit [123], since it is closely related to the two electron qubit in terms of operation.

2.5.1 Single-spin qubit: Loss-DiVincenzo qubit

In the so-called Loss-DiVincenzo qubit, a single electron spin makes up the qubit, the two-level system simply comprised by $|\uparrow\rangle$ and $|\downarrow\rangle$; the Zeeman split states of the spin in a large external field \mathbf{B}_0 defining the z -axis. Manipulation of the spin is achieved by electron spin resonance (ESR), which is rotation of the spin around a rotating magnetic field, \mathbf{B}_1 , applied perpendicular to the splitting field \mathbf{B}_0 , see Fig. 2.16 (a). The rotating field, B_1 , is rotating with frequency ω equal to the resonance frequency of the spin rotation in the Zeeman splitting field $\omega_L = g\mu_B B_0/\hbar$, known as the Larmor frequency (g is the electron-spin g -factor and μ_B the Bohr magneton, the unit of the magnetic moment of an electron). Fig. 2.16 (a) shows the motion of the electron spin (grey arrow) in the laboratory rest frame in response to the magnetic fields. Shifting to the electron rest frame (rotating at

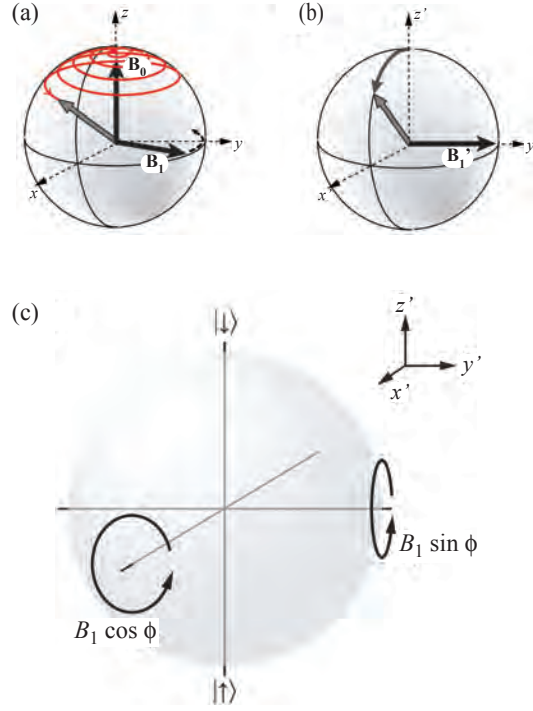


Figure 2.16: Bloch sphere representation of single-spin spin qubit. (a) Precession of spin about perpendicular resonant field in the laboratory frame. (b) Same as in (a) in the rest frame of the electron. (c) Spin rotations for the single spin qubit are performed by applying oscillating magnetic field, B_1 , perpendicular to the splitting field, the two axis set by the phase of the oscillation, see text. (a) and (b) adapted from [77], (c) adapted from [130].

the Larmor frequency about the z -axis), Fig. 2.16 (b), the motion of the spin is simply a rotation corresponding to a static magnetic field of magnitude B_1 in the x - y -plane with a frequency $\Omega = g\mu_B B_1/\hbar$ called the Rabi frequency. The “absolute” orientation of the field B_1 in the plane in the rotating frame is arbitrary, but by changing the phase, ϕ , of the applied rotating field the relative orientation of the field B_1 in the rotating frame shifts. Defining \mathbf{x} as parallel to \mathbf{B}_1 for $\phi = 0$ it can be shown that the spin in the rotating frame evolves as experiencing a static magnetic field [129]

$$\mathbf{B}'_1 = \frac{\hbar}{g\mu_B} \begin{pmatrix} \Omega \cos \phi \\ \Omega \sin \phi \\ \omega - \omega_L \end{pmatrix}. \quad (2.7)$$

For an applied field rotating with frequency $\omega = \omega_L$ the effective field is in the x - y -plane and by applying bursts of different phase, rotation about an arbitrary axis in the plane can be achieved, sufficient for arbitrary rotations of the spin on the Bloch sphere by combining rotation around different axis, Fig. 2.16.

Often, instead of a rotating field \mathbf{B}_1 , it is simpler to apply an oscillating field with frequency, ω_L ; decomposing the oscillating field into two counter-rotating fields with same frequency and magnitude $B_1/2$, it can be seen that for $B_0 \gg B_1$ one component will be on

resonance while the other will oscillate with frequency $2\omega_L = 2g\mu_B B_0/\hbar \gg \Omega = g\mu_B B_1/2\hbar$. The effect of the oscillating field will average out on the timescale Ω^{-1} , and the evolution of the spin in the rest frame will be described by the resonant component in analogy to Eq. (2.7).

As time-varying magnetic fields are technically difficult to apply locally on a nanometer scale as required for local control of individual qubits, electric dipole spin resonance (EDSR) has been used as an alternative to ESR for spin manipulation. In EDSR an oscillating electric field is used to “shake” the electron, and although the electric field does not directly couple to the spin, the presence of a spatially varying magnetic field will result in an oscillating magnetic field in the electrons rest frame. For an oscillating electric field on resonance with the spin splitting in the external field B_0 , the effective oscillating magnetic field will induce spin rotation similar to ESR. Both ESR [101] and EDSR mechanisms [25, 111, 131, 132] for arbitrary single spin rotations have been realized in single electron spin qubits. For EDSR, the source of the spatially varying magnetic field can be the spin-orbit interaction⁴ [25, 111], a micro-magnet aligned with the dot [131, 132] or the gradient in the (random) nuclear magnetic field [102]⁵. For EDSR mediated by spin-orbit interaction, the greater strength of the interaction in InAs compared to GaAs makes Rabi oscillations about an order of magnitude faster in InAs; for GaAs the highest Rabi frequency obtained in the original study was ~ 5 MHz [111], whereas it was ~ 60 MHz in an InAs nanowire qubit [25].

2.5.2 Two-electron qubit: S - T_0 qubit

In the two-electron qubit the two levels are the singlet S and the $m_S = 0$ triplet T_0 spin states of the (1, 1) charge configuration in a double quantum dot; Fig. 2.17 shows the Bloch sphere representation of the S - T_0 qubit. This qubit basis was originally proposed by Levy [128], as it would render the qubit immune to decoherence due to spatially uniform fluctuations in magnetic field. The S and T_0 states are separated from the T_{\pm} spin states by an applied magnetic field B_0 , see Fig. 2.10. The exchange energy splitting, J , between S and T_0 can be used to drive rotations around the z -axis (parallel to the external magnetic field). Rotations about the x -axis are mediated by a gradient in magnetic field between the two dots parallel to the Zeeman splitting field, ΔB_z ; this drives transitions between the S and T_0 spin states [133]. The magnetic field difference between the dots can be realized through a micro-magnet [134] or by a gradient in nuclear fields developed and stabilized by dynamical nuclear polarization (DNP) [135].

Most importantly, this means that the qubit can be operated by voltage pulses alone

⁴To first order in the spin-orbit interaction the effect can be accounted for by a position-dependent magnetic field, proportional and perpendicular to the external field [111].

⁵The random nuclear field can not be used to drive coherent oscillations as a stable gradient is needed, but it is sufficient for spin resonance measurements

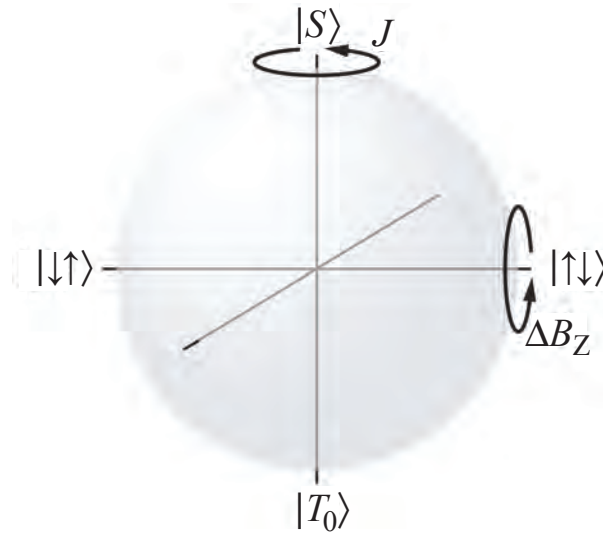


Figure 2.17: Bloch sphere representation of a S - T_0 spin qubit. Rotation around z and x are mediated by exchange coupling, J , and longitudinal magnetic field gradient, ΔB_Z , respectively. Adapted from [136]

on a sub-nanosecond timescale, as has been demonstrated for exchange operations alone [116, 117] and for both exchange and DNP gradient rotations [98, 135], which is significantly faster than for the ESR/EDSR controlled single qubit. This means that many more operations can be performed within the decoherence time (up to $\sim 200 \mu\text{s}$ in GaAs [137] and up to $\sim 200 \text{ ns}$ in InAs [25]) for the S - T_0 qubit, meeting the estimated requirement of 10^4 operation within the decoherence time for efficient error correction in a quantum computer [62].

2.5.3 Three-electron qubit: Exchange-only qubit

For the exchange-only qubit three spin over three quantum dots make up each qubit, but single- as well as two-qubit gates are mediated by the exchange coupling as the name “exchange-only” suggests [118, 119, 123]. This means that the qubit can be controlled via electrical pulses without the need for tricks such as DNP or micro-magnets to create magnetic field gradients.

2.5.4 Two-qubit operation and gates

For all three types of spin qubits, two-qubit operations between adjacent qubits are possible via the exchange interaction, thus implementing the SWAP-gate.

For the Loss-DiVincenzo qubit the operation of this two-qubit gate was recently demonstrated and benchmarked, thanks to the realization of simultaneous single-shot read-out of the spin in both quantum dots, allowing the coherent oscillations between the qubits to

be measured [121]. However, this experiment did not demonstrate single qubit operation, which was demonstrated, along with two-qubit entanglement via the exchange interaction, in another experiment on a GaAs Loss-DiVincenzo two-qubit system [120].

For the S - T_0 qubit it has also been predicted that simply the capacitive coupling between adjacent double-dot qubits is strong enough to allow universal quantum computation [97]. Toward this end, it was demonstrated that based on the charge state of a control qubit — (1,1) or (0,2) — the phase evolution of the exchange interaction in the target qubit could be shifted by π on a ~ 30 ns time-scale. This thus demonstrated the potential for a controlled phase gate between two S - T_0 qubits [122].

Recently, Shulman *et al.* [98] realized the controlled phase gate, creating an entangled state between the two qubits via their electrostatic coupling and the different charge distribution of the S and T_0 states.

So far no two-qubit operations have been demonstrated for qubits in InAs nanowires - however, the demonstration of coupling of a InAs nanowire qubit to a superconducting cavity [138] is promising with respect to coupling multiple qubits.

Chapter 3

Device fabrication and measurement setup

3.1 InAs nanowire device fabrication and measurement

The nanowire devices fabricated and measured for this thesis all consist of InAs nanowires resistively coupled to source and drain electrodes and capacitively coupled to a number of local gate electrodes and a global back gate. Measurements are performed on two types of devices with different geometries for the local gates to compare the response in electron transport through the nanowires to potentials applied to the gates. For the different gate geometries one has local gates on top of the nanowire, dubbed top gates, and the other has the nanowire on top of the local gates, dubbed bottom gates.

The fabrication of the bottom gated InAs devices was done by Attila Márton in collaboration with Shivendra Upadhyay and the author was kindly allowed to use one of these for the measurements presented in this thesis. The fabrication procedure for the bottom gated devices is included here for completeness and to allow comparison to the top gate fabrication procedure.

3.1.1 InAs nanowire device fabrication

Different fabrication procedures are used for the bottom and top gated devices. Here, we will first give a brief overview of the fabrication procedure for both types of device, with detailed descriptions and discussions of the different steps given subsequently.

For *top gated* devices, Fig. 3.1, nanowires are deposited from an isopropanol suspension onto a highly doped Si wafer capped with 500 nm SiO₂ (step 1, Fig. 3.1). The positions of the nanowires with respect to predefined alignment marks are determined using dark field optical microscopy and subsequently source and drain contacts are defined using e-beam lithography (EBL) and deposition of a Ti/Au (10/90 nm) bilayer (step 2, Fig. 3.1). Immediately prior to metal deposition, the native oxide cap on the nanowire is removed by an ammonium polysulphide etch[139]. After metal deposition, a $\simeq 15$ nm thick patch of e-beam lithographically defined HfO₂ is deposited on top of the nanowire by atomic

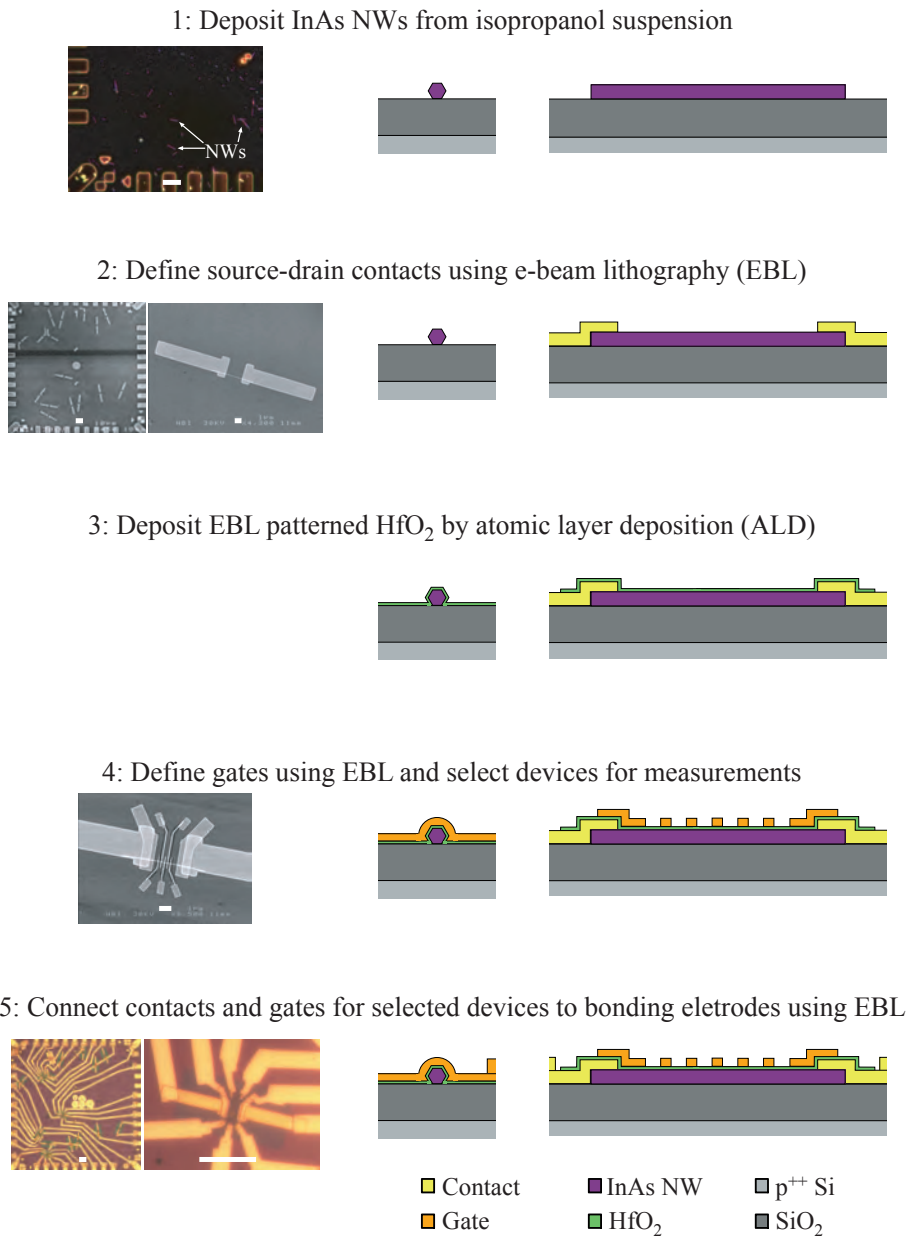


Figure 3.1: Main steps in fabrication of top gated InAs nanowire devices. The first column shows top view illustration of four of the five process steps in form of (from top to bottom) a dark field optical micrograph (scale bar 10 μm), two SEM images (scale bars 10 and 1 μm), a SEM image (scale bar 1 μm) and two optical micrographs (scale bars 10 μm). The remaining two columns show schematic cross sectional views across and along the nanowire axis, respectively, for a nanowire laying perpendicular to the gate axis. Thin gates (*top gates*) have width 100 nm and pitch 250 nm and the wider gates are $\sim 1 \mu\text{m}$ wide (*contact gates*).

layer deposition (ALD) at 130°C using a tetrakis(dimethylamido)hafnium precursor (step 3, Fig. 3.1). In a third e-beam lithography step the top gates are defined and a Ti/Au (10/50 nm) bilayer is deposited (step 4, Fig. 3.1). The thin top gates on the middle section of the wire are ~ 100 nm wide, have a pitch of 250 nm, and are hence referred to as *top gates*; the wider gates overlapping the wire/contact-interface are $\sim 1 \mu\text{m}$ wide and are hence referred to as *contact gates*. After checking for proper gate definition in low magnification scanning electron microscopy (SEM), S/D-contacts and gates are connected to bonding electrodes in a fourth EBL step (step 5, Fig. 3.1).

For the *bottom gated* devices, Fig. 3.2, the local gates are defined in the first e-beam lithography step (step 1, Fig. 3.2) and have widths $\simeq 45$ nm, pitch $\simeq 75$ nm and consist of a 5/10 nm Ti/Au bilayer on a highly doped Si wafer capped with 500 nm SiO₂. The gates are covered by 20 nm of e-beam lithographically defined HfO₂ deposited at 90°C (step 2, Fig. 3.1) prior to depositing the InAs wires from suspension (step 3, Fig. 3.1). The nanowires are identified and selected for correct positioning with respect to the local gates using an optical microscope, and S/D-contact electrodes and connections to the local gates are defined using e-beam lithography (step 4, Fig. 3.1). Again, an ammonium polysulphide etch is performed prior to deposition of 15/90 nm Ti/Au.

Nanowire deposition and contacts

Here we give a detailed description of the procedure for defining the source/drain contacts for both top and bottom gate devices. This is followed by a brief discussion of some of the steps in the procedure and an overview of other research groups approaches to contacting (and insulating) InAs nanowires.

Contacts for top gate devices

NW deposition: Wet deposition of NWs from IPA suspension

- Revive suspension by heating on hotplate briefly and 2-3s of ultrasound; swirl for ≈ 1 min while heating on hotplate for short intervals
- Deposit a small amount ($\sim 10 \mu\text{L}$) on target wafer with predefined alignment marks (enough to wet the surface completely, but not much more); evaporate solvent by gently blowing w/ N₂ from a distance of ~ 20 cm perpendicular to the surface; as droplets start to form move these around and blow them off the edge before they dry out as this leaves drying marks; check wire density under optical microscope and repeat deposition process until satisfactory

Sample cleaning: Three-step rinse in acetone, methanol, IPA; blow dry w/ N₂; bake for 5 min at 185°C on hotplate

Resist: Apply resist bilayer

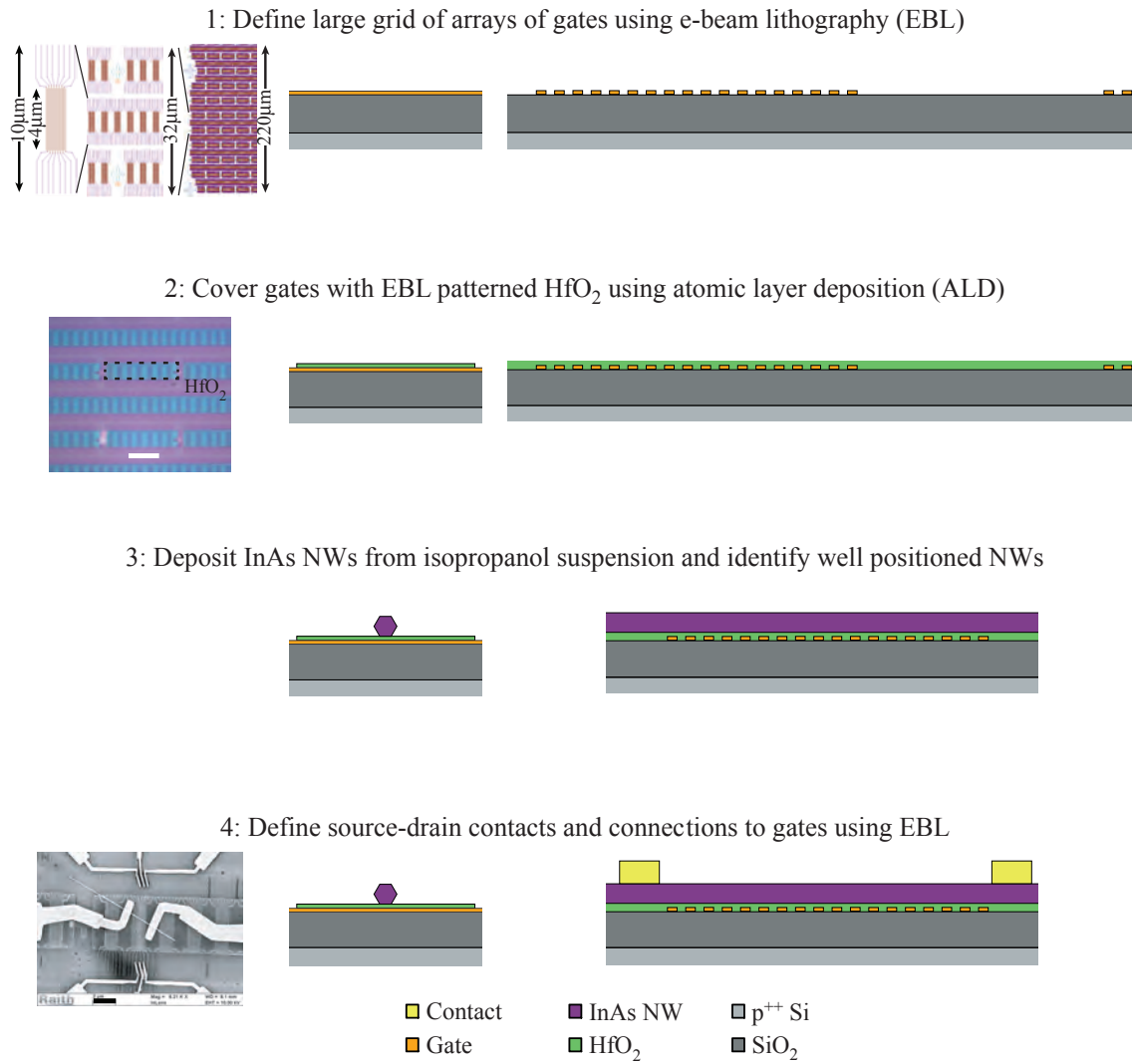


Figure 3.2: Main steps in fabrication of bottom gated InAs nanowire devices. The first column shows top view illustration of three of the four process steps in form of (from top to bottom) a CAD drawing, an optical micrograph (scale bar $10\ \mu\text{m}$) and a SEM image (scale bar $2\ \mu\text{m}$). The two remaining columns show schematic cross sectional views across and along the nanowire axis, respectively, for a nanowire laying perpendicular to the gate axis. Gates have widths $\simeq 45\ \text{nm}$ and pitch $\simeq 75\ \text{nm}$.

- 6% Copolymer, spin deposit at 4000 rpm for 40 s; bake for 90 s at 185 °C on hotplate → ~ 100 nm thick
- 2% PMMA, spin deposit at 4000 rpm for 40 s; bake for 90 s at 185 °C on hotplate → ~ 50 nm thick

Image and design: Image sample area ($200 \times 200 \mu\text{m}^2$) using optical microscope (dark field) to determine positions of NWs; design devices using CAD program

E-beam exposure: JEOL JSM-6320F scanning microscope

- acceleration voltage: 30 kV; aperture nr.= 4, constant current; WD: 8 mm; write field: 200 μm ; magnification: 400x; beam current: $\simeq 13\text{-}30 \text{ pA}$ falling off over a period of 2 h after flashing
- area dose: 250 $\mu\text{A s/cm}^2$; area step size: 1 pixel $\simeq 3 \text{ nm}$

Development: 50 s in 1:3 MIBK:IPA while swirling; rinse w/ IPA; blow dry w/ N_2

Ash: pumping down for 2 min; O_2 plasma ash for 20 s (etch rate: $\simeq 3\text{-}4 \text{ nm/s}$, no ashing in the first 2 s → $\simeq 60 \text{ nm}$ PMMA is removed)

Etch: (metals for deposition should be outgassed before etch) 5 sec etch at 40 °C in 20 % $(\text{NH}_4)_2\text{S}$ (stock solution) with 2.3 M S added; rinse w/ Millipore water for ~ 30 s; blow dry w/ N_2

Metal deposition: outgas materials before etching and loading sample; pump e-gun evaporator to $\sim 1 \times 10^{-7}$ torr

- 10 nm Ti, $\sim 0.5 \text{ \AA/s}$
- 70 nm Au, $\sim 2 \text{ \AA/s}$

Lift-off: acetone at RT for a few min; rinse w/ acetone from wash bottle; blow dry w/ N_2

Contacts for bottom gate devices:

NW deposition: Wet deposition of NWs from IPA suspension

- Revive suspension by heating on hotplate briefly and 2-3 s of ultrasound; swirl for $\approx 1 \text{ min}$ while heating on hotplate for short intervals
- Deposit a small drop on target wafer with predefined alignment marks and bottom gates (enough to wet the surface completely, but not much more); evaporate solvent by gently blowing w/ N_2 from a distance of $\sim 20 \text{ cm}$ perpendicular to the surface; as droplets start to form move these around

and blow them off the edge before they dry out as this leaves drying marks; check for wires positioned across predefined gate structure in an optical microscope and repeat deposition process if necessary

Sample cleaning: Three-step rinse in acetone, methanol, IPA; blow dry w/ N₂; bake for 5 min at 185 °C on hotplate

Resist: Allow wafer to cool and apply resist bilayer

- 9% Copolymer, spin deposit at 4000 rpm for 60 s; bake for 3 min at 185 °C on hotplate → ~ 325 nm thick; allow to cool before next deposition
- 2% PMMA, spin deposit at 4000 rpm for 60 s; bake for 3 min at 185 °C on hotplate → ~ 50 nm thick

Image and design: Image nanowires chosen for contacting in SEM to determine positions of NWs with respect to alignment marks; draw connections to nanowire and to gates using CAD program

E-beam exposure: Raith e_LiNE

- acceleration voltage: 30 kV; aperture size: 20 μm; current: 0.13-0.14 nA; stage height: 26 mm; write field: 50 μm; magnification: 200x
- area dose: ~ 290 μA s/cm²; area step size: 32 nm

Development: 60 s in 1:3 MIBK:IPA while flushing w/ N₂ bubbles; IPA flushing for 15 s; check development in optical microscope; blow dry w/ N₂

Ash: pumping down for 2 min; O₂ plasma ash for 20 s (etch rate: \simeq 3-4 nm/s, no ashing in the first 2 s → \simeq 60 nm PMMA is removed)

Etch: (metals for deposition should be outgassed before etching) 5 sec etch at 40 °C in 20% (NH₄)₂S (stock solution) with 2.3 M S added; rinse w/ Millipore water for ~ 30 s; blow dry w/ N₂

Metal deposition: outgas materials before loading sample; pump e-gun evaporator to ~ 6-8 × 10⁻⁸ torr

- 15 nm Ti, ~ 1 Å/s
- 120 nm Au, ~ 2 Å/s

Lift-off: acetone at ~ 50 °C for a few min; rinse w/ acetone from wash bottle; blow dry w/ N₂

Materials and methods:

The chemicals used for all EBL steps are 9% Copolymer MMA (8.5) MAA (diluted to give

lower concentrations) and 2% 950PMMA A both from MicroChem; 1:3 methyl isobutyl ketone/isopropanol (1:3 MIBK/IPA) from MicroChem; and Remover PG from MicroChem. For the nanowire etch prior to contact deposition we used an ammonium sulphide stock solution, 20%-wt $(\text{NH}_4)_2\text{S}$ in H_2O , from Sigma-Aldrich.

The suspension of NWs in isopropanol (IPA) is made by cutting a small piece of growth wafer ($\sim 2 \times 2 \text{ mm}^2$) with a high density of wires and put it in a glass vial along with $\sim 1 \text{ mL}$ of IPA. The wires are broken off the wafer by $\sim 10 \text{ s}$ of ultrasound. The suspension should be good for many depositions, as each only uses a tiny drop and additional IPA can be added to the suspension. Wet deposition from suspension of InAs nanowire in IPA gives a uniform distribution of wires on the target wafer, but can also leave debris such as fragments of the growth wafer and occasionally drying marks.

As an alternative to wet deposition, dry (mechanical) deposition of wires is also possible. One method we have previously used: Use a small triangle of Pro-Wipe cleanroom tissue to lightly touch NW growth wafer; transfer to target area on sample wafer with a light touch; check deposition in optical microscope and repeat deposition if necessary. Dry (mechanical) deposition can lead to more fragmentation of wires, but offers more control over deposition area although wires can have a tendency to cluster.

An improved method in terms of control would be positioning of individual nanowires by micromanipulators; as only a small number of devices ($\sim 3\text{-}10$) are produced in each fabrication run it is feasible to position the individual wires in this fashion.

The etch performed prior to contact metal deposition is to remove the native oxide from the nanowire [139–141]. The stability of the etching solution is limited (especially at temperatures $> 40^\circ\text{C}$), so only prepare a small amount; dissolve sulphur by swirling and sonicating, not by heating; and do not reuse for multiple etchings unless in straight succession (bright orange color of the etch solution should disappear with degradation of solution [139]). We have used a brief etch in a concentrated polysulphide solution, since this approach was the first successful after failed attempts with a highly diluted (1:500) solution of the stock solution. For future devices we would prefer a slightly diluted etching solution with a longer treatment time, since this would likely give better control and repeatability than a few second etch.

Also, regarding wire conductance, it has been observed that keeping the finished device in vacuum for $\sim 24\text{-}48 \text{ h}$ before cooling down can increase the conductance by around a factor of 10, likely due to desorption of water and other physisorbed molecules that affect charge density and mobility in the wire through creation of surface states [77, 142–144]. We speculate that the same effect could affect the quality of the ohmic contacts, and would generally recommend keeping the sample at high vacuum ($\sim 10^{-7}\text{-}10^{-8} \text{ Torr}$) for at least a couple of hours, and preferentially overnight, before depositing the metal contacts¹.

¹Although this could be hard to negotiate with other cleanroom users.

Chapter 3. Device fabrication and measurement setup

Performing a literature search shows that different groups working with InAs nanowires have slightly different fabrication procedures. Some differences are related to different applications of the devices (especially metals used for contacting wires), but for all but a few purposes a low contact resistance ($\sim 1\text{-}10\text{ k}\Omega$), high device stability and efficient gating are desirable characteristics.

Here we list the selected details regarding obtaining ohmic contacts (and wire/gate insulation) from the fabrication methods reported for a number of groups (Institution, City (State), Country (Group leader)) working with InAs nanowires,

Lund University, Lund, Sweden (L. Samuelson):

Dry deposition; highly diluted (1:500) $(\text{NH}_4)_2\text{S}_x:\text{H}_2\text{O}$ at 62°C for 30 min [139]; or diluted (1:9) $(\text{NH}_4)_2\text{S}_x:\text{H}_2\text{O}$ at 40°C for 2-3 min [145, 146]; Ni/Au contacts; gate insulation 25 nm SiN_x by PECVD [147].

Delft University of Technology, Delft, The Netherlands (L.P. Kouwenhoven):

Dry deposition; 5-6 s buffered hydrogen fluoride (HF) etch [148, 149]; or 10-15 s HF etch and pump on device for two days at RT to lower two-terminal resistance by 2-3 orders of magnitude (presumably due to desorption of physisorbed molecules that affect mobility or charge density by creating surface states) [77, 143]; Ti/Al contacts; gate insulation by 20 nm Si_3N_4 by sputtering [77, 143].

University of Copenhagen, Copenhagen, Denmark (J. Nygård):

Wet deposition (methanol); or dry deposition; 5 s HF etch, Ti/Au contacts [150]. Also, wet deposition (IPA); 5 s etch in undiluted (20%) $(\text{NH}_4)_2\text{S}_x$ w. 2.3 M elemental S; top- and bottom gate insulation by $\sim 20\text{ nm}$ ALD HfO_2 (this work, see [151])

ETH Zurich, Zurich, Switzerland (K. Ensslin):

Wet deposition (ethanol) or dry deposition, Highly dil. (1:1000) $(\text{NH}_4)_2\text{S}_x:\text{H}_2\text{O}$; Ti/Au contacts; (top)gate insulation by $\simeq 2\text{ nm}$ native oxide [152, 153].

University of Basel, Basel, Switzerland (C. Schönenberger):

Wet deposition (IPA); “gentle” Argon sputtering in metallization chamber; Ti/Au contacts; (top)gate insulation by native oxide [154, 155].

Princeton University, Princeton (NJ), USA (J. Petta):

Wet deposition (ethanol); diluted (1:333) $(\text{NH}_4)_2\text{S}_x:\text{H}_2\text{O}$ at 62°C for 30 min; Ti/Au contacts, annealing at 200°C for 1 min; factor of ~ 2 increase in device conductance by keeping it in vacuum prior to cooling; gate insulation by 20-25 nm SiN_x by PECVD [144, 156].

UCSD, La Jolla (CA), USA (D. Wang):

Wet deposition (ethanol); 15 s HF etch; Ti/Al contacts [157]. (However,

in most papers it seems no etching was used, and still few $k\Omega$ resistance were obtained — even down to $\sim 700 \Omega$ for 50-100 nm diameter nanowires [158]!)

UCB, Berkeley (CA), USA (A. Javey):

Wet deposition (ethanol); 5 s HF etch ($\sim 0.1\%$); Ni contact, annealing at 250°C for 1 min [159]; or Ni/Au contact w/o annealing and surface passivation w/ ALD of 7 nm ZrO_2 and 1.1 μm photoresist [160].

CWRU, Cleveland (OH), USA (X. P. A. Gao):

Wet deposition (IPA); 3 s HF etch; Ti/Al contacts [127, 161].

TIFR, Mumbai, India (Mandar M. Deshmukh):

Wet deposition; low power plasma etching in metal deposition chamber [162]; or $(\text{NH}_4)_2\text{S}_x$ treatment [163]; Cr/Au contacts.

Braun Center for Submicron Research, Rehovot, Israel (H. Shtrikman):

Wet deposition (ethanol); $(\text{NH}_4)_2\text{S}_x$ etch; Ni/Au contacts w/ suspended geometry; high vacuum leads to significant increase in conductance (factor 10) [142, 164], cf. Delft above.

NEST, Pisa, Italy (F. Beltram) and IOM-CNR, Trieste, Italy (S. Roddaro):

Highly diluted $(\text{NH}_4)_2\text{S}_x$ at 44°C ; GeAu/Au contacts and annealing at 250°C for 30 s [165]; or Ti/Au contacts [166].

CEA, Grenoble, France (S. De Franceschi):

InAs/InP core/shell ($\sim 28/2 \text{ nm}$) nanowires; Argon sputtering; Ti/Al contacts [167]

In summation a few things are worth noting:

- Wire deposition is done both from suspension (methanol, ethanol or isopropanol) and by mechanical transfer with success;
- Four different processes are used for oxide removal: two wet etches (HF and $(\text{NH}_4)_2\text{S}_x$) and two *in vacuo* processes (Argon sputtering and plasma etching);
- Metal contacts generally consist of a wetting layer (Ti, Ni, Cr) and a thicker top “functional” layer depending on specific application (usually Au for normal metal and Al for superconducting);
- Individual groups have tried multiple procedures, indicating a suboptimal current processing procedure;
- The processing schemes do not seem to be converging to a single, shared recipe.

The main conclusion that I would draw from this is that the formation of low resistance, ohmic contacts is likely not dependent on the choice of a specific method for the mentioned processes (deposition, etching, metallization), but rather some other aspect of processing. Our best guess is that the determining step is cleaning of the contact surface of the wire in terms of resist residue and adsorbed molecules. Normally resist residues persisting after lift-off should not be an issue as this should be stripped by the O₂ plasma ashing step. Surface adsorbed molecules should be desorbed prior to metal deposition by keeping the sample at a high vacuum for some time (preferably over night) prior to metal deposition.

Gates

The top and bottom gated devices were produced on different e-beam lithography systems; the top gate devices were produced on a JEOL JSM-6320F, the only EBL system at the Nano-Science Center at the beginning of my Ph.D.; the bottom gate devices were produced on a Raith e_LiNE system that arrived at the Nano-Science Center as I was about to leave for Harvard towards the end of 2010. The production of bottom gate devices sets specific requirements to the e-beam lithography system, since the stochastic nature of nanowire deposition means that a large area of predefined bottom gates is needed to have an acceptable yield of nanowires correctly positioned across the gates. The production of a large area ($\sim \text{mm}^2$) with repeated patterns of thin, closely spaced gates is accomplished by doing very precise stitching of smaller write fields; a process that was not possible on the old e-beam system (JEOL).

Here we give a detailed description of the procedures for defining the top and bottom gates.

Top gates:

Sample cleaning: Three-step rinse in acetone, methanol, isopropanol (IPA); blow dry w/ N₂; bake for 5 min at 185 °C on hotplate

Resist: Apply resist bilayer

- 6% Copolymer, spin deposit at 4000 rpm for 40 s; bake for 3 min at 185 °C on hotplate → ~ 100 nm thick
- 2% PMMA, spin deposit at 4000 rpm for 40 s; bake for 3 min at 185 °C on hotplate → ~ 50 nm thick

E-beam exposure: JEOL JSM-6320F scanning microscope

- acceleration voltage: 30 kV; aperture nr. = 4, constant current; WD: 8 mm; write field: 200 μm ; magnification: 400x; beam current: $\simeq 13\text{-}30$ pA falling off over a period of 2 h after flashing
- line dose: 1700 pA s/cm; line step size: 1 nm
- area dose: 200 $\mu\text{A s/cm}^2$; area step size: 1 pixel $\simeq 3$ nm

Development: 50 s in 1:3 MIBK:IPA while swirling; rinse w/ IPA; blow dry w/ N₂

Ash: pumping down for 2 min; O₂ plasma ash for 10 s (etch rate: \simeq 3-4 nm/s, no ashing in the first 2 s \rightarrow \simeq 30 nm PMMA is removed)

Metal deposition: outgas materials before loading sample and pump e-gun evaporator to $\sim 1 \times 10^{-7}$ torr

- 10 nm Ti, $\sim 0.5 \text{ \AA/s}$
- 50 nm Au, $\sim 2 \text{ \AA/s}$

Lift-off: in acetone at $\simeq 40^\circ\text{C}$ for 4 min; brief (3-5 s) ultrasound; rinse w/ acetone from syringe; repeat ultra sound and syringe rinse until lift-off seems satisfactory in optical microscope (sample immersed in IPA)

Bottom gates:

Sample cleaning: O₂ plasma ash for 2 min; three-step rinsing in acetone, methanol and IPA; blow dry w/ N₂; bake for 5 min at 185 °C on hotplate

Resist: Apply single layer resist

- 2% PMMA spin deposited at 4000 rpm for 60 s, baked for 16 min at 185 °C \rightarrow ~ 50 nm thick

E-beam exposure: Raith e_LiNE

- acceleration voltage: 30 kV; aperture size: 20 μm ; current: 0.13-0.14 nA; stage height: 26 mm; write field: 50 μm ; magnification: 200x
- line dose: $\sim 880 \text{ pA s/cm}$; line step size: 1 nm, w/ good stigmation, focus (using 3 point focus correction) and write field alignment
- area dose: $\sim 250 \mu\text{A s/cm}^2$; area step size: 32 nm
- curved element dose: $\sim 230 \mu\text{A s/cm}^2$; step size: 16 nm

Development: 45 s in 1:3 MIBK:IPA while flushing w/ N₂ bubbles; IPA flushing for 15 s; blow dry w/ N₂

Ash: pumping down for 2 min; O₂ plasma ash for 8 s (etch rate: \simeq 3-4 nm/s, no ashing in the first 2 s \rightarrow \simeq 20 nm PMMA is removed)

Metal deposition: outgas materials before loading sample

- 5 nm Ti, $\sim 0.3 \text{ \AA/s}$
- 10 nm Au, $\sim 1 \text{ \AA/s}$

Lift-off: Remover PG for at least 2 hours at 75 °C; leave overnight in Remover PG at RT; rinse w/ Millipore water for 30 s; blow dry w/ N₂

Atomic layer deposition of HfO₂

To insulate the nanowires from the local gates — top or bottom — a layer of HfO₂ was deposited by atomic layer deposition (ALD). Alternatives to this include ALD of Al₂O₃, sputtering of silicon nitride (Si₃N₄) [77, 143] or plasma enhanced chemical vapor deposition (PECVD) of silicon nitride (SiN_x) [144, 147], and usage of the native oxide on the nanowires, although it has a rather low break down voltage ($\simeq \pm 1$ V)[153, 154].

Here we give the details of the process for depositing EBL patterned HfO₂ for both top and bottom gated devices.

HfO₂ for top gate devices:

Sample cleaning: Three-step rinse in acetone, methanol, isopropanol (IPA); blow dry w/ N₂; bake for 5 min at 185 °C on hotplate

Resist: Apply resist bilayer

- 3% Copolymer, spin deposit at 4000 rpm for 40 s; bake for 90 s at 185 °C on hotplate → ~ 40 nm thick
- 2% PMMA; spin deposit at 4000 rpm for 40 s, bake for 90 s at 185 °C on hotplate → ~ 50 nm thick

E-beam exposure: JEOL JSM-6320F scanning microscope

- acceleration voltage: 30 kV; aperture nr.= 4, constant current; WD: 8 mm; write field: 200 μm; magnification: 400x; beam current: $\simeq 13$ -30 pA falling off over a period of 2 h after flashing
- area dose: 250 μA s/cm²; area step size: 1 pixel $\simeq 3$ nm

Development: 50 s in 1:3 MIBK:IPA while swirling; rinse w/ IPA; blow dry w/ N₂

Ash: pumping down for 2 min; O₂ plasma ash for 20 s (etch rate: $\simeq 3$ -4 nm/s, no ashing in the first 2 s → $\simeq 60$ nm PMMA is removed)

ALD: Cambridge NanoTech Savannah s100 ALD system using a tetrakis-(dimethylamido)hafnium precursor

- 100 cycles at 130 °C → ~ 15 nm oxide

Lift-off: acetone at $\simeq 40^\circ\text{C}$ for 20 min; 5 s ultrasound in acetone at 40°C ; rinse w/ hot acetone from syringe; repeat ultra sound and syringe rinse until lift-off is satisfactory; flush w/ IPA; blow dry w/ N_2

HfO₂ for bottom gate devices:

Sample cleaning: O_2 plasma ash for 2 min; three-step rinsing in acetone, methanol and IPA; blow dry w/ N_2 ; bake for 5 min at 185°C on hotplate

Resist: Apply resist bilayer

- 6% Copolymer, spin deposit at 4000 rpm for 45 s; bake for 3 min at 185°C on hotplate $\rightarrow \sim 100$ nm thick
- 2% PMMA, spin deposit at 4000 rpm for 45 s; bake for 3 min at 185°C on hotplate $\rightarrow \sim 50$ nm thick

E-beam exposure: Raith e_LiNE

- acceleration voltage: 20 kV; aperture size: $120\ \mu\text{m}$; stage height: 24 mm; write field: $200\ \mu\text{m}$; magnification: 50x
- area dose: $\sim 200\ \mu\text{A s}/\text{cm}^2$; area step size: 128 nm

Development: 45 s in 1:3 MIBK:IPA; IPA flushing for 15 s; blow dry w/ N_2

Ash: pumping down for 2 min; O_2 plasma ash for 17 s (etch rate: $\simeq 3\text{-}4$ nm/s, no ashing in the first 2 s $\rightarrow \simeq 50$ nm PMMA is removed)

ALD: Cambridge NanoTech Savannah s100 ALD system using a tetrakis-(dimethylamido)hafnium precursor

- 250 cycles at 90°C $\rightarrow \sim 20$ nm oxide

Lift-off: Remover PG for at least 2 hours at 75°C ; 10-20 s ultra sound pulses can help lift-off; rinse w/ Millipore water for 30 s; blow dry w/ N_2

The thicknesses of the HfO_2 layers for both top and bottom gated devices were determined from atomic force microscopy line scans of layers deposited using the same respective recipes, see Fig. 3.3 (c).

The use of a 3% Copolymer for the EBL patterning of the HfO_2 for the top gated devices was due to an issue with protruding edges on the defined patches after lift-off causing later deposited metal leads running across to be broken. This was observed for the initial process for ALD patterning for top gated devices using a 6% Copolymer/2% PMMA bilayer. Fig. 3.3 (a) and (b) show scanning electron microscope (SEM) micrographs of 10/90 nm Ti/Au

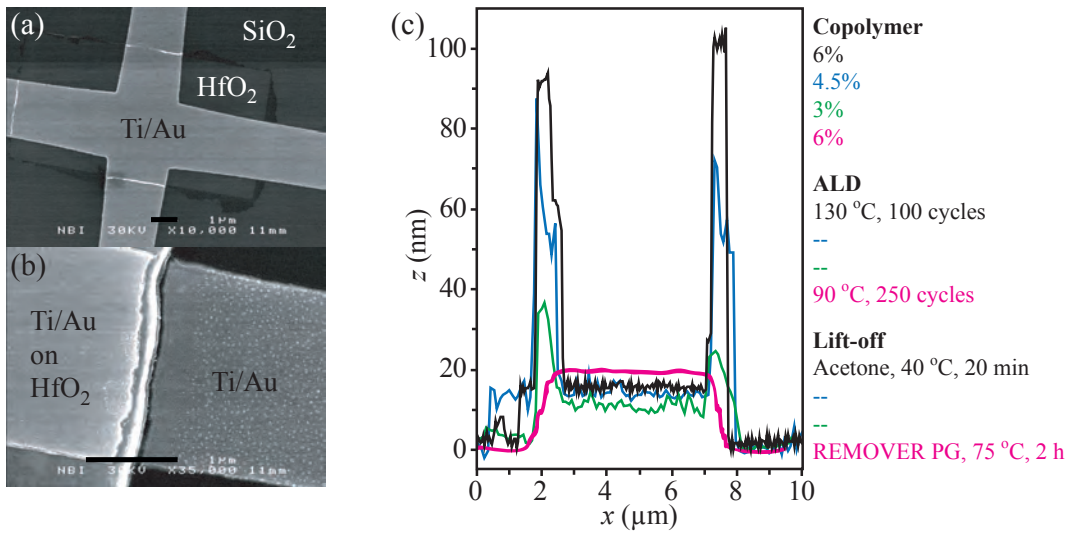


Figure 3.3: Effects of HfO₂ patterning and deposition conditions on height, z , profiles. (a) Scanning electron microscope (SEM) image of 10/90 nm Ti/Au leads running across the edges of a patch of HfO₂ produced under conditions corresponding to the black graph in (c). (b) Same as (a) showing a closer view of a lead crossing a HfO₂ edge leading to a gap in the lead. Scale bars in (a) and (b) are 1 μm. (c) Height profiles for 5 μm wide HfO₂ patches for different e-beam lithography and atomic layer deposition (ALD) conditions. Traces for 130 °C ALD are measured with atomic force microscopy, and for 90 °C ALD with an AlphaStep profilometer by Attila Márton. Edges are present for all but the 90 °C ALD and seem to scale with Copolymer concentration for the 130 °C HfO₂.

leads crossing onto such a patch of HfO₂ on a p⁺⁺ Si/SiO₂ substrate. In (a) it can be seen that at three out of the four crossings protruding HfO₂ edges are present, seen as white features across the leads, and this can cause a gap in the lead, Fig. 3.3 (b), due to shadow effects during metal deposition. Atomic force microscope (AFM) line profiles of HfO₂ patches produced using same recipes as listed above are shown in Fig. 3.3 (c), with the variations in the recipes denoted for each of the four traces; variation are with respect to the “top gate HfO₂ recipe” for the three first and with respect to the “bottom gate HfO₂ recipe” for the last. By using a lower concentration Copolymer solution the height of the edge on 130 °C HfO₂ diminishes; noting that the height of the 6% Copolymer is ~ 100 nm it is likely that the scaling of the height of the edge with the Copolymer concentration reflects the reduced height of the Copolymer at lower concentrations. For the 3% Copolymer the height of the edge is ~ 30-40 nm, which is low enough for the 10/90 nm Ti/Au leads to cross without being broken. However, comparing to the 90 °C ALD HfO₂, the 3% Copolymer process is still not optimal, as no edges are present for the 90 °C ALD — whether this difference is due to a higher stiffness/tensile strength of the 130 °C HfO₂ or due to a better left-off process for the 90 °C HfO₂ is unclear.

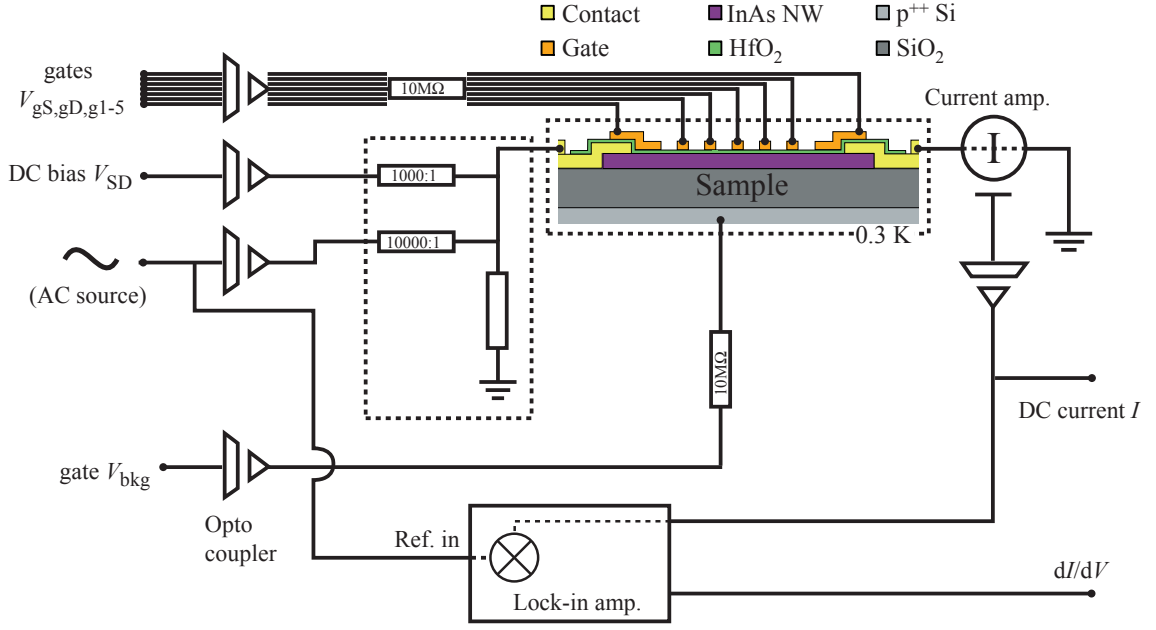


Figure 3.4: Schematic representation of the measurement setup used for the InAs nanowire measurements. Voltages were controlled from a computer running LabVIEW. Opto-couplers isolate the device from the computer. Adapted and modified from [168]

3.1.2 InAs nanowire measurement setup

A very basic measurement setup was used for the measurements on InAs nanowires, see Fig. 3.4. Conductance was measured with standard lock-in detection technique at an ac voltage bias (V_{SD}) of $100 \mu\text{V}$ with possibility for adding a dc bias for bias spectroscopy measurements. Current was measured in response to an applied dc bias only. Voltages (dc) are applied and measured using a PC running LabVIEW software and equipped with a National Instruments data acquisition (DAQ) card (National Instruments, BNC2110). Devices were cooled in a cryogen-free HelioxAC-V ^3He refrigerator from Oxford Instruments with a base temperature of $\simeq 0.3\text{K}$ and a hold time of ~ 20 hours. Temperature dependence was measured during cool down over a period of ~ 12 hours.

Contact gates and built-in barriers at nanowire-contact interface

A prerequisite for most measurements is good ohmic contact to the nanowire, and although chemical processing schemes for obtaining such contacts have been reported [139], experience shows that the yield often is low. It is possible that a contact gate, see Fig. 3.1, can alleviate wire/contact barrier problems that persist despite the chemical processing, increasing the yield of low resistance ohmic contacts to nanowires and in general allowing tuning of the wire/contact-coupling.

Figure 3.5 (a)–(c) show room temperature measurements of I vs V_{SD} for the top gated device TG0 that deviates from the described fabrication of top gated devices in only having one 300nm wide top gate, V_{tg} , see insert to (a). Panel (a) shows that transport through

the wire is blocked for zero voltage on top and contact gates, V_{gSD} , as well as the global back gate, V_{bkg} .

The reason for the asymmetry of the blockade in V_{SD} is not clear, but we see that the blockade can be lifted by applying a positive voltage, $V_{\text{gSD}} = 1 \text{ V}$ to the contact gates. That this is a specific effect of the contact gates is shown by applying similar voltages to the top gate with $V_{\text{gSD}} = 0 \text{ V}$, which only modifies the barrier slightly, Fig. 3.5 (b). Applying the same voltages to the top gate with $V_{\text{gSD}} = 1 \text{ V}$ shows that the top gate does in fact have an effect on the resistance of the nanowire as in this case the resistance of the wire is changed significantly, being $\sim 70 \text{ k}\Omega$ for $V_{\text{tg}} = 1 \text{ V}$, see Fig. 3.5 (c).

Such a different effect of the gates is also seen at low temperature, $T = 3 \text{ K}$, for the top gated device TG3 with the five top gates $V_{\text{g1-g5}}$ grounded in a lock-in measurement of G vs V_{bkg} with $V_{\text{SD,ac}} = 100 \mu\text{V}$, Fig. 3.5 (d); while the back gate is efficient at modulating the carrier density for $V_{\text{gSD}} \geq 0$, the wire is pinched off irrespective of V_{bkg} already at $V_{\text{gSD}} = -80 \text{ mV}$. Part of the inefficiency of the back gate in lifting the induced barrier at the wire/contact interface is likely due to shielding of the interface by the contact gates, but the contacts themselves have the same effect in the absence of contact gates [142, 169]. Note also that a negative potential on V_{gSD} was needed to create a barrier in (d), whereas a barrier was present in (a) even for $V_{\text{gSD}} = 0$; barriers are present only in some instances and sometimes only at one of the two contacts. Another effect associated with poor contacts is “freezing out” of devices, where a device conducting at room temperature pinches off as it is cooled down.

Fig. 3.5 (e) shows the effect of the source contact gate, g_s , on the conductance, G , of the top gated device, TG1, in response to $V_{\text{SD,ac}} = 100 \mu\text{V}$ as a function of temperature. The remaining gates are applied positive voltages to avoid formation of barriers here. A vertical dashed line at $V_{g_s} = 1 \text{ V}$ separates the plot into two regions, I and II, showing different temperature dependencies.

In region I, for gate voltages $V_{g_s} > 1 \text{ V}$, the conductance is independent of temperature, increases with gate voltage over the temperature range investigated and does not show saturation up to $V_{g_s} = 3 \text{ V}$.

In region II, $V_{g_s} < 1 \text{ V}$, the conductance drop with decreasing gate voltage is temperature dependent, yielding a pinch-off voltage that decreases from $V_{g_s} \approx 0.5 \text{ V}$ at $T = 3 \text{ K}$ to $V_{g_s} \approx -3 \text{ V}$ at $T = 225 \text{ K}$; for $V_{g_s} = 0$ this would lead to the “freezing out”. From measurements on quantum dots in InAs nanowires, it is known that barriers can form at wire/contact interfaces in response to carrier depletion using a global back-gate [142, 150]. The pinch-off at positive contact gate voltage in region II is consistent with the presence of a barrier at the nanowire/contact interface even in the absence of a depleting gate voltage, and the barrier thus appears to be built into the assembled nanowire-contact structure.

Such “built-in” barriers are likely the results of imperfect contact processing and are only seen for some of the top gated devices measured in this work. The lack of contact gates for the bottom gated devices impairs the observation of “built-in” barriers in these devices as measurements are only possible for devices without such a barrier. The contact gate

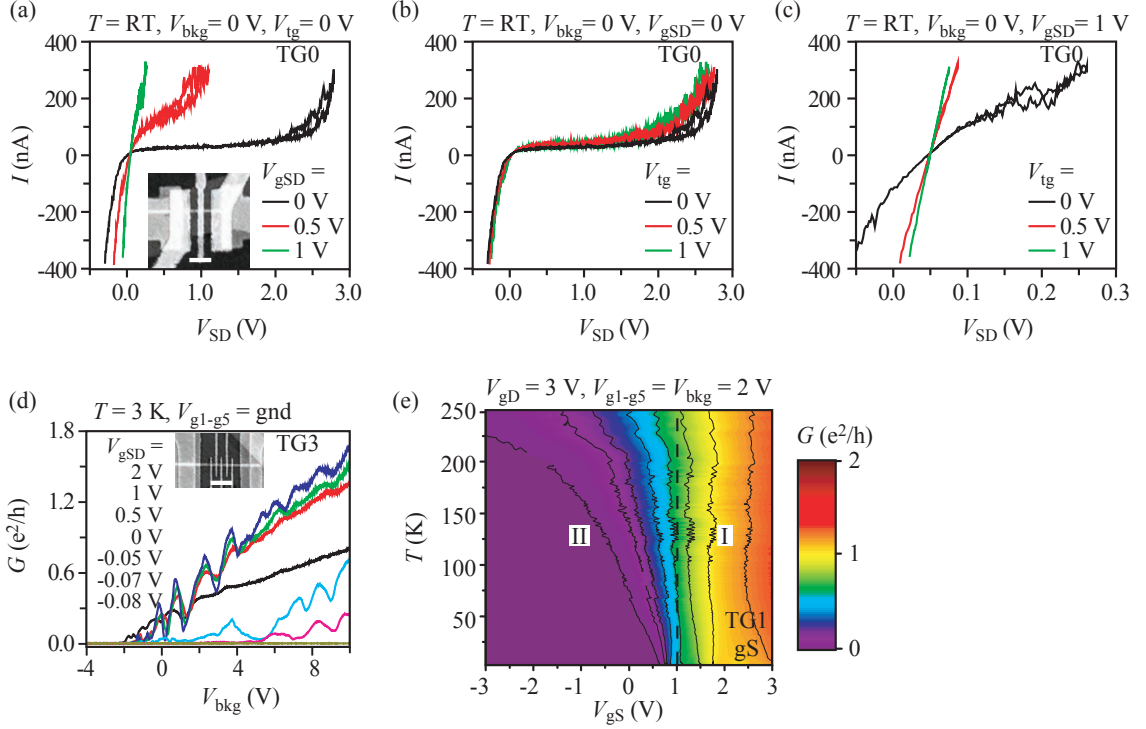


Figure 3.5: The effect of source/drain-contact gates, V_{gS} and V_{gD} , respectively, on the transport characteristics of top gated nanowires. V_{gSD} denotes voltages applied to both contact gates and V_{bkg} to the global back gate. (a) I vs V_{SD} for top gated device TG0 for different V_{gSD} . Insert shows SEM image of the device, scale bar $1\ \mu\text{m}$. (b) Same as (a) only for different V_{tg} with $V_{gSD} = 0\ \text{V}$. (c) Same as (b) only with $V_{gSD} = 1\ \text{V}$. (d) G vs V_{bkg} for top gated device TG3 at $T = 3\ \text{K}$ for different V_{gSD} . Insert shows SEM image of the device, scale bar $1\ \mu\text{m}$. (e) Effect of the source contact gate, g_S , on the conductance of the top gated device, TG1, as a function of temperature with $V_{gD} = 3\ \text{V}$ and $V_{g1-5} = 2\ \text{V}$. Roman numerals and dashed lines indicate regions with specific trends.

is able to enhance or remove the “built-in” barrier; applying a positive gate voltage up to $V_{gs} \sim 1$ V in Fig. 3.5 (e) diminishes the effect of the built-in barrier by lowering its height until it is below the electrochemical potential; applying a negative gate voltage increases the barrier height above the electrochemical potential adding to the blockade of transport.

Hence, the contact gate increases the device yield by allowing transport measurements in devices where “built-in” contact barriers would otherwise block transport and additionally allows independent tuning of the nanowire/contact coupling. The origin of the contact barrier has not been identified, but based on the observed differences in contact properties between ideally identical devices, it seems likely that the reason is non-ideal processing resulting in only partial oxide removal from and cleaning of the nanowire surface prior to metal deposition.

We note that we see a temperature dependence similar to that in Fig. 3.5 (e) region II for barriers induced by applying negative voltages to the local gates, see Section 4, page 55.

3.2 GaAs/AlGaAs heterostructure device fabrication and measurement

3.2.1 GaAs/AlGaAs heterostructure device fabrication

The fabrication of the GaAs/AlGaAs heterostructure devices measured in Marcus Lab at Harvard University was done entirely by Dr. Javad Shabani and followed a general fabrication recipe for lithography on a GaAs 2DEG, see e.g. Ref. [136].

A very brief description of the procedure for device fabrication is included here, with a few additional details of the deposition of the magnetic gate structure:

MESA etch Photolithography, bake, etch in $\text{H}_3\text{PO}_4:\text{H}_2\text{O}_2:\text{H}_2\text{O}$ 1 : 1 : 80 for 1 min

Ohmics Photolithography, evaporate metal, anneal

Magnetic gates

Define structure Resist ZEP520A:Anisole 1:3, EBL design

Metallize Evaporate Ti/Co/Au 2 nm/30 nm/5 nm

Lift off In acetone for 2 min and then acetone:trichloroethylene TCE for four hours, wash off w IPA

Connecting layers Photolithography with negative resist, metallize, lift off

The GaAs/Al_{0.3}Ga_{0.7}As heterostructure used in the GaAs experiments described in this thesis were grown by Borzoyeh Shojaei in the Chris Palmstrøm group at UCSB. These wafers are different from that shown in Fig. 2.3 in one important aspect; the 2-DEG

is located only 57 nm below the wafer surface, why it is referred to as a “shallow 2-DEG”. The closer proximity to the surface is beneficial, since it makes the electrons in the 2-DEG more sensitive to the fields applied to the surface gates and to magnetic field gradients from micro-magnets deposited on the wafer surface, see Section 5.3. Also, the closeness to the depletion gates help in defining small structures in the 2-DEG.

The charge density and mobility of the 2DEG was measured to $\sigma = 7.9 \times 10^{11} \text{ cm}^{-2}$ and $\mu = 1.3 \times 10^5 \text{ cm}^2/\text{V s}$ at 77 K.

3.2.2 GaAs/AlGaAs 2DEG measurement setup

A good part of my stay at the Marcus Lab was spent on learning the ins and outs of high frequency measurements. As part of that I modified a KelvinoxMX-100 dilution to include four high frequency lines and a reflectometry read-out circuit that we unfortunately never got to use in my time there.

Details of this work can be found in Appendix A where the general build-up of the measurement setup is also described. In addition, in relation to most of the measurements described in Chapter 5 are accompanied by a description of the measurement setup/principle.

As described in Section 2.2 a positive bias was applied to the depletion gates when cooling down the sample, to minimize noise caused by electrons tunneling from gates into the 2-DEG [125].

Chapter 4

Comparing gate geometries for modulation of electrostatic barriers in InAs nanowires

We report measurements and analysis of gate-induced electrostatic barriers for electron transport in InAs nanowires. Three types of local gates are analyzed; narrow gates (50–100 nm) located on top of or below the nanowire, and wide gates overlapping the interfaces between nanowire and source and drain electrodes. We find that applying negative potentials to the local gate electrodes induces tunable barriers of up to 0.25 eV. From the temperature dependence of the conductance, the barrier height is extracted and mapped as a function of gate voltage. Top and bottom gates are similar to each other in terms of electrostatic couplings (lever arms ~ 0.1 – 0.2 eV/V) and threshold voltages for barrier induction ($V_g \sim -1$ to -2 V), but low temperature gate sweeps suggest that device stability could be affected by the differences in device processing for the two gate geometries. The results are published in Ref. [151]

4.1 Introduction

Electrostatic gates add local or global control of the potential landscape, and thereby the carrier density, in nanowire devices. Many proposed applications of nanowires in devices such as field effect transistors (FETs)[127, 152, 163, 170], biosensors[171], spin qubits[25, 172] and Cooper pair-splitters[24] rely on changing the state of the nanowire device by the actions of gates.

A number of different gate geometries have been used for nanowire devices; *global back-gates* have been used for FETs[127, 152, 170] and quantum dots (QDs)[24, 150, 154, 173, 174]; *wrap gates* have been used to boost the performance of FETs[18, 163, 175]; *local top gates* have been used for defining single and double quantum dots with independent control of occupation and coupling[152, 173, 176] and for the operation of a Cooper pair splitter[24] and FETs[170]; *local bottom gates* have likewise been used for defining and

controlling single[113] and double QDs[25, 147, 177], successfully reaching the few-electron regime and allowing the operation of a spin-orbit qubit[25]; *contact gates* overlapping the interface between the nanowire and the current carrying leads have been used to control the contact properties of the device independently of the carrier density in the nanowire channel[25, 65, 144].

As the above listing shows, the different gate geometries are not unique in their applications, and choosing one over another for a given objective will among other factors depend on an estimation of gate efficiency and the fabrications challenges involved with a given gate geometry. In particular, for obtaining individual tunability of tunnel barriers and carrier occupation in an InAs nanowire QD a number of local top or bottom gates are both viable choices.

The aim of this study is to measure and compare the effect of local top- and bottom gates on the conductance of InAs nanowires. We present temperature dependent measurements from ~ 250 K to 3 K and quantitatively analyze the barriers induced by the top and bottom gates based on a model of thermally activated transport. Low-temperature measurements, $T \sim 300$ mK, form the basis of a discussion of the influence of device processing on the stability of the top and bottom gated devices. These comparative studies should assist in choosing the better gate geometry for the future design of gated nanowire-based quantum devices.

4.2 Induction of electrostatic barriers by local gates: Top gates vs bottom gates

The devices measured here all consist of InAs nanowires resistively coupled to source and drain electrodes and capacitively coupled to a number of local gate electrodes, see Fig. 4.1. The nanowires are grown by molecular beam epitaxy, have diameters of ~ 80 – 100 nm and stacking fault densities $\sim 30 \mu\text{m}^{-1}$. The InAs nanowires show n-type conduction, likely due to non-intentional doping and pinning of the Fermi level in the conduction band at the surface of the wire[82]. Different fabrication procedures are used for the bottom and top gated devices, see Section 3.1.1, page 35.

Devices were cooled in a cryogen-free ^3He refrigerator and temperature dependence of conductance was measured from room temperature to ~ 3 K, and device stability was measured at ~ 0.3 K. The gates labeled in Fig. 4.1 (a) and (b) were swept sequentially; one gate was swept, typically in the range -3 to 3 V, while the others were kept at positive voltages, typically 2–3 V. Conductance was measured with standard lock-in detection technique at an ac bias of $100 \mu\text{V}$, see Section 3.1.2, page 49.

Fig. 4.2 shows representative measurements of conductance as a function of temperature and gate voltages for the top and bottom gates. Fig. 4.2 (a) shows the effect of top gate, g_5 , on the conductance of the top gated device, *TG1*, as a function of temperature with the gates $V_{g_S, g_D} = 3$ V and $V_{g_{1-4}} = 2$ V. Three regions of different behavior, I-a, II-a

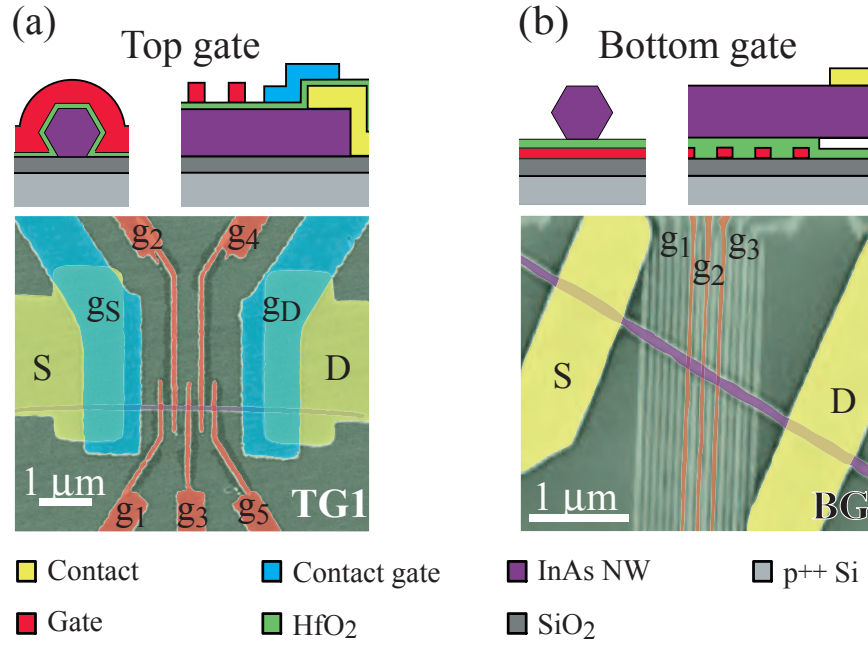


Figure 4.1: Top and bottom gated InAs nanowire devices. (a) SEM micrograph of top gated devices, *TG1*. Current flows through the InAs nanowire in response to a voltage applied between contact leads *S* and *D*. g_S and g_D denote contact gates used to modulate the interface resistance between nanowire and the contacts. Leads g_1 – g_5 are the top gates (width 100 nm, pitch 250 nm) used to induce electrostatic barriers in the nanowire. Top left schematic shows a cross sectional view through one of the top gates. Top right schematic shows a cross sectional view along the axis of the nanowire. (b) SEM micrograph showing the bottom gated device, *BG*. Here, the gates inducing the electrostatic barriers, g_{1-3} , are located below the nanowire (width 45 nm, pitch 75 nm) and there are no contact gates. Top schematics show the corresponding cross sectional views as in (a). For both types of devices, (a) and (b), the barrier gates are isolated from the nanowire by a HfO₂ oxide layer of thickness $\simeq 15$ and $\simeq 20$ nm, respectively.

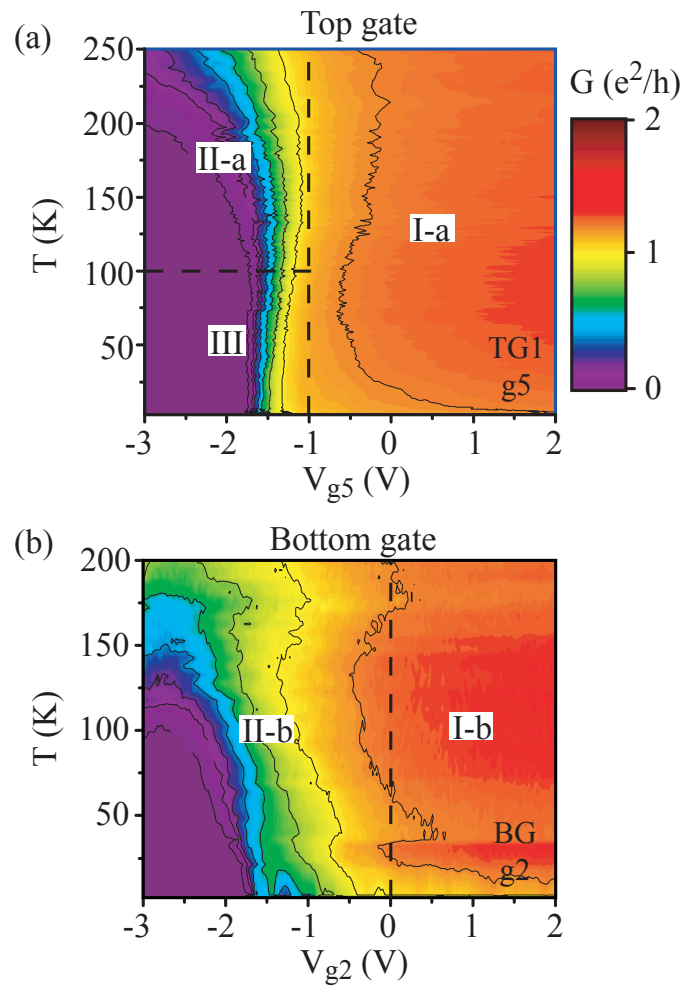


Figure 4.2: Device conductance as a function of temperature and gate voltages. Roman numerals and dashed lines indicate regions with specific trends; regions with similar trends bear the same numeral. (a) Effect of top gate, $g5$, on the conductance of device *TG1* as a function of temperature with $V_{g_{s,gd}} = 3$ V and $V_{g_{1-4}} = 2$ V. (b) Effect of bottom gate $g2$ on conductance of device *BG* as a function of temperature with $V_{g_{1,3}} = 2$ V.

4.2. Trends in temperature dependence of conductance

and III, are separated by dashed lines. In region I-a, $V_{g_5} > -1$ V, the conductance shows very little dependence on gate voltage and no temperature dependence; the conductance has reached a plateau. In region III, $V_{g_5} < -1$ V and $T < 100$ K, conductance is again independent of temperature, but shows a strong decrease with decreasing gate voltage, resulting in a temperature independent pinch-off at $V_{g_5} \approx -1.8$ V. Lastly, region II-a, $V_{g_5} < -1$ V and $T > 100$ K, shows both temperature and gate voltage dependence similar to that seen for the contact gate in region II in Fig. 3.5 (e), see Section 3.1.2, page 49; gate pinch-off voltage decreases from $V_{g_5} \approx -1.8$ V at $T = 100$ K to $V_{g_5} \approx -3$ V at $T = 200$ K. Data for the bottom gate g_2 of device *BG* with gates $V_{g_{1,3}} = 2$ V is shown in Fig. 4.2 (b). The trends are similar to those seen for the top gated device in (a); in region I-b, $V_{g_2} > 0$ V the conductance saturates showing little temperature or gate dependence, corresponding to I-a in (a); in region II-b, $V_{g_2} < 0$ V, temperature dependent pinch-off at negative gate voltages, corresponding to II-a in (a). However, in region II-b the pinch-off is more gradual compared to region II-a in (a) pointing to a weaker capacitive coupling – and the pinch-off voltage is temperature dependent over the entire temperature range, as opposed to region III in (a).

Next, we will discuss the behavior in the different regions and try to explain the observed difference, leading to a quantitative analysis of the regions II-a and II-b.

4.2.1 Interpretation of trends in temperature dependence of conductance as a function of gate voltage

Apart from the differences in sharpness of the pinch-off, the regions II-a and II-b show qualitatively similar gate and temperature dependencies. The pinch-offs at negative gate voltages in II-a and II-b show that barriers are induced only after application of a negative potential to the top and bottom gates, respectively, in contrast to a similar measurement for the source contact gate on the device TG1, see Fig. 3.5 (e), page 51. The increase in conductance with temperature is consistent with thermal activation of carriers over the barriers, and below we analyze these regions to determine the barrier heights using this model.

Comparing the regions I-a, and I-b at the highest gate voltages, the observed temperature independence indicates that transport is not dominated by thermal activation over barriers. The plateaus in conductance in regions I-b and I-c for the top and bottom gates tell that the transport limiting factor is not modulated by the local gates. Most likely the plateaus in I-a and I-b reflect that the conductance, when not limited by barriers, is limited by the interface resistance between wire and contacts. This is consistent with the effect of the contact gate for the top gated device, Fig. 3.5 (e) region I, where conductance rises with gate voltage in a way consistent with lowering contact resistance by increasing the carrier density in the nanowire[178, 179]. Also, the top gate saturation conductance in Fig. 4.2 (a) region I-a coincides with the level in Fig. 3.5 (e) region I at $V_{g_S} = 3$ V, which is the contact gate voltage during the top gate measurement in Fig. 4.2 (a).

Temperature independent conductance for gate voltages where a barrier is induced, is seen

Table 4.1: Device and gate characteristics for local top and bottom gates

Device		TG1		TG2		BG		
Nanowire diameter	nm	$\simeq 90 \pm 10$		$\simeq 100 \pm 10$		$\simeq 80 \pm 10$		
Gate width	nm	100		100		45		
HfO ₂ thickness	nm	$\simeq 15$		$\simeq 15$		$\simeq 20$		
Gate		g3	g5	g3	g5	g1	g2	g3
Lever arm	meV/V	110	240	170	150	150	110	80
Threshold voltage	V	-2.2	-1.4	-1.0	-1.9	-1.6	-1.9	-2.5
Electrochemical potential ^a	meV	250	340	180	280	180	140	140

^a Electrochemical potential is determined by extrapolation of the linear fit for barrier height vs gate voltage to zero voltage.

only for the top gate, cf. region III in Fig. 4.2 (a). The temperature independence would be explained by transport dominated by tunneling through the barrier in this temperature regime. It is surprising that a tunneling dominated region is not observed for the bottom gate in (b); as seen from Tab. 4.1 the bottom gates are half the width of the top gates, which intuitively should increase the significance of tunneling through the barrier in the bottom gated device compared to the top gated. However, the wrap-around geometry of the top gate will likely result in a sharper potential profile for the induced barrier than the flat geometry of the bottom gate, counteracting the effect of the larger physical width of the top gate on the tunneling current. Whether the effect of the physical width of the gate or the effect of the gate geometry will dominate in setting the barrier width and is not clear, and thus neither is it clear which of two gates in Fig. 4.2 (a) and (b) should give the largest contribution from tunneling current. Note that at the lowest temperatures (≈ 3 K) transport is dominated by tunneling through the induced barriers for both top and bottom gates, cf. the low temperature measurements in Fig. 4.6. Having addressed the characteristics of the different regions in Fig. 4.2, we now turn to determining barrier height from a quantitative analysis of the temperature dependent regions II-b and II-c.

4.2.2 Thermal activation over barrier: Extraction of barrier height vs V_g

Transport across barrier: tunneling and thermal activation

A general expression for the conductance, G_b , across a tunnel junction at an arbitrary temperature can be found by summing over the current carrying momentum states, $k_{x,y,z}$. For a three-dimensional conductor carrying a current along the x direction in response to a bias V_{SD} ,

$$G_b = 2e \sum_{k_x > 0, k_y, k_z} (v_{k_x}^+ f(\varepsilon - eV_{SD}) + v_{k_x}^- f(\varepsilon)), \quad (4.1)$$

where e is the electron charge, ε is the energy above the Fermi level, μ , $f(\varepsilon) = \frac{1}{1 + \exp(\varepsilon/k_B T)}$ is the fermi distribution with k_B the Boltzmann constant and T the temperature, $v_{k_x}^\pm = \pm \frac{\hbar k_x}{m^* L_x} \tau(\varepsilon)$ is the drift velocity of the electrons along the x -axis with $m^* = 0.023 m_e$

4.2. Trends in temperature dependence of conductance

the effective mass of the electron, L_x the size of the system along the x -axis and $\tau(\varepsilon)$ the transmission coefficient across the barrier. For a harmonic potential barrier $U(x) = U - \frac{1}{2}m^*\omega^2x^2$, see Fig. 4.3 (a), the transmission coefficient is [180]

$$\tau(\varepsilon) = \frac{1}{1 + \exp(\frac{U-\varepsilon}{T_0})}, \quad T_0 = \frac{\hbar\omega}{4\pi^2}, \quad (4.2)$$

and Eq. 4.1 can be reduced to

$$G_b = \frac{e^2}{h} \frac{Am^*e}{\hbar^2\pi^2} \int_{-\mu}^{\infty} d\varepsilon \int_0^{\pi} d\theta \int_{-\pi/2}^{\pi/2} d\phi \frac{1}{(\varepsilon + \mu) \sin(\theta)^2 \cos(\phi) \frac{-\partial f(\varepsilon)}{\partial \varepsilon} \left(\frac{1}{1 + \exp\left(\frac{U - ((\varepsilon + \mu) \sin(\theta)^2 \cos(\phi) - \mu)}{T_0}\right)} \right)}, \quad (4.3)$$

with $\frac{-\partial f(\varepsilon)}{\partial \varepsilon} = \frac{1}{4T \cosh^2(\varepsilon/2T)}$ the derivative of the Fermi distribution and A the cross sectional area of the transport channel. Here T_0 is a ‘‘tunneling temperature’’ determined by the curvature, ω , of the barrier; for a given height of the barrier, U , an increased curvature will lead to a thinner barrier increasing the tunneling probability, which is described by the an increasing T_0 .

As eq. (4.3) is a rather long expression to work with, and since we do not know the electrochemical potential, μ , we would like to simplify the expression used to fit to the data by making some simplifying assumptions.

For high barriers ($U \gg T$) and temperatures exceeding T_0 an alternative expression for the conductance can be obtained, still allowing the determination of T_0 , and circumventing the issues with the unknown μ [180],

$$G_b = \frac{e^2}{h} \frac{Am^*e}{\hbar^2\pi^2} \frac{\pi T_0/T}{\sin(\pi T_0/T)} \exp(-U/T), \quad U \gg T > T_0. \quad (4.4)$$

In Fig. 4.3 (b.1-4) we compare the two expressions eq. (4.3) and eq. (4.4) for different values of U and T_0 . For validation of the models, we also plot the simple Arrhenius expressions for thermally activated transport [16] $G \propto T \exp(-U/k_B T)$ (valid for $U \gg T$ and $\tau(\varepsilon_x > U) = 1$, $\tau(\varepsilon_x < U) = 0$) and the expression for transport without tunneling $G \propto -U + k_B T \ln(1 + \exp[-U/k_B T])$ (valid for $\tau(\varepsilon_x > U) = 1$, $\tau(\varepsilon_x < U) = 0$), both obtained from eq. (4.1) in the given limits. Fig. 4.3 (b.2) shows that all four models agree in the temperature range 1-280 K for $U = 150$ meV and $T_0 = 1$ meV as tunneling can be neglected and only electrons with energies higher than the barrier contributes to the current (*i.e.* thermally activated transport dominates). Increasing T_0 to 10 meV while keeping $U = 150$ meV (effectively making the barrier thinner) shows that tunneling now contributes to the current, see Fig. 4.3 (b.4), and that eq. (4.4) shows agreement with the exact numerical integral eq. (4.3). In contrast the the expressions disregarding tunneling predict a lower conductance. Thus, tunneling can be important ‘‘irrespective’’ of U if T_0 is high, corresponding a thin barrier with a high curvature.

From Fig. 4.3 (b.1-4) we also see that eq. (4.4) is exact for high U , as the discontinuity at

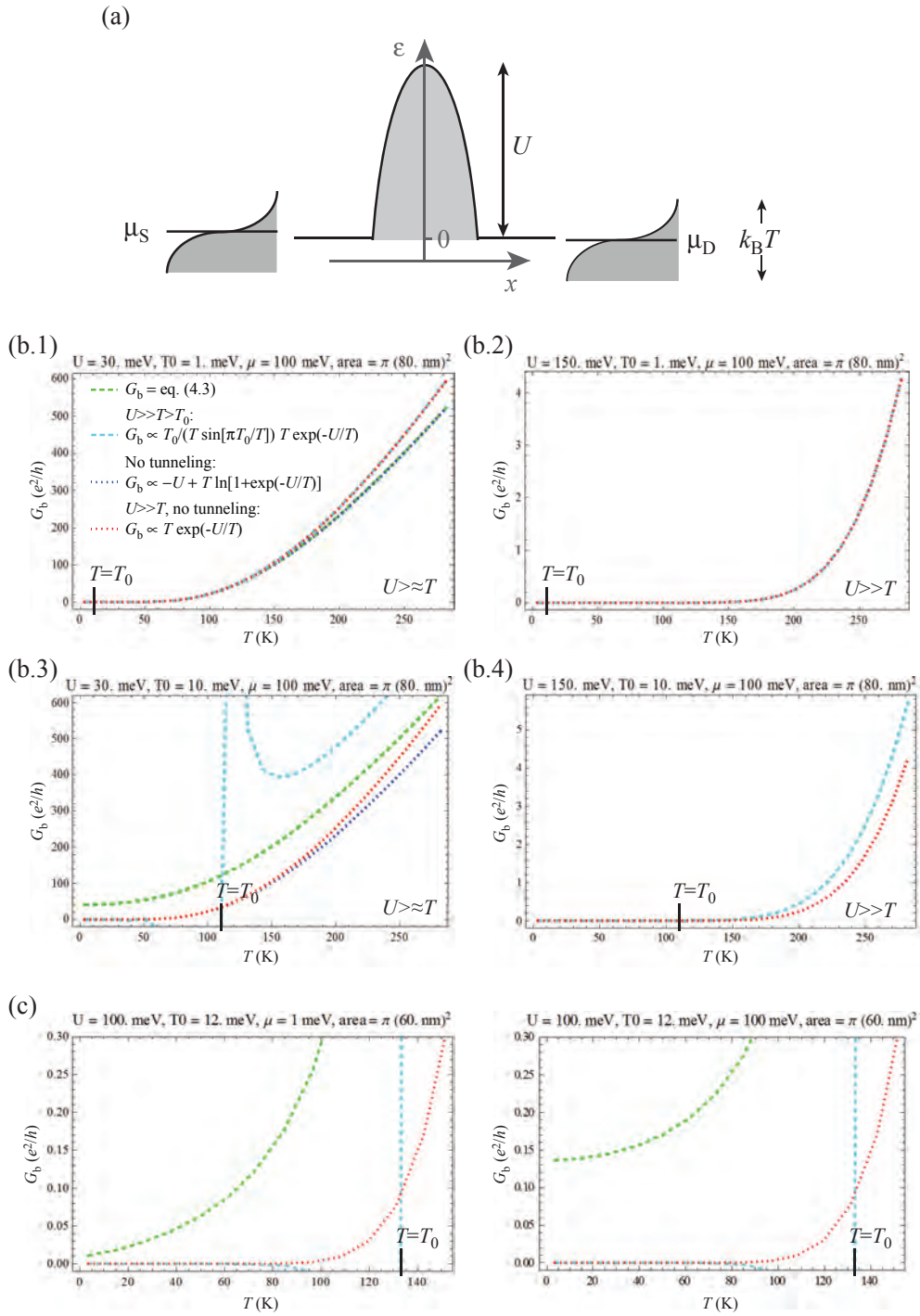


Figure 4.3: Transport across barrier in nanowire and models for different regimes. (a) Schematic representation of the gate induced barrier of height U above the fermi energy. The wire sits between the source and drain reservoirs with electrochemical potentials $\mu_{S,D}$ both broadened by the thermal energy $k_B T$. (b.1-4) Plots of conductance across a barrier for four models with different assumptions and for different values of barrier height U , barrier curvature T_0 , but identical electrochemical potential μ and cross-sectional area. Note that the dotted lines and the dashed lines overlap pairwise in (b.4). (c) Comparison of same expressions as in (b) for different values of μ . Note that the red and dark blue dotted curves overlap in both plots.

4.2. Trends in temperature dependence of conductance

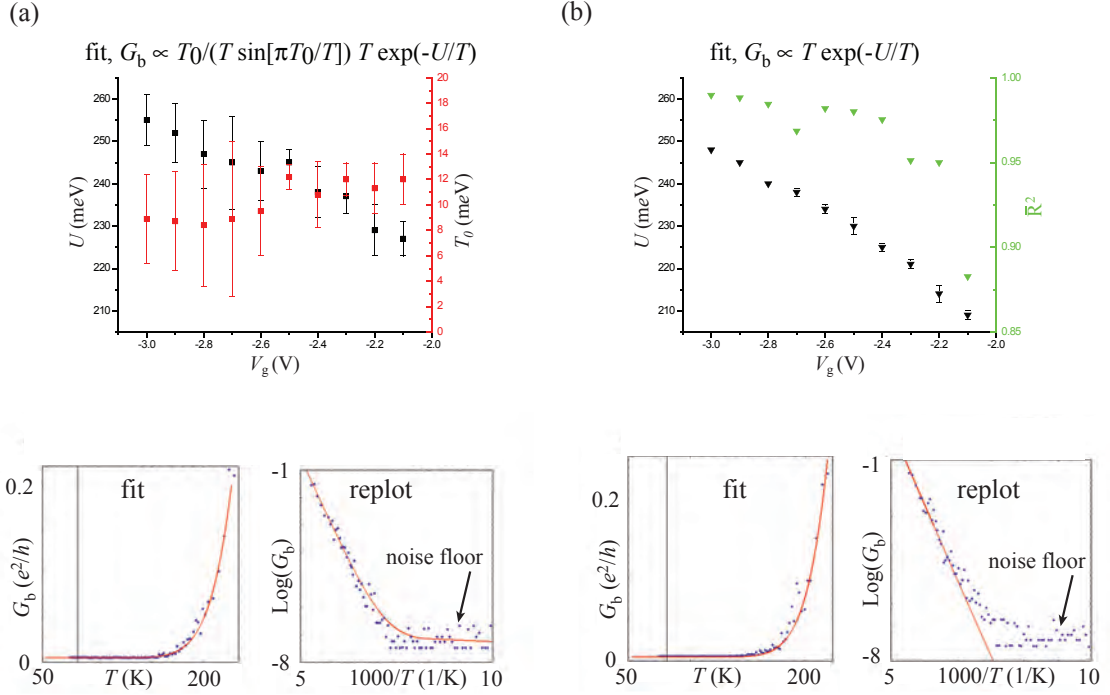


Figure 4.4: Extraction of data from fits for model incorporating the barrier curvature, T_0 , [180] and simple arrhenius-type model [16]. (a) Results from fitting Eq. 4.4 to data and below, examples of fit to data and replot of fit and data on log scale. (b) Results from fitting Eq. 4.5 to data including the goodness of fit parameter \bar{R}^2 . Examples of fit and replot on log scale shown below.

$T > T_0$ will not affect fitting when $G(T_0) \approx 0$. However, for $G(T_0) > 0$ the discontinuity at $T > T_0$ will make fitting in this temperature region impossible, *cf.* Fig. 4.3 (b.3).

For the full expression, eq. (4.3), we see that knowledge of the electrochemical potential is needed, as it affects the tunneling dominated part of the curve, *cf.* Fig. 4.3 (c). Using the chemical potential as a fitting parameter gives an undetermined T_0 .

Instead we try fitting our data with the more simplified expression eq. (4.4) restricted to the parameter space $U \gg T > T_0$. However, this parameter space turns out to be a very limited interval, since we, see Fig. 4.4 (a), either get an undetermined T_0 for the highest U or quickly get into a regime where $T \approx T_0$ is in the fitting interval, causing the discontinuity to make the fit invalid.

If we instead perform the fit using the simplest model for thermally activated transport and restrict the fitting to $U \gg T$, see Fig. 4.4 (b), we find approximately the same values for U , but we do of course not get any information for the tunneling barrier.

Barrier height vs V_g from thermal activation analysis

To characterize the induced barriers we model the transport in the regions II-b and II-c as thermal activation of electrons over the barriers, and neglect quantum tunneling through the barriers. Assuming three dimensional diffusive transport of the electrons in the temperature range $\sim 250 - 10$ K for the given NW diameters (~ 100 nm) [149] and

expected electron mean free path (~ 50 nm) [112, 162, 181], the zero-bias conductance, G , across a single barrier as a function of temperature, T , follows [182],¹

$$G(T) = C \cdot T \cdot \exp\left(\frac{-E_b}{k_B T}\right). \quad (4.5)$$

Here, E_b is the height of the barrier above the electrochemical potential, C is a constant related to the carrier density and mobility and k_B is the Boltzmann constant. Thus, when thermally activated transport is dominant an Arrhenius-type plot of $\ln G/T$ vs $1/T$ yields a straight line where E_b can be extracted from the slope.

However, Eq. (4.5) does not account for possible temperature dependence of the carrier mobility and density or the contact resistance between nanowire and source/drain electrodes. Therefore, to apply Eq. (4.5) to our data we normalize the temperature dependence of the conductance, and subtract the contact resistance from the normalized data. The temperature dependence of the conductance, $G(V_g, T)$, is normalized with respect to the saturation conductance, $G(2V, T)$, as

$$G_n(V_g, T) = \frac{\max_T(G(2V, T))}{G(2V, T)} \cdot G(V_g, T),$$

where $\max_T(\dots)$ denotes the maximum value as a function of T . This eliminates the temperature dependence of carrier density and mobility. Since the temperature dependence at the highest gate voltages is very weak, *cf.* regions I-a and I-b in Fig. 4.2, the normalization constant $\frac{\max_T(G(2V, T))}{G(2V, T)}$ is mostly close to 1. Interpreting the plateaus in regions I-a and I-b as conductance dominated by contact resistance, we estimate the contact resistance as $R_c(T) = 1/G_n(2V, T)$ and eliminate it from the normalized data by subtraction, yielding

$$G_{n,R_c}(V_g, T) = \left((G_n(V_g, T))^{-1} - R_c(T) \right)^{-1}.$$

Left and rightmost panels of Fig. 4.5 (a) show fits of Eq. 4.5 to $G_{n,R_c}(V_g, T)$ for series of gate voltages for top and bottom gates, respectively; fits are restricted to data ranges of approximately linear dependence, and the intersection with the y-axis is allowed to vary with gate voltages. Only data with a negative slope is fitted since these are the traces where the barrier dominates transport, *cf.* the different regions in Fig. 4.2. The noise floor in the measurements is visible in the data for the most negative gate voltages, where the linear decrease of $\ln G/T$ vs $1/T$ is interrupted as the conductance drops below $\sim 0.007 e^2/h$. From the slopes of the linear segments the barrier heights, E_b , were extracted for different gate voltages and devices, and the results are summarized in Fig. 4.5 (b). The left panel shows the results for the top gates and the right shows the bottom gates. The increase in barrier height with negative voltage is different for the individual gates, even on the same device. This reflects differences in the capacitive coupling to the nanowire for the individual gates despite their intended identical geometry and size, *cf.* top schematics Fig.

¹The linear T term comes from the dimensionality of the electron transport in the nanowire. For one dimensional transport this term is absent.

4.2. Trends in temperature dependence of conductance

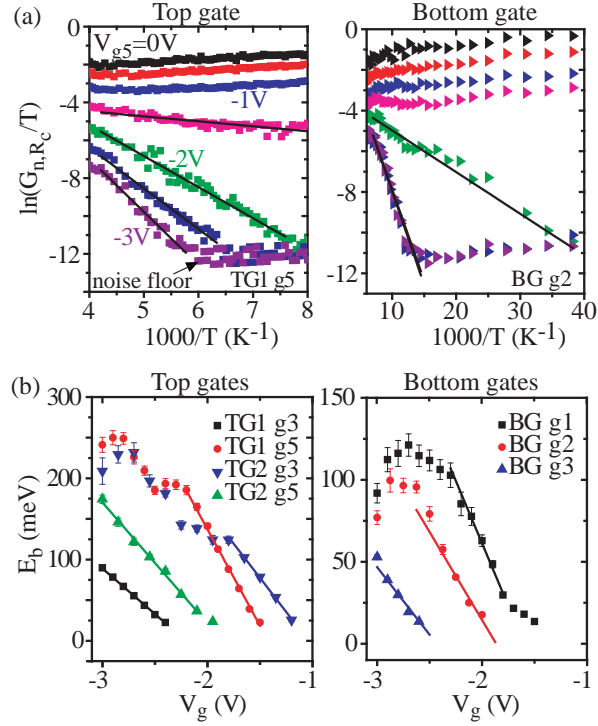


Figure 4.5: Extraction of gate induced barrier height above the electrochemical potential, E_b , assuming thermally activated transport. (a) Left, logarithm of G/T vs $1/T$ for various V_{g_5} for top gated device TG1. Solid lines are linear fits, the slope yielding the barrier height, E_b . Right, same for bottom gate g_2 on the device BG, the different traces corresponding to the same gate voltages as on the left. (b) Left, extracted E_b as a function of gate voltage, V_g , for four top gates on the devices, TG1 and TG2. Solid lines are linear fits giving the electrostatic coupling of the gate to the wire. Right, same for three bottom gates on the device BG.

4.1. The electrostatic coupling strength – or lever arm – between gate and nanowire can be found as the slope of a linear fit to E_b vs V_g , solid lines Fig. 4.5 (b). The fits are restricted to ranges without plateaus, representing gate switches or effects other than the simple action of the gate on the barrier height. The extracted couplings for the top and bottom gates are gathered in Tab. 4.1 together with other characteristics for both types of gates. On average, the lever arms for the top gates are slightly larger than for the bottom gates², which is in line with the greater gate width and thinner ALD oxide for the top gates.

For both top and bottom gates, barrier growth with increasingly negative voltage only occurs below a certain threshold voltage, different for the individual gates. The threshold voltage represents the voltage at which the induced barrier is aligned with the electrochemical potential in the nanowire, thus starting to block the current. Assuming a V_g independent lever arm, the y-axis intersection of the linear fit to E_b vs V_g will give the electrochemical potential, for barriers setting out from the bottom of the conduction band³. Tab. 4.1 shows that the extracted values of electrochemical potential seem to differ for the two devices; the top gated devices average to a magnitude ~ 260 meV, and the bottom gated indicate ~ 150 meV. Both show a tendency that a larger gate lever arm leads to less negative threshold voltage, *cf.* Fig. 4.5 (b).

4.3 Influence of local gate geometry on low temperature device stability

The analysis of the gate induced barriers indicates that the top and bottom gates are very similar and equally useful for inducing barriers, *e.g.* in order to define quantum dots at low temperature. However, performing low temperature measurements with gates configured to define quantum dots shows another important aspect. Figure 4.6 contrasts similar measurements for the bottom gated device BG, (a)–(c), and top gated devices TG1 and TG3, (d)–(e), showing that the measurements on the top gated devices suffer from a high degree of charge noise. Fig. 4.6 (d) shows a measurement of Coulomb oscillations in top gated device TG3 tuned to form a single QD, exhibiting Coulomb oscillations in I vs V_{g1} with random shifts in peak positions for changing V_{g3} . Panel (e) shows Coulomb blocked regions for top gated device, TG1 tuned to form a single QD, in a measurement of conductance as a function of gate voltage, V_{g2} , and bias voltage, V_{SD} . The plot shows a

²The four top gate lever arms, α_{TG} , have mean value $\bar{\alpha}_{TG} = 0.17$ eV/V and $\sigma_{\bar{\alpha}_{TG}} = 0.03$ eV/V. For the three bottom gates the same values are $\bar{\alpha}_{BG} = 0.11$ eV/V and $\sigma_{\bar{\alpha}_{TG}} = 0.02$ eV/V

³This argument disregards the effect of the global back-gates in the devices. For the top gated devices TG1 and TG2, the back-gates were so weakly coupled ($\Delta G < 0.3 e^2/h$ for $V_g \pm 10$ V) that we disregard their effect for the 1 and 3 V applied to the them, respectively. For the back-gate on bottom gated device BG, analysis like that presented in Fig. 4.5 yields a lever arm of 30 meV/V, threshold voltage -4.7 V and electrochemical potential 140 meV. The electrochemical potentials for the bottom gates are adjusted for a back-gate voltage of 2 V by subtraction of 60 meV from the value extracted by the analysis in Fig. 4.5.

4.3. Gate geometry and low temperature stability

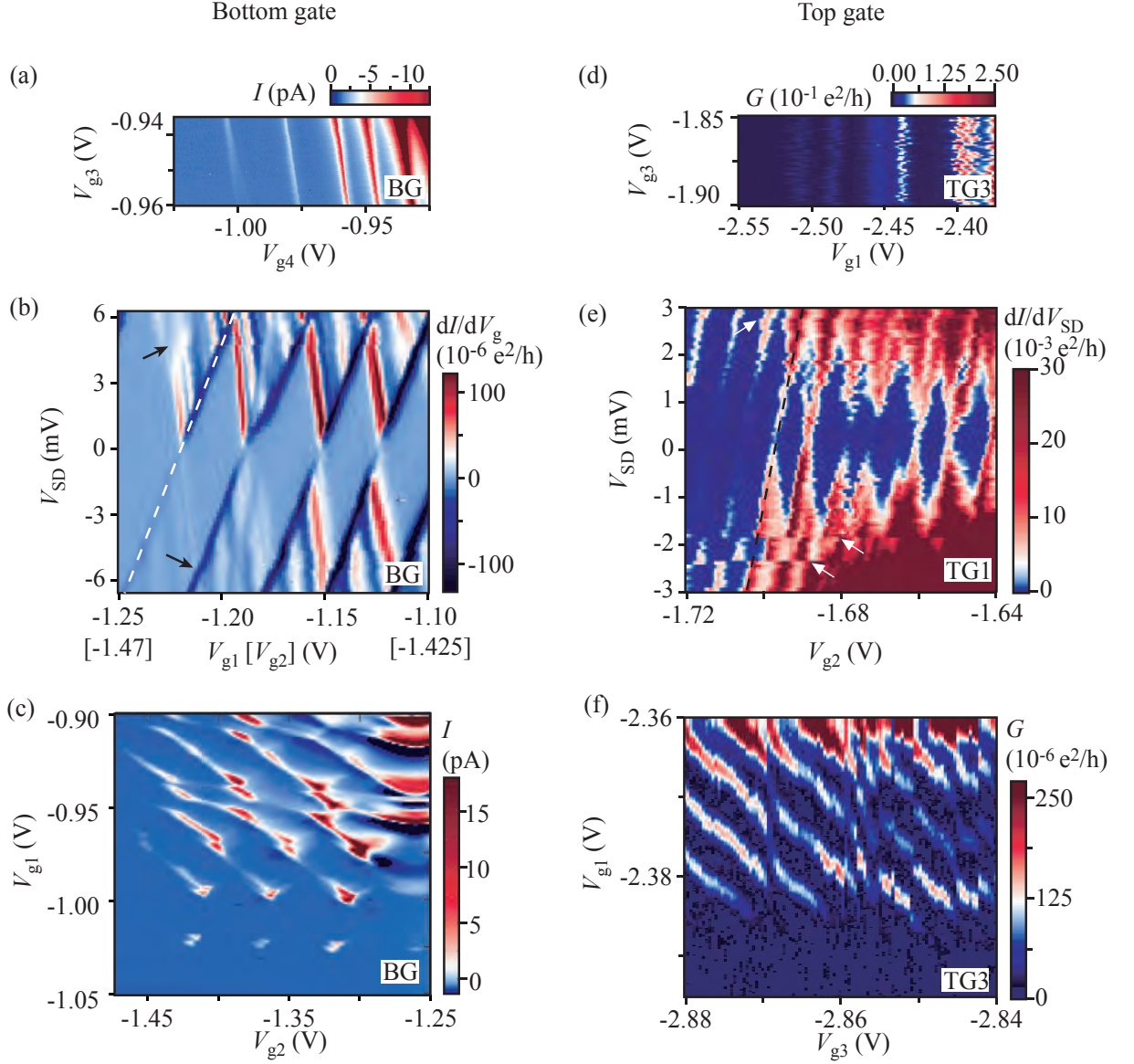


Figure 4.6: Comparison of sweep-stability of top and bottom gates at $T \approx 0.3$ K. (a) Coulomb blockade measurement for bottom gated device BG tuned to a single QD showing I vs V_{g4} vs V_{g3} exhibiting Coulomb peaks in I vs V_{g4} being shifted smoothly by the action of V_{g3} . (b) Bias spectroscopy of top gated device TG1 showing Coulomb blockade regions in measured transconductance when sweeping gate voltage $V_{g_{1,2}}$ and stepping bias voltage, V_{SD} . For the remaining gates $V_{g3} = -1.65$ V, $V_{g_{4,5}} = 2$ V and $V_{g_{SD}} = 3$ V. Switches are marked by arrows, dashed line traces edge of Coulomb blockade region. (c) Bottom gate device BG tuned to form a double QD showing I vs V_{g1} vs V_{g2} . (d) Coulomb blockade measurement for top gated device TG3 tuned to form a single QD, exhibiting Coulomb oscillations in I vs V_{g1} with random shifts for changing V_{g3} . (e) Bias spectroscopy of bottom gates device, BG, when sweeping the bottom gates g_1 and g_2 with the global back-gate $V_{bkg} = -1.62$ V and remaining gates grounded. (f) Top gate device TG3 tuned to form a double QD showing G vs V_{g1} vs V_{g3} .

high number of switches between individual sweeps of gate voltage, visible as jagged and discontinued lines of conductance changes that distort the usual diamond shaped Coulomb blockaded regions, see arrows and dashed line. Panel (f) shows similar switching noise in a measurement of G vs V_{g1} vs V_{g3} for top gated device TG3 tuned towards forming a double QD. Such switches occur when the electrostatic environment changes abruptly, e.g. by the shifting of a charge trapped in the oxide layer, rather than smoothly by the action of the gate itself [124, 125]. Similar results were obtained for the other top gated devices. Fig. 4.6 (a)–(c) show similar measurements for the bottom gated device BG. Comparing to the measurements in (d)–(f), the features form continuous lines as a function of gate voltages, see dashed line in (b), indicating that the actions of the bottom gates are not disturbed by fluctuations in the environment. A statistical analysis of the charge fluctuations for additional samples would be needed to substantiate the difference in device stability suggested by the measurements in Fig. 4.6, and to conclude that the bottom gate geometry is superior with respect to charge noise.

A difference in device stability could be caused by the different order of the processing steps in device fabrication — deposition of nanowires is the second to last step for bottom gates, whereas it is the first step for top gates. This means the nanowires are exposed to more, potentially contaminating, processing steps for the top gated devices; *poly(methyl methacrylate)* (PMMA) residues from e-beam lithography can act as charge traps; *e-beam irradiation* can cause charge accumulation in the nanowire- and ALD oxide due to secondary electrons escaping from the oxides [183] and the irradiation can damage the oxides, creating charge traps close to the nanowire that cause charge noise by trapping electrons leaking from the top gates into the nanowire [125]. Also, the growth of the ALD oxide directly on top of the nanowire may degrade device stability for the top gated devices, since enhanced defect densities are expected at growth interfaces compared to internally in films [184].

In addition to the processing step order, the top and bottom gated devices differ in having nanowires from different growths and HfO₂ of thicknesses 15 nm and 20 nm deposited at 130 °C and 90 °C, respectively. However, from transmission electron microscopy the nanowires are known to be of equal quality, i.e. stacking fault density *etc.*; likewise, the oxide film quality, i.e. crystallinity and interface trap density, is not expected to change significantly with the mentioned differences in growth temperatures [184, 185]⁴ and thicknesses [186].

Thus, we believe that the most likely cause of the suggested difference in stability of top and bottom gated devices would be the exposure of the nanowire to all processing steps for the top gated device.

⁴Both deposition temperatures, 90 °C and 130 °C, are considered low with respect to film crystallinity; films deposited at 130 °C are ~ 92–98 % amorphous, and for 90 °C > 98 % amorphous [185].

Chapter 5

Confined electron spins in GaAs/AlGaAs heterostructure 2-DEG QDs

5.1 Preface

The work contained in this chapter was performed over a total of seven months comprising two stays at the Marcus Lab headed by prof. Charles Marcus at the Department of Physics at Harvard University. The work was performed in collaboration with and under the guidance of postdoctoral fellow Dr. Javad Shabani. Both the addition of high frequency lines and read-out to the fridge, see Section A.1.2, page 97, as well as establishing the measurement setup, see Section 3.2.2, page 53, and performing the measurements presented here were combined efforts by the author and Javad Shabani. However, the idea for and the fabrication of the ferromagnetic gate device were Javad Shabani's efforts. Also, the EDSR measurements were performed by Javad Shabani in the week following the author's departure from the Marcus Lab.

5.2 Introduction

The focus of the work presented in this chapter is manipulation of electron spins confined to quantum dots in GaAs/AlGaAs heterostructure 2-DEGs towards the end of the utilizing the electrons in spin qubits [28].

Two ideas were the basis for the experiments performed, namely

- Incorporating ferromagnetic metal in the depletion gates to make them double as micro-magnets supplying magnetic field gradients allowing spin qubit operation [131]. This avoids issues with alignment between micro-magnet and quantum dots and allows closer proximity of the magnet to the 2-DEG, improving the magnetic field gradients obtained.

- Utilizing single unpaired electron spins in multi-electron quantum dots for spin qubits. Avoiding the single electron regime would relax demand for optimal geometry, tuning and purity of the device and the additional electrons should have beneficial screening effects on qubit coherence [187].

In the following we will demonstrate control of charge occupation to the last electron for double quantum dots in a double–double quantum dot device with ferromagnetic gates and use electric dipole spin resonance (EDSR) measurements to determine the difference, ΔB_Z , in the local magnetic field parallel to the externally applied field between QD positions for one set of double dots. In the multi-electron double dot occupation regime we will address spin filling behavior and demonstrate spin blockade. Assuming an analogy between the two-electron and the multi-electron spin states we will extract the exchange energy, J , and estimate the spin decoherence timescale, T_2^* , from pulsed gate measurements. All measurements, two- and multi-electron, are performed on the same device.

5.3 Two-electron double quantum dots and magnetic field gradients with ferromagnetic gates

5.3.1 Magnetic field gradients from magnetic gate structure

For lateral DQDs in heterostructure devices, micro-magnets giving magnetic field gradients allowing spin manipulation are usually incorporated by deposition of a ferromagnetic metal, *e.g.* Co or Ni, on top of a dielectric layer insulating the magnetic metal from the normal metal depletion gates [102, 120, 131, 134], see Fig. 5.1 (a). The geometry and orientation of the micro-magnet is designed to optimize specific gradients of certain components of the magnetic field along a given axis, according to the intended operation basis of the qubit; for EDSR mediated spin rotations, see Section 2.5.1, page 30, these are the gradients of the components perpendicular to the total field, corresponding to $\partial B^{x,z}/\partial x$ and $\partial B^{x,z}/\partial y$ in Fig. 5.1 for the axes orientation shown and a total field, B , dominated by an externally applied field, B_0 , along the y -axis; for operations in the S - T_0 basis, see Section 2.5.2, page 32, it is the difference in the total (average) field between the quantum dots, $\mathbf{B}_{\text{QD1}} - \mathbf{B}_{\text{QD2}} = \Delta \mathbf{B}_Z \approx \Delta B^y \hat{\mathbf{y}}$ in Fig. 5.1, for the same conditions as above. However, the gradients achieved are sensitive to misalignment of the micro-magnet with respect to the depletion gates defining the QD positions, as the micro-magnet is defined in a separate lithography step. Also, the need for an insulating layer between the depletion gates and the micro-magnet increases the distance to the 2-DEG below the wafer surface, which leads to a weak field, and hence gradient, from the micro-magnet at the level of the QDs. The deposition of the insulating layer itself may also lead to increased charge noise, due to defects and interface charge traps present in the insulating layer depending on the material and deposition conditions [184, 185], see discussion in Section 4.3, page 66.

Fig. 5.1 (b) shows a GaAs/AlGaAs heterostructure device with ferromagnetic gates of Co sandwiched between a Ti sticking layer and an Au capping layer and a 2-DEG 57 nm below

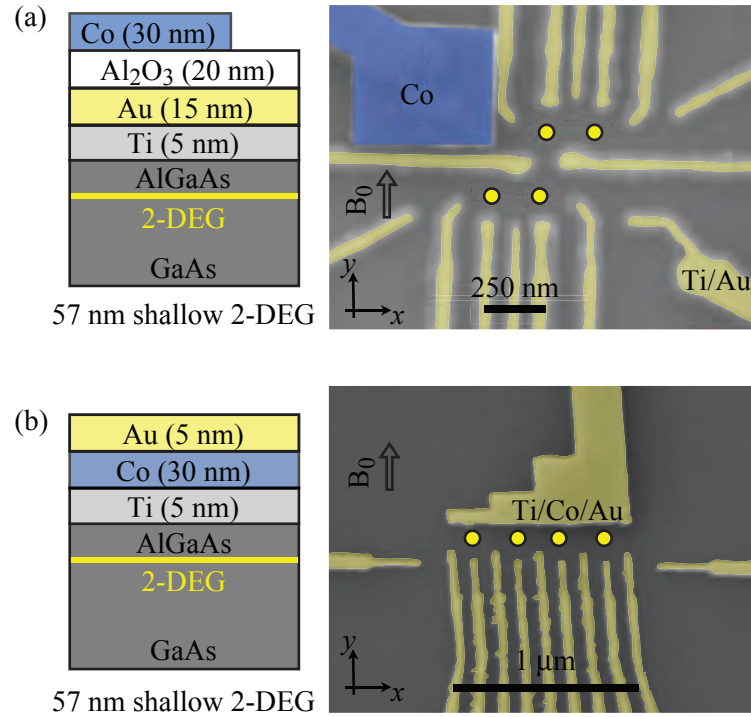


Figure 5.1: Two different methods for incorporating micro-magnets for field gradients between quantum dots in a 2-DEG 57 nm below the GaAs/AlGaAs wafer surface. (a) “Old” design, where magnet, Co, is deposited in a final processing step, after insulating it from the depletion gates (Ti/Au) using e.g. Al₂O₃. The left panel shows schematic cross-section through the structure, right panel shows a false color SEM micrograph of a finished device, where yellow dots indicate the position of the QDs and B_0 is an applied magnetic field with the indicated orientation. (b) “New” design, where the depletion gates incorporate the magnetic Co, sandwiched between a Ti sticking layer and an Au capping layer. Left and right panel show the equivalents to (a)

the wafer surface (left). The ferromagnetic depletion gates should help to form quantum dots in the 2-DEG at the positions marked by yellow dots (right). The advantages of incorporating the magnet in the gates are, as mentioned, avoiding both alignment issues and deposition of an insulating dielectric, giving improved magnetic field gradients and possibly lowering charge noise. One disadvantage is, however, constraints on the gating geometry, since it should be designed to give both the desired magnetic field gradients and tunability of dots and their couplings; these can be optimized independently for the floating micro-magnet design. For the devices in Fig. 5.1, the result of the constraints can be seen from SEM micrographs in the rightmost panels of (a) and (b); in the current realization of the ferromagnetic gates, the double-double quantum dots are in a linear configuration, making some aspects of the device tuning more difficult compared to the offset double-double dot configuration for the floating magnet device of Fig. 5.1 (a). Another disadvantage is the limitation on the thickness of the ferromagnetic gates, as the need for fine structured gates sets a limit on the gate height allowing for lithographic definition and successful lift-off. Generally, a thicker ferromagnetic layer will give larger fields and gradients and is thus desirable [134].

In designing the ferromagnetic gate device in Fig. 5.1 (b), the pitch of the finger gates, defining the positions of the QDs, is adopted from the “old” device in Fig. 5.1 (a); the QD pitch is ~ 250 nm and we would expect similar depletion behavior for the two devices. The magnetic field from the gates at the positions of the dots will be dominated by the big top gate and hence determine the achieved gradients between the dots. Simulations show that a design as that in Fig. 5.1 (b), with a y -axis extension stepped with QD positions, gives good gradients combined with a relatively simple geometrical shape easily produced with standard e-beam lithography. COMSOL Multiphysics is used to simulate the magnetic field produced by the ferromagnetic gate structure with a stack-up and geometry as shown in Fig. 5.1 (b) and a remnant field of 1.8 T parallel to the y -axis, the direction of the applied field, B_0 , in the experiments, see Fig. 5.2 (a). The magnitude of the remnant field is not meant to represent the exact conditions in experiments, and the obtained values of field and gradients should not be regarded as the exact values we expect to achieve in experiments. Rather, we are interested in the profile of the field at the level of the dots; the relative sizes of the field components and the gradients of these between the dots should give an indication of which modes of operation might be successful. Fig. 5.2 (b)–(i) show plots extracted from the simulation, and (a) shows a SEM micrograph of device with magnetic gates; the black dotted line indicates the position of field profiles along the x -axis, *cf.* (f), with $x = 0$ at the middle finger gate; the green dashed lines indicate field profiles along the y -axis at the position of the dots, *cf.* (g)–(i), with $y = 0$ along the black dotted line. As indicated in (a), the x -axis is parallel to the $[\bar{1}\bar{1}0]$ crystal axis and the y -axis is parallel to the $[110]$ crystal axis. Fig 5.2 (b)–(e) show $|\mathbf{B}|$, B^x , B^y and B^z , respectively, in the xy -plane at the level of the 2DEG with the outline of the gate structure superimposed. Again, the black dotted line indicates the axis of the line cuts in panel (f). From the plane

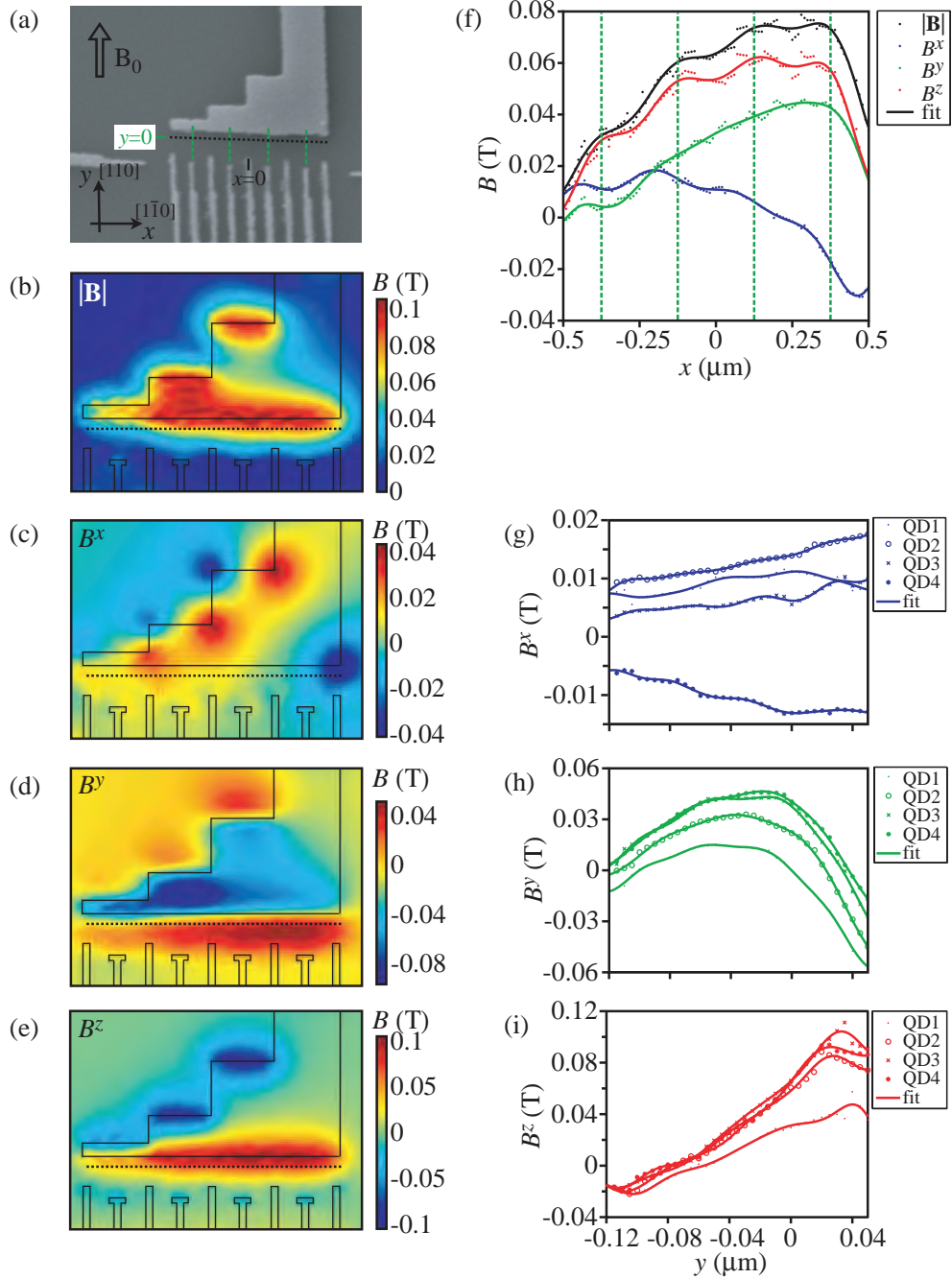


Figure 5.2: COMSOL Simulation of micro-magnet magnetic field and line cuts at the positions of the four quantum dots for magnetization $M = 1.8\text{T}/\mu_0$ along the y -axis. (a) SEM micrograph of device with magnetic gates on a 57 nm shallow 2-DEG GaAs/AlGaAs wafer. The indicated x and y -axes run along the $[1\bar{1}0]$ and the $[110]$ crystal axis, respectively. B_0 is the externally applied magnetic field magnetizing the micro-magnet; the black dotted line indicates the position of field profiles along the x -axis, *cf.* (f); and the green dashed lines indicate field profiles along the y -axis, *cf.* (g)-(i). Zero of the x -axis is at the middle finger gate and zero of the y -axis is along the black dotted line. (b)-(e) Simulations of micro-magnet magnetic field $|B|$, B^x , B^y and B^z , respectively, in the xy -plane at the level of the 2DEG. (f) x -axis line cut at $y = 0$ showing $|B|$ (black), B^x (blue), B^y (green) and B^z (red). Green dashed lines mark intended positions of dots. (g)-(i) y -axis line cuts showing B^x , B^y and B^z at the plane of the 2-DEG around the expected y equilibrium position for each of the four quantum dots labeled QD1-4 from left to right.

cuts it can be seen that the total field is dominated by the B^y and B^z components, and especially so along the flat bottom edge of the big top gate where the dots are positioned, cf. x -axis line cuts in panel (f). B^x has its extrema at the corners of the stepped top gate, but these are away from the dot positions and generally weaker than the extrema in B^y and B^z ; the x -axis line cuts in panel (f) clearly show that the magnitude of B^x is generally a factor of 2 or 3 smaller than B^y and/or B^z at the positions of the dots, marked by the green dashed lines. B^y shows a maximum along the y -axis between the plunger gates ($y = -0.12 \mu\text{m}$) and the top gate edge ($y = 0.04 \mu\text{m}$), and the maximum increases with the x -coordinate up until between the third and fourth dot. Note that B^y is different for the different dot positions, see Fig. 5.2 (f), giving rise to the ΔB_Z term needed for S - T_0 qubit operation [97] and allowing quantum dot addressability for rotations in the EDSR scheme [131]. Rotations in the EDSR scheme should also be possible by exploiting the stable gradient in B^z along the y -axis centered around $y \approx -0.03 \mu\text{m}$, cf. Fig. 5.2 (i). The B^x gradient along the y -axis is about a factor of ten lower, cf. Fig. 5.2 (g), and is thus not expected to be of significance. It should also be beneficial for the stability of the EDSR resonance frequency that B^y only changes slowly with y around $y = -0.03 \mu\text{m}$ at the dot positions, cf. Fig. 5.2 (h).

5.3.2 Formation of few-electron double dots and spin blockade

The simulations above indicate that the magnetic field gradients should allow for spin rotation both in the EDSR scheme and the S - T_0 basis. Before attempting any of this, we first need to establish that the new gate geometry forms the dots as expected and that we can control the occupation on the dots down to the last electron. Fig. 5.3 (a) shows a false color micrograph of a device similar to the measured. The intended positions of the QDs are indicated by yellow dots and the QPCs used for determining occupancy of the QDs are marked by yellow arrows. All gates can be applied dc voltages and additionally the plunger gates, V_{Ll} , V_{Lr} , V_{Rl} and V_{Rr} , that control the potentials on the dots have high frequency capabilities as indicated in Fig. 5.3 (a). Ohmic contacts to the 2-DEG are indicated by crossed squares, and are used for charge sensing measurements of DQD occupation by measuring the time averaged conductance through the QPCs [188]. As indicated by circuit diagrams in Fig. 5.3 (a) the QPC is also part of a tank circuit, enabling fast read-out of the DQD charge state in a reflectometry measurement [189], see section A.2. Applying negative dc voltages to the gates and measuring the derivatives of the QPC conductances vs the voltages on plunger gates for both pairs of DQDs gives the charge stability diagrams shown in Fig. 5.3 (b) and (c). The number of electrons on left, m , and right QD, n , in a DQD pair is indicated as (m, n) and both the left DQD pair, (b), and the right DQD pair, (c), show control of the occupation down to the last electron with the voltages on the relevant plunger gates. In the few-electron regime Pauli spin blockades (PSB) are expected at the $(1, 1)$ - $(2, 0)$ and $(1, 1)$ - $(0, 2)$ transitions assuming simple even-odd spin filling [96], and this is also observed for the right DQD; Fig. 5.4 shows transport and pulsed measurements of the $(1, 1)$ - $(0, 2)$ charge transition indicating Pauli spin blockade — measurements for the

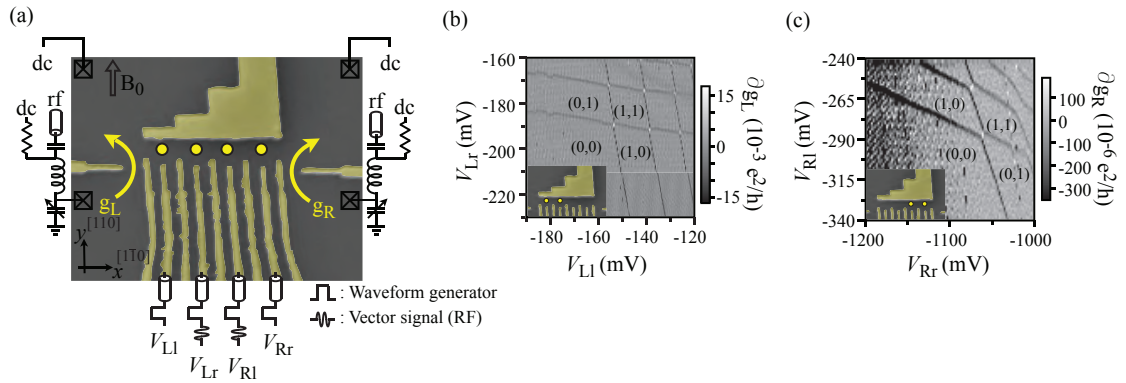


Figure 5.3: Measurement configuration and depletion of double quantum dots. (a) Micrograph of device identical to the measured, with ohmic contacts indicated by crossed squares and circuit diagrams for the tank circuits connected to the QPCs used for charge sensing. The plunger gates V_{Ll} , V_{Lr} , V_{Rl} and V_{Rr} control the potentials on the dots and are all connected through high frequency coaxial cable to waveform generators (Tektronix AWG520) and two are additionally connected to vector signal generators (Rhode&Schwarz SMBV100A). The charge sensor quantum point contacts are in the following measurements only used for standard lock-in measurement of the time average conductance of the QPC, but are capable of high frequency reflectometry measurements via RF signals (HP8647A). (b) Charge stability diagram for the left DQD showing emptying to the last electrons with (n,m) denoting number of electrons for (left,right) quantum dot. Color scale shows the derivative of the QPC conductance with respect to plunger voltage. (c) Same as (b) for the right DQD.

(1,1)-(2,0) charge transition are not shown.

The spin blockade is identified by blockade of electron transport under forward bias, Fig. 5.4 (a) and (c), but not under reverse bias, 5.4 (b) and (d). In the charge sensing signals in Fig. 5.4 (a) and (b) this is seen as the colors of the bias triangles (dashed lines) being those of the (1,1) charge state, due to blockade of the (1,1)-(0,2) transition, and intermediate between those of the three charge states that transport cycles through, respectively. Blockade was also confirmed in a measurement where voltage pulses drive charge transition while $V_{SD} = 0$; Fig. 5.4 (e) shows blockade of transitions from (1,1) T_{\pm} to (0,2) S when continuously pulsing across the (1,1)-(0,2) transition as indicated by the arrows. The pulse sequence shown in (e) is explained diagrammatically in (f): The pulse sequence starts by loading the (0,1) state at **R** to “reset” the system; a pulse to **I** initializes into (1,1), loading either a singlet or a triplet; finally, pulsing to **M** lets the (1,1) singlet make the transition to (0,2), whereas the triplet cannot make the transition due to Pauli spin blockade. The pulse cycle period is $\approx 4 \mu\text{s}$ and dominated by $\tau_{\mathbf{M}} = 3 \mu\text{s}$ so that the time averaged conductance reflects the charge occupation at **M**. The triangular area in (0,2), marked with dashed lines in (e), shows time averaged QPC conductance intermediate between that of (1,1) and (0,2), due to spin blockade of the (1,1) triplets leading to an occupation that is intermediate between (1,1) and (0,2) when averaging over many cycles. For the left DQD we were not able to identify PSB in similar pulsed gate measurements at neither the (1,1)-(2,0) nor the (1,1)-(0,2) transitions. This hinders the normal read-out of spin states and hence spin manipulation measurements for the left double dot.

5.3.3 Spin blockade lifting with electric dipole spin resonance

For the right DQD, the inter-dot difference in the magnitude of the total magnetic field, ΔB , for a given external field, B_0 , is determined by measuring the lifting of PSB at the (1,1)-(0,2) transition using EDSR driven single spin rotations [102, 131, 132], see Section 2.5.1, page 30. Different magnetic field magnitudes for the two dots will give different Zeeman splittings, $\Delta E_Z = g\mu_B \Delta B$, and hence different EDSR resonance conditions, $\hbar\Delta\nu = \Delta E_Z$, for the two dots; spin blockade is then lifted at two distinct frequencies, ν , corresponding to flipping the electron spin in each of the two dots, and the difference in frequency correspond to the magnetic field difference as $\Delta B = \frac{\hbar\Delta\nu}{g\mu_B}$.

The EDSR pulse sequence is shown in Fig. 5.5. At point **M'**, Fig. 5.5 (a), the ground state configuration is (0,2) S , Fig 5.5 (b). Pulsing to a Coulomb blockade situation deep inside the (1,1) charge state, point **A'** in Fig. 5.5 (a), protects from non-resonant lifting of spin blockade by photon assisted tunneling [94], when applying microwaves to the plunger gate V_{R1} (Fig. 5.3 (a)) to induce spin rotation. The microwave burst at frequency ν and of duration $\tau_{\text{EDSR}} = 1 \mu\text{s}$ is applied at **A'** before pulsing back to **M'** and projecting onto (0,2) S for spin-state measurement, see Fig.5.5 (b) and (c). If the spin has been flipped during the microwave burst, a (1,1) triplet has been created and transitions to (0,2) S are blocked. Without spin flip events, the (1,1) S is preserved and transitions to (0,2) S occur

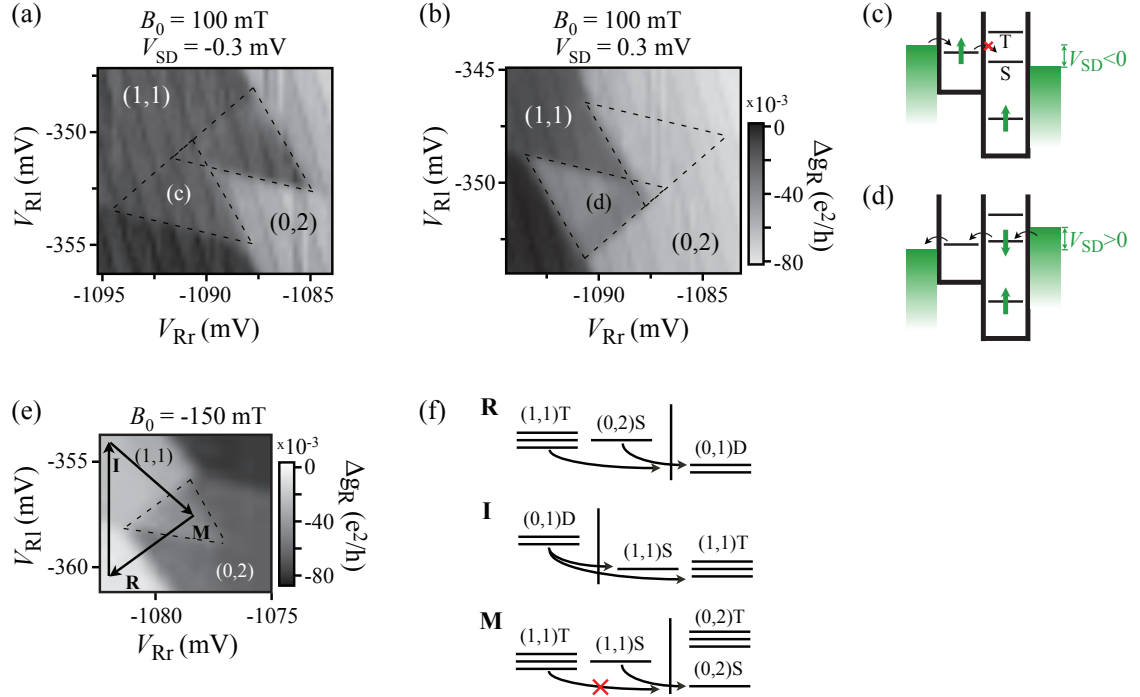


Figure 5.4: Pauli spin blockade for right DQD at (1, 1)-(0, 2) charge transition. (a) Charge sensing measurement of the (1, 1)-(0, 2) transition with negative bias $V_{SD} = -0.3$ mV and external magnetic field $B_0 = 100$ mT. Transport in the bias triangles marked by dashed lines are hindered by Pauli spin blockade, see (c), giving the triangle the same color of the (1, 1) charge state. A plane has been subtracted from the data, scale same as for (b). (b) Same as (a) for positive bias $V_{SD} = 0.3$ mV. Transport in the bias triangles (dashed lines) occurs via a series of charge states, *cf.* (d), making the triangle an intermediate color. A plane has been subtracted from the data. (c) Pauli spin blockade of electron transport under negative bias due to loading of (1, 1) triplet while (0, 2) triplet is energetically inaccessible. (d) Transport through charge cycle (0, 2) $S \rightarrow$ (1, 1) \rightarrow (0, 1) with positive bias. (e) Pauli spin blockade at the (1, 1)-(0, 2) charge transition in the right DQD, detected by continuously applying the pulse cycle $\mathbf{R} \rightarrow \mathbf{I} \rightarrow \mathbf{M} \rightarrow \mathbf{R}$, while measuring the time averaged QPC conductance. A plane background has been subtracted. (f) Diagrams showing the electrochemical potentials for the relevant charge states at the different stages in the pulse cycle. Arrows indicate transitions.

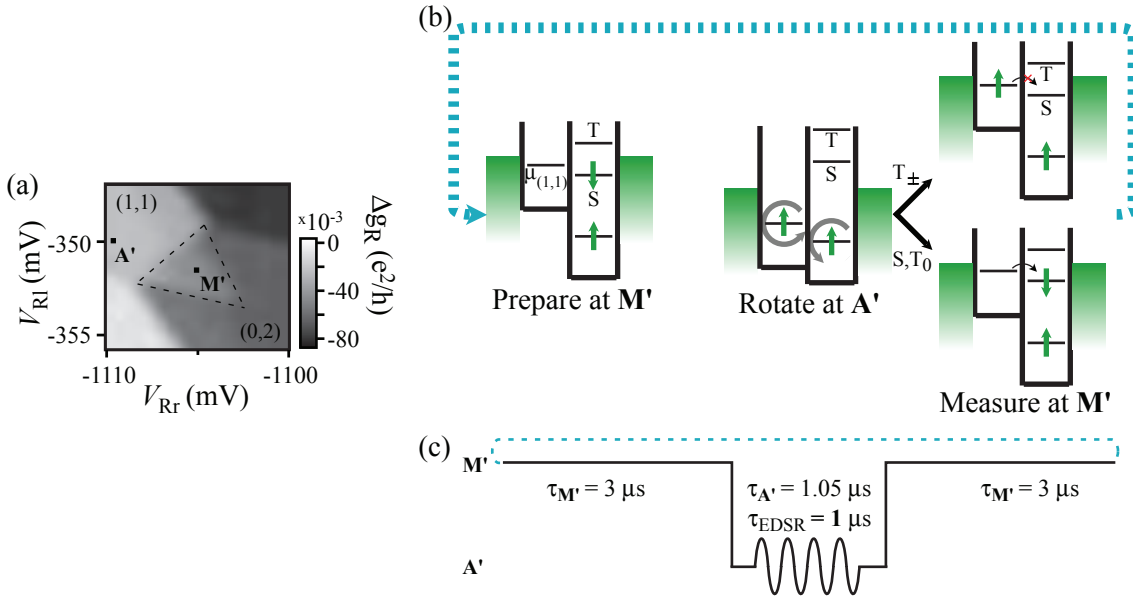


Figure 5.5: Pulse sequence for EDSR measurements. (a) Stability diagram for right DQD showing the (1,1)-(0,2) charge transition with detunings during the, $M' \rightarrow A' \rightarrow M'$ pulse cycle indicated. (b) Energy diagram showing the electrochemical potentials of the relevant charge states during the EDSR cycle. (c) The pulses applied to the plunger gates, V_{Rl} and V_{Rr} , to move between the points M' and A' in the stability diagram and drive spin rotation at A' . The cycle period is $4.05 \mu s$.

unhindered leaving the system re-initialized for the next pulse cycle. Re-initialization from the blocked $(1,1)T_{\pm}$ states depends on spin relaxation to $(0,2)S$ at the measurement point and may not be 100 % effective.

Spin flip events are detected by monitoring the conductance through the right QPC, g_R ; without spin flip the system is dominated by the $(0,2)$ charge configuration, but remains in the $(1,1)$ charge configuration for a longer time in case of spin flip, leading to a higher average conductance through the QPC during a cycle with spin flip.

The change in g_R is monitored via the voltage V_{QPC} across the QPC biased at 1 nA dc and 1 nA ac at 257 Hz. To increase sensitivity the microwaves are chopped at 207.3 Hz and the change in V_{QPC} is measured by homodyne detection using a lock-in amplifier with a time constant of 100 ms. The signal is averaged to remove field and frequency independent features, such as resonances from the microwave circuit (still visible in Fig. 5.6 (a)).

Figure 5.6 (a) shows the resulting measurement of V_{QPC} when continuously driving the EDSR pulse sequence, Fig. 5.5 (c), while sweeping the microwave frequency, ν , and stepping the magnetic field, B_0 . Lifting of spin blockade at resonance conditions, $h\nu = g\mu_B B$, is seen as a drop in V_{QPC} (dark color) at frequencies, ν , proportional to B_0 ¹. The lin-

¹Note that we microwave chopping would expect the sensor signal to show a peak on resonance with instead of a drop. A possible explanation for the reversed sign of the change in signal on resonance could

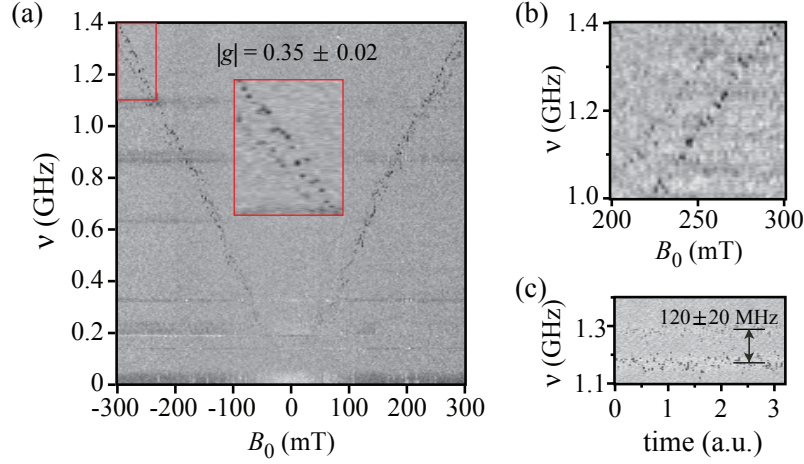


Figure 5.6: EDSR spectroscopy. (a) Charge sensor voltage, V_{QPC} , vs ν vs B_0 showing a dip in V_{QPC} (darker) corresponding to creation of spin blockade when resonance conditions ($h\nu = g\mu_B B$) for spin flip are met. Insert (red box) shows magnified view of upper left corner of plot, where splitting of resonance is visible. Horizontal features stem from resonances in the microwave circuit. (b) Same as (a) showing the splitting of the resonance due to the different magnetic field at the positions of the two dots, $\Delta|\mathbf{B}|$. (c) The split resonance with $B_0 = 250$ mT, showing the splitting of the resonance 120 ± 20 MHz corresponding to $\approx 25 \pm 4$ mT using $g = 0.4$. The jitter in the resonances giving the uncertainty is attributed to the randomly fluctuating nuclear fields.

ear relationship between resonance frequency and B_0 is a sure indication of driven spin resonance between levels split by the Zeeman splitting $\Delta E_Z = g\mu_B B$. The slope of the resonance feature corresponds to $|g| = 0.35 \pm 0.02$, which is similar to values found in equivalent systems [101, 102, 131, 190].

The resonance disappears around $B_0 = 0$ due to the independently fluctuating effective nuclear magnetic fields, B_N , in the two dots. The random inter-dot difference in nuclear magnetic field, ΔB_N , lifts spin blockade by coupling the triplet states, T_0 , T_+ and T_- , to the singlet, S , when the magnetic field and the exchange splitting between S and T_0 , J , are sufficiently small, $\Delta B_N > B, J(\epsilon_M)$ [103, 133], see Section 2.4.1, page 22, causing measurement contrast to disappear. Note that the microwave independent blockade lifting around $B_0 = 0$ [103] is not visible in Fig. 5.6 (a), both due to our measurement cycle, Fig. 5.5 (b), and the microwave chopping synced sensing [102]; we are only sensitive to events causing spin blockade, and only so if they are synced with the microwave chopping.

For sufficiently large external magnetic fields, $B_0 > 200$ mT, the resonance line becomes visibly split, see insert Fig. 5.6 (a), due to the magnetization of the micro-magnet creating a difference in Zeeman splitting fields, ΔB_M , between the positions of the two quantum

be loading into $(1,1)T_+$ instead of $(1,1)S$ at \mathbf{A}' . Still, however the sign of the signal change, the resonance effect is clear and for the extent of the investigation presented here we can disregard the discrepancy in the sign of the change.

dots such that $\Delta B_M > B_N$. The two resonance lines, one corresponding to the resonance condition in each dot, are shown in Fig. 5.6 (b). The resonances are split by $\Delta B_M \sim 25$ mT and based on the magnet simulations, see Fig. 5.2, B_M^y should add to B_0 meaning that the higher frequency resonance should correspond to the dot with the larger $|\mathbf{B}_M|$. Again, according to the magnet simulation, Fig. 5.2 (f), the rightmost quantum dot, QD_{Rr}, should have the greater $|\mathbf{B}_M|$, although only slightly. However, the difference would increase dramatically for the left dot, QD_{Rl}, further away from the large top gate than the right dot, QD_{Rr}; such relative positioning corresponds well with the different plunger gate voltages, $V_{Rl} \sim -300$ mV and $V_{Rr} \sim -1000$ mV, around the charge transition (1,1)-(0,2), *cf.* Fig. 5.3 (c).

The resonances signals also have different magnitudes, but unlike in continuous microwave EDSR experiments [131, 132] signal strength cannot be related to dot position relative to the microwave gate in our pump-and-probe experiment, since the pulse cycle duration sets the frequency for measuring EDSR spin flip events irrespective of the strength of the microwave signal at the dots. Additionally, a relation between signal strength and distance to microwave gate would be inconsistent with the change of relative magnitude of the split signals observed between the insert in Fig. 5.6 (a) and 5.6 (b).

Jitter in the position of the resonances at a given magnetic field is clear in Fig. 5.6 (c), where ν is swept across both resonances repeatedly in a constant external field $B = 250$ mT. We attribute this jitter to random fluctuations in the nuclear magnetic field between measurements [102]. The range of the jitter is $\sim \pm 20$ MHz for each of the resonances, roughly corresponding to a fluctuating field of ~ 4 mT in agreement with measurements in similar devices [96, 102, 103, 116].

The intensity of the resonance in Fig. 5.6 (a) does not seem to increase with B_0 , however, it is visibly weaker for $B \lesssim 100$ mT. Scaling of resonance intensity with B_0 would be expected for EDSR mediated by spin-orbit coupling [25, 111] and micro-magnet induced magnetic gradients², but not for hyperfine mediated spin resonance [102]. We have not investigated the dependence of resonance strength on τ_{EDSR} , and cannot say whether Rabi oscillations in resonance strength occur nor whether there is a dependence of Rabi frequency on B_0 . Therefore, it remains uncertain whether the spin resonance is induced by random inhomogeneity of the nuclear magnetic field [102], a gradient from micro-magnet perpendicular to external field [102, 131] or spin-orbit coupling [111]³.

Further measurements are needed to the fully establish the EDSR mechanism and to estimate the perpendicular components of the micro-magnet magnetic field on the way to demonstrating qubit operation in the few-electron DQD w. magnetic gates, either in the single electron basis or in the S - T_0 basis.

²Assuming that the magnetic field gradients scale with the magnetization in the external magnetic field.

³We note that the direction of the crystal axis, the magnetic and electric field are the same as in Ref. [111] where spin-orbit driven EDSR and coherent oscillations were observed.

In the next section, we turn away from the two-electron DQD and investigate the possibility of a multi-electron DQD spin qubit.

5.4 Multi-electron double quantum dots for singlet-triplet spin qubits

5.4.1 Introduction

Single electron (double) quantum dots have become the standard starting point for experiments with electrostatically defined and controlled electron spin qubits in solid state systems such as GaAs [98, 116], InAs [25] and Si [64]. As the state of the field moves from single qubit operation to coupling qubits and realizing two or multiple qubit gates [98, 122] the scalability of a given system becomes a determining factor for its continued progress. Traditionally, solid-state qubits including electrostatically defined lateral DQDs in semiconductor heterostructures, have been promoted on their promise of scalability [33, 97], but the prospect of dense arrays of gate defined single electron quantum dots fabricated routinely is hampered by the presence of defects and charge traps in the heterostructure hosting the quantum dots. In *e.g.* GaAs/AlGaAs heterostructure 2DEGs the presence of charged impurity centers and defect states can cause problems by distorting the potential landscape, making the single electron regime inaccessible, and by creating charge noise from switching occupation of the impurity and defect state [124], causing decoherence and gate errors in singlet-triplet spin qubits by affecting the exchange coupling, J [98, 116]. Operating the single electron qubit at so-called “sweet spots” might lower the sensitivity of the exchange energy to charge noise [117, 191–195], but is impractical when scaling to multiple qubits and would still leave the qubit vulnerable to a distorted potential making the single electron regime inaccessible. A better alternative might be using qubits with several electrons per dot, where paired-up “core” electrons would screen a single “valence” electron from charge noise [187]. In addition to the beneficial screening, multi-electron qubits should not be as sensitive to distorting effects of impurities and thus be easier to fabricate with a high yield than single electron qubits, offering a practical advantage in terms of scaling.

In the context of multi-electron quantum dots for spin qubits, “multi-electron” means enough “core” electrons to provide screening, but not so many that the dot excitation energies becomes too small to have well defined qubit states [187, 196, 197]. The exact number of electrons per dot for these criteria to be met is not known in advance and could depend on the quantum dot and qubit geometries.

Here, we wish to examine the multielectron-per-dot regime for a double quantum dot with the prospect of using this as a singlet-triplet (S - T_0) qubit. We first investigate the occurrence of spin blockade in the multielectron regime, before we measure the singlet-triplet exchange energy, J , and obtain an estimate of T_2^* from measuring dephasing of the separated singlet.

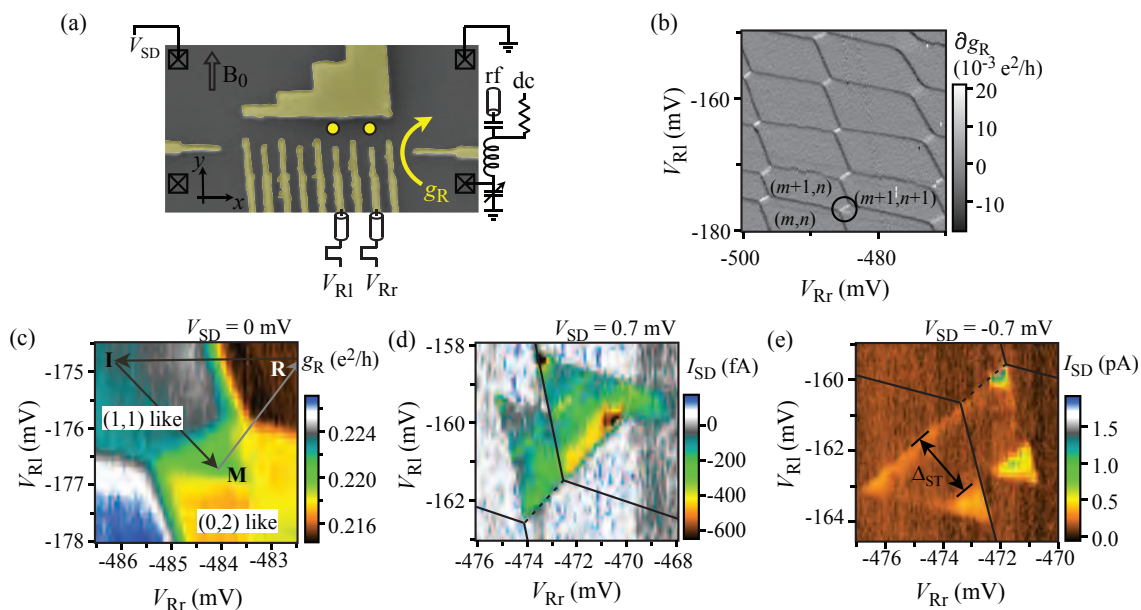


Figure 5.7: Spin blockade in multi-electron double quantum dot. (a) Micrograph of device identical to the measured, with ohmic contacts indicated by crossed squares and an arrow marking the QPC used for charge sensing. The positions of the dots defined by the gates are marked by yellow dots. The plunger gates V_{Rl} and V_{Rr} control the potentials on the dots and are both connected through high frequency coaxial cable to waveform generators (Tektronix AWG520). The charge sensor quantum point contact, g_R is in the following measurements only used for standard lock-in measurement of the time average conductance of the QPC. (b) Charge stability diagram showing tuning of the electron occupation numbers with plunger gate voltages. (n,m) denote number of electrons for (left,right) quantum dot. Color scale shows the derivative of the QPC conductance with respect to plunger voltage. The circle indicates the spin blocked transition measured in (c)-(e). (c) Charge sensing measurement of the transition circled in (b) while applying pulse cycle $R \rightarrow I \rightarrow M$ indicated by arrows. The measurement shows a blocked transition that we interpret in analogy to the $(1,1)$ - $(0,2)$ spin blockade. (d) and (e) Transport measurement of transition circled in (b), under positive, (d), and negative, (e), source-drain voltage bias. The allowed transport in the full bias triangles for one bias direction and a gap analogous to the $(0,2)$ singlet-triplet splitting, $\Delta_{ST} \approx 0.4$ meV, for the other bias direction indicates a Pauli spin blockade.

5.4.2 Pauli spin blockade in the multielectron regime

Fig. 5.7 (a) shows a SEM micrograph of a GaAs/AlGaAs heterostructure device similar to the one measured here with the top depletion gates in false-color yellow and the positions of the quantum dots in the 2DEG marked by yellow dots. The plunger gates for the two dots, V_{Rl} and V_{Rr} , are connected to the outputs of an arbitrary waveform generator (AWG520) through high frequency coaxial cabling to allow for fast changes of plunger voltage. Charge transitions in the DQD are measured from the time-averaged change in conductance, ∂g_R of a nearby quantum point contact acting as charge sensor. Transport

5.4. Multi-electron double quantum dots for S - T_0 spin qubits

through the DQD can be measured in response to applying a dc voltage, V_{SD} , across the DQD. Ohmic contacts to the 2DEG are marked by crossed boxes. The direction of the externally applied field, B_0 , is indicated by an arrow - unless noted otherwise, $B_0 = 0$.

Fig. 5.7 (b) shows a double dot stability diagram in terms of the derivative of QPC conductance with respect to plunger voltage, ∂g_R , as a function of plunger gate voltages, V_{Rr} and V_{Rl} . Several charge states, (m, n) , are visible, with m and n denoting number of electrons in left and right dots, respectively. The absolute number of electrons on the dots in the measurements presented here is not known exactly, since it was not possible to empty the dots to the last electrons, due to instabilities in the right dot.

Spin blockades at inter-dot charge transitions depend on the ground state spin configurations for the involved charge states. At the $(1,1)$ - $(0,2)$ transition we know that for low magnetic fields the $(0, 2)$ ground state is a singlet, and spin blockade of the $(1,1)$ - $(0,2)$ transition will occur if a $(1, 1)$ triplet is loaded [93, 95, 96]. However, for higher numbers of electron occupation level degeneracies and electron-electron interactions may affect the single dot spin filling spectrum and create non-trivial ground states similar to what seen in the filling of atomic shells [198, 199]. The appearance of atom-like shell filling is dependent on a spatially symmetric confinement potential and level quantization of the same magnitude as the Coulomb interaction [198]. Such shell-filling has been observed in single vertical quantum dots by ground state spectroscopy of electron occupation from zero to more than 30 electrons [200], and also observed for the four-electron ground state in a lateral quantum dot [201]. For a broken spatial symmetry, usually the case for laterally defined quantum dots containing $\gtrsim 10$ electrons [197, 202], we expect simple even-odd spin filling for a system where confinement effects dominate over interaction effects. However, absence of both even-odd spin filling and atom-like shell filling have also been reported for a lateral few-electron quantum dot [203], as well as the absence of spin degeneracy for an otherwise single-particle spectrum dot [204]. Both are supposedly the result of different degrees of electron-electron interactions. For DQDs the picture becomes even more unclear as the inter-dot coupling will play an important role as well [199]; even-odd spin filling behavior has been observed in both few- [96] and multi-electron lateral DQDs [205], and some shell-filling signatures have been observed in a vertical few-electron DQD [206].

Such different energy level spectra for quantum dots, showing examples of both many-body and single-particle behavior depending on the specific realization and tuning of a given quantum dot [204, 207], leaves the question of expected spin filling behavior in our double quantum dot open.

With no knowledge of absolute occupation numbers or expected spin filling behavior, we searched for spin blockade at the nine bottommost inter-dot transitions shown in Fig. 5.7 (b), by pulsing around the transitions as indicated in panel (c). Driving the pulse cycle $\mathbf{R} \rightarrow \mathbf{I} \rightarrow \mathbf{M}$ will detect spin blockade when the transition $\mathbf{I} \rightarrow \mathbf{M}$ involves a transition from a $(1,1)$ -like state to a $(0,2)$ -like state, but will not detect $(1,1)$ - to $(2,0)$ -like spin blockades as this would require the opposite pulse direction. For even-odd spin filling we should detect spin blockade at every second transition in every second column with the

given pulse cycle. For a spin blocked transition, the pulse sequence in Fig 5.7 (c) will, starting from a (1,2)-like state at \mathbf{R} , initialize into a (1,1)-like state at \mathbf{I} with an equal probability of singlet and triplet. Pulsing to \mathbf{M} , where $> 80\%$ of the pulse cycle is spent and thus dominates the charge sensing signal, the transition to the (0,2)-like state will be blocked for (1,1)-like triplets, making the spin blocked pulse triangle a color intermediate between the (1,1)- and (0,2)-like charge states as seen in Fig. 5.7 (c). The spin blocked transition shown in panel (c) was the only one detected in the pulsed measurements of the nine transitions. The location of the spin blockade is indicated in panel (b) by a circle, and for even-odd spin filling, we would expect the inter-dot transition two up from this to also show blockade, but this was not the case. The presence of spin blockade at the circled transition was confirmed by transport measurements with positive bias, (d), showing no blockade and with negative bias, (e), showing blockade with an (0,2)-like singlet-triplet splitting $\Delta_{ST} \approx 0.44 \text{ meV}$, in agreement with values found for similar few-electron dots [96]. Note that the gate voltages are different for the transport measurements, due to a shift in the charge stability diagram moving all transitions to less negative gate voltages for both plungers. The absence of spin blockade at the transition two up from that measured in (d) and (e) was also confirmed with transport measurements (data not shown).

The apparent absence of even-odd spin filling weakens the analogy of the observed spin-blocked transition to the well understood (1,1)T-(0,2)S spin blockade, as we do not have a reason to assume that the simple level spectrum of the (1,1)-(0,2) transition applies to the $(m+1, n)-(m, n+1)$ transition in the multi-electron dots. To further investigate the (1,1)T-(0,2)S analogy of the observed spin-blocked transition in the multi-electron DQD, we performed measurements of the exchange energy, J , and the ensemble spin decoherence time, T_2^* , both measurements that are performed for characterization and operation info for two-electron DQD $S-T_0$ spin qubits [116, 208].

5.4.3 Measurement of exchange energy vs detuning

For the (1, 1)-(0, 2) charge transition in a two-electron DQD we can write up the spin-states of the two charge configurations and their dependence on detuning from degeneracy, ϵ , and magnetic field, B [93, 94]; it is this knowledge that lays the basis for the use of this system as a spin qubit [97].

For a multi-electron DQD the relevant spin configurations for a spin blocked $(m+1, n)-(m, n+1)$ charge transition are not generally known or easily deduced without knowledge of the energy level spectrum, absolute electron number in each dot and the effects of electron-electron interactions on the level spectrum. In the simplest case, the m and $n-1$ electrons constitute filled, inert shells and we can effectively reduce the system to two spin degenerate levels, one in each dot, leading to a close analogy between the (1, 1)-(0, 2) and the $(m+1, n)-(m, n+1)$ charge transitions.

Here we will perform a measurement used for determination of the exchange splitting, J , between the states S and T_0 in two-electron DQDs [116] on a spin blocked charge transition in a multi-electron DQD. The result of the measurement will tell about the

5.4. Multi-electron double quantum dots for S - T_0 spin qubits

likeness of the $(m+1, n)$ - $(m, n+1)$ level spectrum to that of the $(1, 1)$ - $(0, 2)$ transition and hence the suitability of the multi-electron DQD as a S - T_0 -style qubit.

For a two-electron DQD the measurement of the exchange splitting, $J(\varepsilon)$, can be explained by considering the energy dependence of the two-electron spin-states near the $(1, 1)$ - $(0, 2)$ degeneracy, Fig. 5.8(a), the detuning from degeneracy denoted by ε . The two electrons give four possible spin configuration: one singlet, denoted S ; and three triplet states, denoted T_- , T_0 and T_+ , corresponding to $m_S = -1, 0, 1$. For $\varepsilon > 0$ the ground-state charge configuration is $(0, 2)$, and due to tight confinement the spin-singlet, denoted $(0, 2)S$, forms the ground-state with the spin-triplet states much higher in energy (~ 0.4 meV, see Fig. 5.7 (e)) and not relevant for this discussion.

For $\varepsilon < 0$ the ground-state charge configuration is $(1, 1)$ and all four states, denoted simply by their spin configuration, S , T_- , T_0 and T_+ , are degenerate in absence of magnetic field and interdot tunneling, $t_c = 0$ (grey, dotted lines). In a magnetic field, B , T_{\pm} are split off by the Zeeman energy $E_Z = \pm g\mu_B B$, where $\mu_B = 5.788 \times 10^{-5}$ eV/T is the Bohr magneton and $g = -0.44$ is the electron g -factor in GaAs, while S and T_0 remain degenerate.

For a finite interdot tunnel coupling, t_c , the S and $(0, 2)S$ states hybridize around the $(1, 1)$ - $(0, 2)$ degeneracy point, $\varepsilon = 0$, creating a detuning dependent splitting, $J(\varepsilon)$, between the hybridized singlet S and T_0 , with $J(0) = t_c$ and $J(\varepsilon) \rightarrow 0$ for large negative detuning, $\varepsilon \ll -t_c$. With $E_Z < t_c$ S and T_+ cross at $\varepsilon < 0$ when $J(\varepsilon) = E_Z = g\mu_B B$, and here, transitions between the two states occur due to a differences in both effective nuclear magnetic fields, $\Delta\mathbf{B}_N$, and micro-magnet magnetic field, $\Delta\mathbf{B}_M$, for the two dots [133].

The $S \leftrightarrow T_+$ transitions are used to measure the exchange splitting by driving the pulse sequence shown in Fig. 5.8(b) [116, 208]. An $(0, 2)S$ is prepared by waiting 80 ns at \mathbf{P} allowing $T \rightarrow (0, 1) \rightarrow (0, 2)S$ transition to occur for any initial triplet states and pulsed to \mathbf{P}' , waiting another 80 ns before pulsing to the separation point, \mathbf{S}' , allowing the created $(1, 1)$ singlet S to evolve for $\tau_{\mathbf{S}'} = 80$ ns at detuning, $\varepsilon_{\mathbf{S}'}$. Readout of the resulting spin state is done by pulsing to \mathbf{M} for $1.5 \mu\text{s}$, projecting the evolved separated state onto $(0, 2)S$. For \mathbf{M} inside the spin blockade triangle, transitions to $(0, 2)S$ are only allowed for the singlet state S , whereas transitions from the triplet state, T_+ , are blocked, leading to a higher charge sensor conductance as the $(1, 1)$ charge configuration is kept. Since transitions between S and T_+ only occur for $\varepsilon_{\mathbf{S}'}$ at the S - T_+ degeneracy where $J(\varepsilon) = g\mu_B B$, we can thereby measure the exchange splitting by mapping this degeneracy against B_0 and ε . In Fig. 5.8 (b) a measurement for the multi-electron DQD at $B_0 = 100$ mT shows two S - T_+ transition features (dotted lines) corresponding to $J(-0.39 \text{ mV}) = J(-0.56 \text{ mV}) = 2.5 \mu\text{eV}$. The appearance of blocked transitions for two separation detunings is not expected from the two-electron case and could suggest that the simple two-electron picture of Fig. 5.8 (a) is not sufficient to describe the transition in the multi-electron DQD.

To investigate the double feature further a mapping of $J(\varepsilon)$ vs B_0 and ε is performed. The \mathbf{S}' - \mathbf{M} separation is kept constant and \mathbf{M} is swept along the detuning axis, ε , indicated in Fig. 5.8 (c), where the axis is superimposed on a measurement indicating the spin

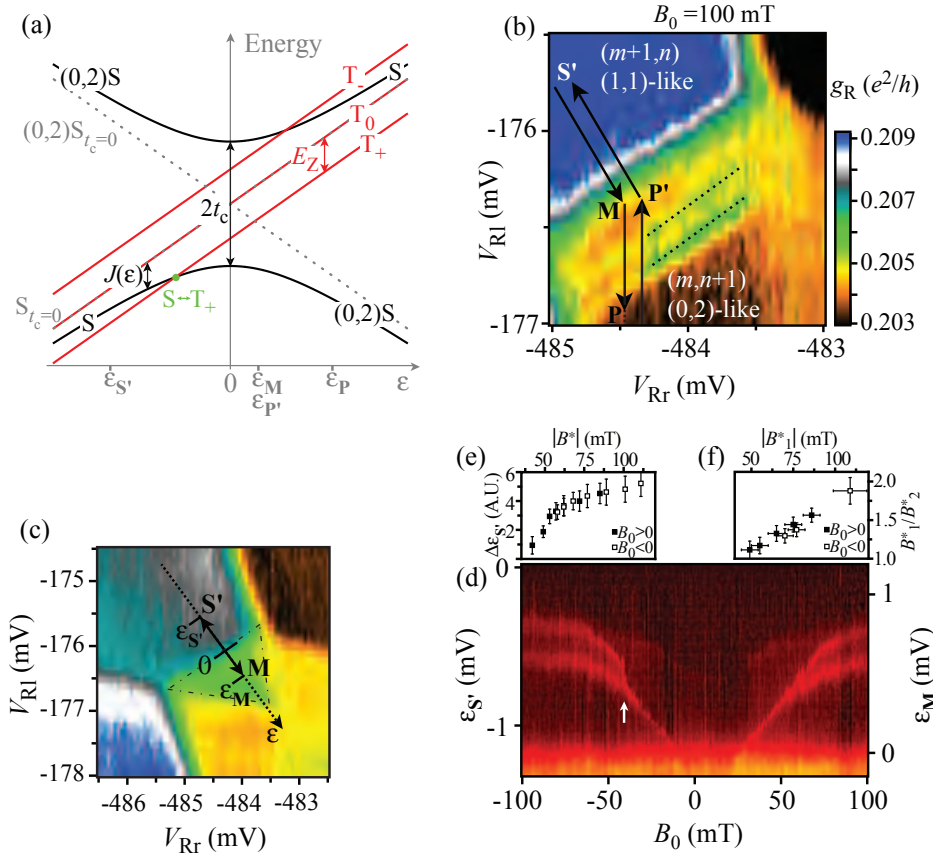


Figure 5.8: Measurement identical to that of the exchange splitting, $J(\epsilon)$, between $(1,1)S$ and $(1,1)T_0$ as a function of detuning, ϵ , from $(1,1)S$ - $(0,2)S$ degeneracy for a spin-blocked $(m+1, n)$ - $(m, n+1)$ transition in a multi-electron DQD. (a) Diagram showing the dependence of the relevant energy levels for a $(1,1)$ - $(0,2)$ charge transition on the detuning, ϵ , of $(1,1)S$ and $(0,2)S$. The $(1,1)$ states are denoted by their spin configurations only, S , T_0 , T_- and T_+ , and the $(0,2)$ singlet is denoted by both charge and spin configuration, $(0,2)S$. The tunnel coupling, t_c , between dots causes S and $(0,2)S$ to hybridize, creating a detuning dependent splitting, $J(\epsilon)$, between S and T_0 . A magnetic field, B , splits the triplet states T_{\pm} from T_0 by $E_Z = g\mu_B B$. (b) Charge stability diagram around the $(m+1, n)$ - $(m, n+1)$ transition measured while applying the pulse cycle indicated by arrows used in the exchange energy measurements. The cycle consists of $(0,2)S$ preparation, P and P' , separation to $(1,1)S$ and evolution, S' , and measurement, M , by projecting onto $(0,2)S$. In the $(1,1)$ - $(0,2)$ -case, the rapid mixing of S and T_+ at their crossing leads to a partially blocked transition to $(0,2)S$ upon pulsing to M . The measurement for the multi-electron DQD, with $B = 100$ mT, shows two such blockade features (dotted lines) separated by $\Delta\epsilon \approx 0.17$ mV. (c) Detuning axis (dotted line), which the measurement point of the $P \rightarrow P' \rightarrow S' \rightarrow M$ pulse cycle is swept along for the measurement in (d), superimposed on a charge stability diagram showing the triangular spin blockade region (green) within which M should fall. The separation pulse is of constant magnitude, as indicated by the double arrow. (d) Spin funnel measurement mapping the detuning position of S - T_+ -crossing, vs applied magnetic field, B_0 , translating to $J(\epsilon)$ vs B_0 since $J(\epsilon) = g\mu_B B$ at the crossing. For $\epsilon_P < 0$ M lies outside the spin blockade and measurement is not possible. (e) Splitting in detuning, $\Delta\epsilon_{S'}$, vs magnetic field corrected for offset, $B^* = B_0 - 13$ mT. Uncertainty for both (e) and (f) is widths of the funnel arms. (f) Ratio of offset-corrected magnet fields for lower, B_1^* , and upper, B_2^* , funnel arms at given detunings denoted by corresponding value of $|B_1^*|$.

blockade region in which \mathbf{M} should fall (dash dotted lines). Fig. 5.8 (d) shows the measurement of the singlet probability (dark is high probability, red is low) of the separated state as a function of B_0 and separation detuning $\varepsilon_{\mathbf{S}'}$. For $\varepsilon_{\mathbf{M}} < 0$ \mathbf{M} lies outside the spin blockade and measurement contrast is lost. A so-called spin funnel feature is apparent in the measurement and shows that the double feature develops with magnetic field, visible for $|B_0| \gtrsim 50$ mT. The funnel feature is not symmetric in B_0 , probably due to the magnetic gates creating offsets of $\simeq 8$ mT and $\simeq 13$ mT for the unsplit and split part of the funnel, respectively. The two distinct offsets could be caused by a switch in the magnetization of the gates as the external field is ramped from -100 mT to 100 mT, in agreement with the abrupt disappearance of the splitting at $B \simeq -40$ mT (see white arrow). Fig. 5.8 (e) shows the difference in detuning, $\Delta\varepsilon$ between the split arms of the funnel in arbitrary units vs magnetic field corrected for offset, $B^* = B_0 - 13$ mT. The splitting is not linear in magnetic field, increasing more slowly with increasing field. Fig. 5.8 (f) shows the splitting of the funnel arms in terms of ratio of offset-corrected magnetic fields for lower, B_1^* , and upper, B_2^* , arms for different detunings denoted by their corresponding B_1^* . The ratio B_1^*/B_2^* is not constant as would be the case for a funnel splitting caused by two states of differing m_S inducing transitions to spin blocked states. In that case $B_1^*/B_2^* = m_{S,2}/m_{S,1}$ rather than $B_1^*/B_2^* \propto B_1^*$.

We speculate that the splitting could be caused by magnetic field gradients between the two dots due to the magnetic field from the magnetized gate structure. This would be consistent with the linear increase of the magnetic field splitting of the funnel arms with increasing magnetic field, see Fig. 5.8 (f), assuming a linear increase of the magnetization of the gate micro-magnet with external field, B_0 . However, a splitting like this was not observed in a exchange energy measurement on a two-electron double dot with a large (~ 100 mT) nuclear magnetic field and field gradient between the two dots created and stabilized by dynamic nuclear polarization [135].

As a final point of comparison to the two-electron DQD, we will investigate the decoherence time, T_2^* , for the spin blocked transition in the multi-electron DQD at larger separation detunings such that $J(\varepsilon) < g\mu_B\Delta B_N$ and the S and T_0 states are mixed by the hyperfine fields [116].

5.4.4 Dephasing of the separated singlet for T_2^* estimate

Measurement of the time a spin state can maintain coherence once separated, e.g. $(0, 2)S$ into $(1, 1)$, is important in terms of the timescale of operations performed on the separated state. Here, we want to obtain this timescale, T_2^* , for the multi-electron DQD in order to compare it to previously obtained values for similar two-electron systems.

The pulse sequence used for the measurement is the same as that used for the measurement of $J(\varepsilon)$, Fig. 5.8 (b), only, the separation pulse is much larger ($\Delta\varepsilon_{\mathbf{S}'\mathbf{M}} = 2.4$ mV) making the separation detuning, $\varepsilon_{\mathbf{S}'}$, much more negative, see Fig. 5.9 (a) and top left panel in (b). Again, we return to the two-level S - T_0 picture to explain the idea of the measurement. At large, negative detuning, where $J(\varepsilon) < g\mu_B\Delta B_Z$, the singlet S and triplet T_0

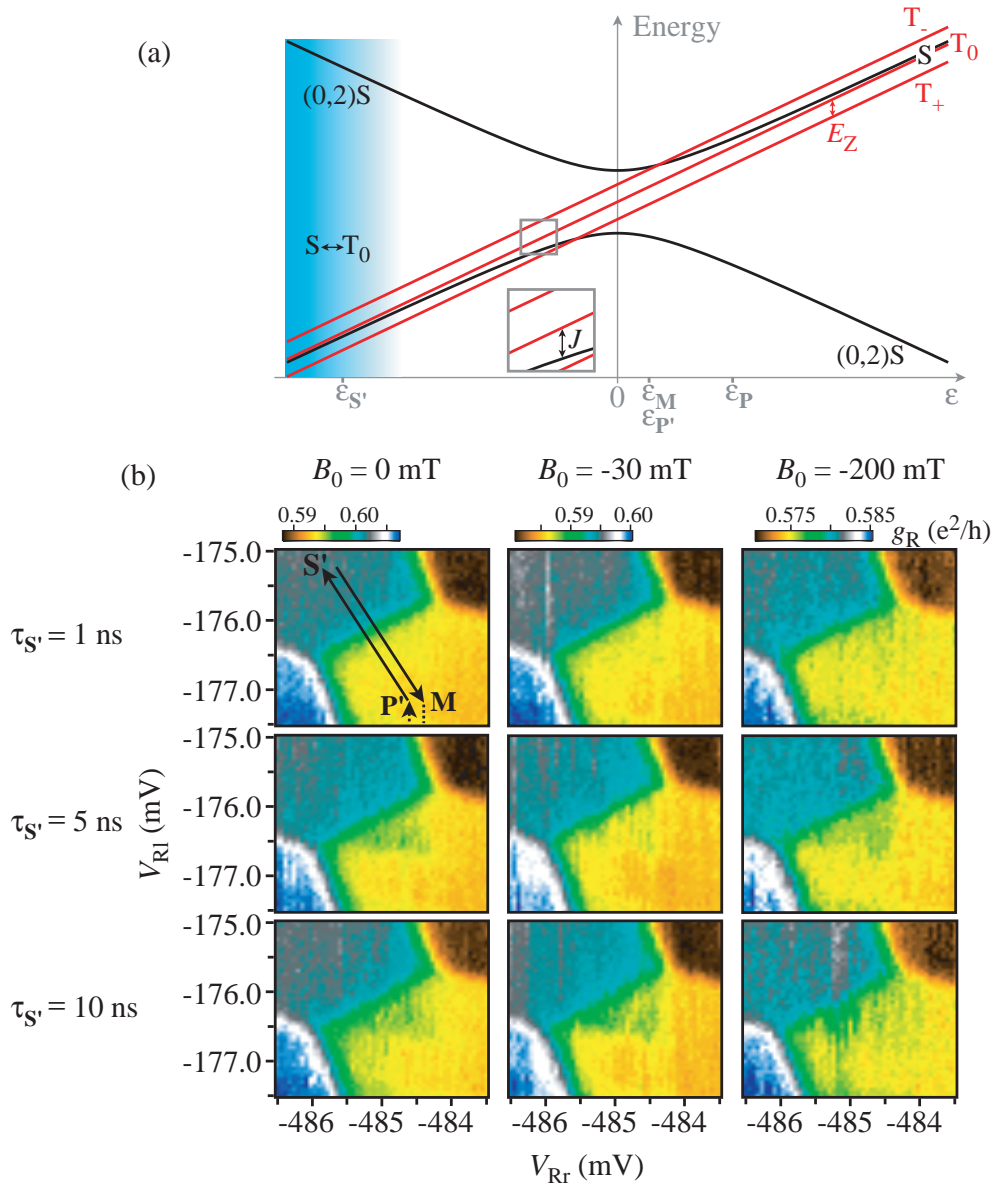


Figure 5.9: Decoherence of the separated spins at large detuning $\epsilon < 0$. (a) Diagram showing the dependence of the relevant energy levels for a $(1,1)$ - $(0,2)$ charge transition on the detuning, ϵ , of $(1,1)S$ and $(0,2)S$. The $(1,1)$ states are denoted by their spin configurations only, S , T_0 , T_- and T_+ , and the $(0,2)$ singlet is denoted by both charge and spin configuration, $(0,2)S$. At large, negative detunings (light blue shaded region) the exchange splitting, J , between S and T_0 becomes smaller than the effect of the fluctuating difference in the nuclear fields for the two dots, leading to transitions between S and T_0 . The approximate detunings for the different points in the pulse cycle in (b) are indicated (b) Pulsed spin blockade measurement for different separation times $\tau_{S'}$ and external magnetic fields B_0 . Color scale is charge sensor conductance. The pulse cycle indicated (\mathbf{P} outside of view) prepares an $(0,2)S$ at \mathbf{P}' , before pulsing deep into $(1,1)$ to \mathbf{S}' where the state is allowed to evolve for $\tau_{S'}$. Pulsing back to $(0,2)$ at \mathbf{M} measures the singlet component of the evolved state.

5.4. Multi-electron double quantum dots for S - T_0 spin qubits

are no longer protected by the exchange splitting, J , from decoherence due to differences in the magnetic fields in the two dots along axis of the applied field, ΔB_Z [116], light blue region in Fig.5.9 (a). In our case this difference stems from both random nuclear fields and the micro-magnet field gradients. The field difference translates to a difference in energy between $|\uparrow\downarrow\rangle$ and $|\downarrow\uparrow\rangle$ causing a phase accumulation between the two, driving transitions between $S = 1/\sqrt{2}(|\uparrow\downarrow\rangle - |\downarrow\uparrow\rangle)$ and $T_0 = 1/\sqrt{2}(|\uparrow\downarrow\rangle + |\downarrow\uparrow\rangle)$ while the system is kept at detuning $\varepsilon_{S'}$. In an external magnetic field, B_0 , the remaining triplet states T_{\pm} are split off, restricting the system to S - T_0 transitions. Projecting the evolved state back onto $(0, 2)S$ measures singlet (unblocked) and triplet (blocked) components of the evolved state. Varying the evolution time, $\tau_{S'}$, allows measurement of the spin decoherence time, T_2^* , as the evolution time needed for the probability of blockade of the (1,1)-(0,2) transition to saturate [116]. The nuclear field, \mathbf{B}_N evolves on a timescale of $\sim 1 \mu\text{s}$ [116], so that the field difference, $\Delta\mathbf{B}_N$, is static on the timescale of electron spin dynamics ($\sim \text{ns}$) [116], but changes randomly between the individual measurement cycles lasting $4.2 \mu\text{s}$ of which $4 \mu\text{s}$ are spent at the measurement point. Averaging over approximately 25 measurement cycles per measurement point gives an ensemble average of the spin decoherence time, T_2^* . We perform an estimation of T_2^* for our multi-electron double quantum dot by measuring the appearance of the spin blockade for three values of $\tau_{S'}$ both with and without magnetic field, Fig, 5.9 (b). In the absence of external magnetic field S is additionally mixed with T_{\pm} , due to inter-dot magnetic field differences in the transverse plane, ΔB^x and ΔB^z , causing the probability of blockade upon projection to increase compared to a situation with magnetic field⁴ [116]. The first column in Fig. 5.9 (b) shows measurements for $B_0 = 0$ for $\tau_{S'} = 1, 5$ and 10 ns (top to bottom). The characteristic spin blockade triangle is absent for $\tau_{S'} = 1 \text{ ns}$, indicating that the singlet spin state has been preserved. For $\tau_{S'} = 5$ and 10 ns the signature spin blockade triangle is visible and does not seem increase in visibility, indicating that $T_2^* \lesssim 5 \text{ ns}$ and certainly less than the $T_2^* = 10 \text{ ns}$ reported in reference [116] for a two-electron double dot. The measurements for $B_0 = -30 \text{ mT}$ (middle column) and -200 mT (right column) are less clear cut. For $\tau_{S'} = 1 \text{ ns}$ it still seems that the singlet state is preserved, although spin blockade is beginning to develop for $B = -200 \text{ mT}$. For $\tau_{S'} = 5 \text{ ns}$ the spin blockade is visible for both $B_0 = -30$ and -200 mT , but less so for $B_0 = -30 \text{ mT}$ compared to $B_0 = 0$ and -200 mT . For $\tau_{S'} = 10 \text{ ns}$ the visibility of the blockade has risen for $B_0 = -30 \text{ mT}$, so that it seems even more pronounced than compared to $B_0 = 0$ in contrast to the behavior observed for a two-electron S - T_0 system without a micro-magnet [116]. For $B_0 = -200 \text{ mT}$ and $\tau_{S'} = 10 \text{ ns}$ the visibility of the blockade is slightly degraded compared to $B_0 = -30 \text{ mT}$. Measurements for $\tau_{S'} > 10 \text{ ns}$ were also performed, but no new trends were observed. It should be noted that there is some uncertainty to the effective field experienced by the quantum dot, due to the magnetization of the magnetic gate structure. However, the offsets seen were around 10 mT and

⁴In the absence of an external magnetic field, the spin quantization axis is set by the local quasi static hyperfine field in the dots and any remnant field from the micro-magnet.

should not change the relative magnitudes of the fields.

The sign of beginning spin decoherence after only 1 ns at $B_0 = -200$ mT, is likely due to a difference in the magnetic field parallel to the applied field between the dots, ΔB_z , due to the magnetization of the gate structure, see Section 5.3, page 70. From the split EDSR signal (see Section 5.3.3, page 76) we know that for an external field $B_0 \approx 200$ mT the magnetic gates create a gradient $\Delta B_z \approx 25$ mT $\gg \Delta B_N^y \approx 4$ mT, so that this stable gradient will dominate the fluctuating gradient from the nuclei. This should not only result in faster rotations, corresponding to the indication of spin blockade after only 1 ns, but also allow coherent rotations between S and T_0 for up to ≈ 10 ns limited by the decoherence time due to the fluctuating nuclear field [116, 135]. This could explain the observed non-monotonicity of the blockade intensity with separation time, $\tau_{S'}$, for $B_0 = -200$ mT. More detailed measurements of the time dependence of singlet probability were attempted, but difficulties with the read-out circuit hindered a more systematic investigation.

Further measurements on the multi-electron double quantum dot were not performed due to instability of the device and the non-trivial spin states observed; emptying of the device from the measured region was not possible and the transitions showing spin-blockade were hard to find, hindering further exploration of the multi-electron regime for spin qubit operation.

Chapter 6

Conclusions and perspectives

6.1 Conclusions for the InAs nanowire studies

We have investigated two local gate geometries for creating tunable, local barriers in InAs nanowires and discussed the influence of device processing on device stability. We determined the height of the gate-induced barriers and found that local bottom and top gates are similar. Low-temperature measurements suggested a greater stability of the bottom gated QDs compared to the top gated; fabrication step order could lead to such a difference, in particular, early/late nanowire deposition for the top/bottom gated devices.

The width of the barrier strongly influences the tunneling current, but is not determined in our analysis of gate induced barriers; attempts to determine tunneling barrier width from the temperature dependence measurements showed that the noise floor in the measurements to a large extent dominated in the regions where thermal activation over the barrier was not dominating the tunneling current. Furthermore, to the extent the tunneling current was resolved, the available models incorporating a tunneling contribution either required knowledge of the electrochemical potential or were restricted to a parameter space other than that within which the tunneling current was resolved.

Device yield was increased by the use of gates overlapping the interface region between nanowire and contact electrode. Presumably, in-complete oxide removal or other sub-optimal processing steps can lead to a barrier between nanowire and contact; only some wires display this non-ohmic behavior despite following the same fabrication procedure for all devices. In addition to increasing device yield, the contact gates are generally useful as they allow for independent tuning of the nanowire/contact-coupling.

6.2 Conclusions for the GaAs/AlGaAs studies

We demonstrated a gate structure for a double double-quantum dot incorporating a cobalt micro-magnet on a shallow 2-DEG (57 nm below the surface) avoiding issues with alignment of micro-magnet with the dots. Simulations indicated that the field from the micro-magnet at the level of the dots had gradients between the dots compatible with EDSR based spin

manipulation and allowing individual manipulation of the dots. For all four dots occupations were tunable to the last electrons allowing tests operation as a two-electron spin qubit, however spin-blockade was only observed for one set of dots for reasons that are unknown.

EDSR mediated spin rotations were demonstrated, showing distinct resonance frequencies for the two dots, translating into a magnetic field gradient of ~ 25 mT from the micro-magnet between the dots. The EDSR mechanism could not be identified, since measurement of coherent oscillations was not attempted; thus the electron spin could have coupled to either the field gradient from the micro-magnet, the Overhauser field from the nuclei or the spin-orbit coupling.

Additionally, we investigated the multi-electron occupation regime of a double quantum dot with respect to operation as a two-electron spin qubit. Simple, alternating spin filling was not found, as Pauli spin blockade was not observed to occur with the regularity expected for such spin filling. Furthermore, measurement of the exchange splitting, J , indicated additional transitions lifting spin blockade.

It thus seems that there are some difference between the measured spin blocked transition in the multi-electron DQD and the $(1, 1)$ - $(0, 2)$ transition and furthermore the decoherence time, T_2^* , was roughly halved for the multi-electron system. The effect of the magnetic field gradients from the micro-magnet could play a role in the observed differences between the multi- and the few-electron double dots.

Measurements at additional occupancies and for additional devices are needed before anything can be concluded regarding the origin of the observed behavior for the multi-electron double dot.

6.3 Outlook

6.3.1 InAs nanowire studies

Alternative methods for barrier creation in nanowires are non-tunable barriers from heterostructure growth [209], crystal structure changes [156, 210] and chemical etching [211]. In the case of heterostructure barriers, the barrier height associated with an InP segment in an InAs nanowire was determined to 0.57 eV, comparable in magnitude to the ~ 0.1 – 0.2 eV found for the gate induced barriers described here. The magnitude of the heterostructure barrier is fixed by the materials used and the barrier can be atomically sharp and as thin as a few monolayers [16, 209]. This constitutes a way for obtaining multiple, identical barriers, or barriers that differ in a controlled way; however, tuning the grown barriers will not be possible, as they are determined by band offsets across and thickness of the heterostructure. In a device for a technological application, such characteristics could be desired, but for fundamental research the flexibility offered by the depletion gate approach is more desirable.

Regarding InAs nanowire device stability at low temperatures, an interesting alternative to ALD of HfO_2 is Si_3N_4 (or SiN_x) which can be deposited on predefined structures by sputtering [25, 212] as well as plasma enhanced chemical vapor deposition (PECVD) [144, 147, 213]. For instance, it has been used as low-noise gate dielectric in low temperature measurements on InAs nanowires [25, 113].

6.3.2 GaAs heterostructure studies

For the magnetic gate structure, the ability to induce coherent oscillations either via timed EDSR pulses or phase accumulation in the S - T_0 basis should be investigated. In addition, further measurements of the different magnetic gradients induced should be obtained; these could be used to compared to the predictions from the simulation and verify it's usefulness.

The origin of the split signal for the S - T_+ -crossing in the multi-electron regime could be investigated further by performing the same measurement for a device tuned to the (1,1)-(0,2) transition, asserting that the splitting is not present there with the micro-magnet magnetized.

In general, the study of the multi-electron dot should be revisited with a dot tuned to last electrons and the ability to control filling up to approx ten electrons per dot, in order to investigate the spin filling behavior more consistently and test effects of multi-electron occupation on qubit operation [187].

6.3.3 Perspectives for InAs nanowire and GaAs heterostructure spin qubits

There is no doubt that the InAs nanowire spin(-orbit) qubit [25] is currently lacking behind the spin qubits realized in GaAs 2-DEGs [98, 120, 121, 135, 137] in terms of coherence, demonstrated control and gates, see Section 2.5, page 30. However, instead of comparing directly, based on the current state of the field, one should rather look at the interesting perspectives for the future due to their material properties.

For the InAs nanowire the strong spin-orbit coupling opens up for strong coupling of the electron spin to the electric field of photons in a superconducting microwave cavity [138, 214, 215]. This point to the possibility of coupling distant qubits via microwave photons through “circuit quantum electrodynamics” (circuit QED) which has carried the development in superconducting qubits [216, 217]. Along the same lines, coupling of quantum dots in GaAs [218] (and carbon nanotubes [219]) to superconducting cavities has been demonstrated, but as the spin-orbit coupling is much weaker so would the spin-cavity coupling be, and only charge-cavity coupling is feasible.

Further, for nanowires the possibility to grow a wide range of heterostructures can be used to create optically active quantum dots of high quality that can be used quantum interface between electron spins and photons [14], with the perspective of the “flying qubit”

for transport between distant qubits.

It is still much to soon to pick a “winning” qubit and likely a large-scale quantum computer will not be realized using a single material system, but rather through a combination of a number of different systems, e.g. nuclear spins for storage, electron spins for manipulation via electrical signals and shuttling of qubits via photons or circuit QED.

Appendix A

Construction of a high frequency measurement setup

A prerequisite for the envisioned GaAs/AlGaAs double double-dot measurements at Marcus Lab at Harvard University was a dilution refrigerator with at least four high frequency lines for pulsing and a reflectometry read-out circuit. Therefore, the first task became modifying a KelvinoxMX 100 dilution refrigerator¹ to suit these needs.

The fridge was, when we got our hands on it, equipped with two RF lines and 32 DC lines. Hence we needed to add four coax lines, two for RF gate pulses and two for reflectometry read-out, along with the other components for the read-out circuit. The number of DC lines seemed sufficient, so we decided not to touch these. However, it soon turned out that we, in order to fit the additional RF lines and components for the tank circuits on the sample holder, would also need a new cold finger and a new sample holder printed circuit board (PCB), due to the limited space on the existing PCB sample holder and the tight fit of this in the existing cold finger. The reflectometry read-out circuit including demodulation was based on that described by David Reilly [189] with guidance from the descriptions in the theses of Edward Laird [130] and Christian Barthel [136], with the addition of a wideband low-noise amplifier (WB LNA).

This chapter starts with a general description of the considerations you make when adding/replacing wiring and components to a cryogenic system, and then describes the modifications that we made in relation to this. Also, the demodulation circuit outside the cryostat used to demodulate the reflectometry signal is described. Nice guidelines for cryostat wiring and filtering are [220] and [221], not to mention the theses by the former Marcus Lab graduate students Alexander Comstock Johnson [89] and Leonardo Di Carlo [222].

¹This was the ‘Old dil. fridge’, going by the log book name, although it was also called the ‘Stanford fridge’.

A.1 Cryogenic wiring

The electrical wiring in a cryogenic system faces the challenge of balancing the, often contradictory, requirements for low thermal conductivity and high electrical conductivity. Especially, for temperatures much below the Debye temperature, θ_D , where phonons are frozen out (usually for $T \lesssim 1$ K), electrons are responsible for the thermal conductivity as well as the electrical conductivity [221]. A low thermal conductivity of the leads will minimize the heat flow between stages of the refrigerator and help it obtain a low base temperature. On the other hand, the impedance of the leads must be sufficiently low to allow measurement of small resistance changes in a charge sensing QPC and not attenuate low frequency ac signals for lock-in measurements by acting as an RC filter and similarly for the leads for high frequency signals.

A.1.1 DC wiring

For DC and low frequency signals (< 1 kHz) simple, unshielded wire is sufficient, and using alloys like constantan or manganin from room temperature to the base temperature stage is standard, giving resistances on the order of 50–200 Ω and sufficient thermal insulation. Also, importantly, the resistance of the alloy wire is almost constant from 300 K–4 K (see Table 3.4 in ref. [220]). Below 1 K the increase in specific heat and resistance of constantan and manganin due to electron magnetic moments might warrant the use of PtW wire, where the changes are smaller and only start below 0.1 K. Alternatively, at temperatures below 0.1 K where heat leaks need to be kept at a minimum without sacrificing electrical conductivity, superconducting wire can be used at temperatures well below T_c , e.g. NbTi with $T_c \approx 9$ K [221]. In high magnetic fields superconductivity is generally suppressed and magneto resistance might make the wire resistance change calling for still different materials, e.g. NiCu alloys. Below the mixing chamber, where thermal coupling to the sample is desired, copper loom is used.

Thermal anchoring of the constantan (and other resistance) wires to different temperature stages is done by winding them tightly around copper posts fastened to the stages and securing them with GE varnish² or 1266 epoxy [220] or alternatively with dental floss, only, for easier reconfiguration [89]. In doing this one should be careful not to damage the thin insulating coating on the wires.

In addition to reduction of heat flow down the wires, the propagation of RF signals down the wires to the sample should be reduced by low pass filtering the lines both at the feedthrough panel to the fridge (the breakout box) and at low temperature as close to the sample as possible to attenuate noise picked up traveling down inside the fridge. Such filtering should be multi-stage with different stages having different cut-off frequencies matched such that the self-resonance frequency of the lowest cut-off frequency filter is higher than the cut-off

²note that the solvent in GE varnish softens formvar (now called Vinylec) insulation used on some types of wire making the insulation extra fragile

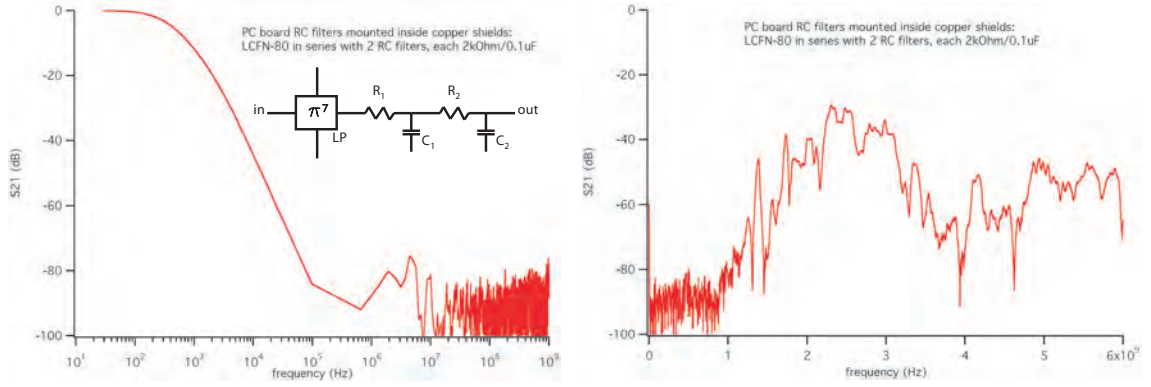


Figure A.1: (a) Transmission characteristics of three stage low pass filter mounted in copper shield. The insert shows the three stages, the first being a seven stage π -filter followed by two RC-filter stages. The shown transmission is for LP = 80 MHz-cut-off low pass filter, Mini-circuits LFCN-80; $R_1 = R_2 =$ Susumu2 k Ω , Digi-Key RR05P2.0KDCT-ND; $C_1 = C_2 =$ Murata 100 nF, Digi-Key 490-5322-1-ND. 3 dB point is around 300 Hz (b) Transmission for the same filter as in (a), for frequencies up to 6 GHz. Note that the transmission increases at frequencies > 1 GHz, but is maximally ≈ 30 dB.

frequency of the following stage and so on to ensure coverage.

A.1.2 High frequency wiring

For high frequency signals coaxial cable is needed to avoid attenuation of the signal by radiation and reflections and to minimize coupling to other leads in the refrigerator. Coaxial lines are designed to have a characteristic impedance, usually 50 Ω , between a center conductor and outer shield separated by a dielectric. Again, one has to strike a balance between little attenuation of signal and low thermal conductance when choosing materials for the center and outer conductors. An important effect to consider for high frequency signals is the skin effect, which describes the tendency for a high frequency ac current in a metal to run in a very thin region near the surface, the thickness given by

$$\delta_s = \sqrt{\frac{2}{\omega\mu\sigma}}, \quad (\text{A.1})$$

where ω is the angular frequency, μ is the magnetic permeability and σ is the conductivity [223]. For (non-magnetic) stainless steel the skin depth at a frequency of 1 GHz is $\approx 20 \mu\text{m}$ and for copper and silver $\approx 2 \mu\text{m}$. This effect greatly reduced the effective, current carrying, cross-section of a conductor, increasing the impedance with frequency. By covering a poor electrical conductor, with low thermal conductivity, *e.g.* stainless steel, with a thin layer of a good conductor, *e.g.* silver, you thereby gain a lot in high frequency electrical conductivity, since this is dominated by the thin surface layer, without increasing thermal conductivity significantly, since this is dominated by the bulk. As the signal is carried on the inner conductor, usually it is only necessary to coat this.

Thermal anchoring of coaxial cable is trickier than for unshielded wire; the thin outer shield of the coaxial cable is easily heat sunk through anchoring to the different stages,

Appendix A. Construction of a high frequency measurement setup

but the low thermal conductivity of the dielectric in the coax means that the thicker inner conductor, responsible for most of the heat load, is not thermalized by this anchoring. The trick currently used for the pulse lines delivering the fast signal to the gates, is thermalization through RF attenuators at each stage. The attenuators are basically voltage dividers, offering a low resistance path to ground ensuring thermalization, with a flat frequency response from DC–18 GHz (depending of the type and manufacturer). By choosing attenuation values (dB, referring to power division w. 3 dB equal to division by 2, 6 dB by 4, 10 dB by 10, 20 dB by 100, etc.) at each stage corresponding to the scaling factor of the temperature with respect to the previous stage, the thermal noise is properly attenuated; e.g. from 300 K to 4 K is approximately a factor of 100, so here a 20 dB attenuator would be suitable. One consideration here, is the cooling power of the different stage. Whereas the 4 K stage has more or less unlimited cooling power (at the expense of ^4He boil-off) and the pot and the still are usually also have some mW of cooling power [221], the cold plate and the mixing chamber have very limited cooling powers, especially is a low base temperature is required — the cooling power, $\dot{Q}_{\text{m/c}}$, of the mixing chamber scales with temperature, T , and ^3He flow, \dot{n}_3 [mol/s], as [221]

$$\dot{Q}_{\text{m/c}} = 84\dot{n}_3 T^2, \quad (\text{A.2})$$

for $T \lesssim 50 \text{ mK}^3$.

The use of attenuators in the pulse lines and the limited cooling powers of the different refrigerator stages also means that the dc signals for the gates are combined with the high frequency signals only after the mixing chamber using a bias tee. The bias tee used is a Marcus Lab invention that, despite its crude appearance, has a nice frequency response with -3 dB in transmission at $\simeq 20 \text{ GHz}$, see Fig. A.2. An attempt to improve shielding of the inner conductor by winding with Cu tape did not improve performance. The bias tee is simply a 100 nF surface mount device (SMD) capacitor⁴ soldered between two PCB mount SMA jacks, the length of the launcher pin filed down to fit the length of the capacitor, and a 5 k Ω SMD resistor soldered to the pin after the capacitor bringing on the dc line. The mounting legs of the PCB mount SMA jack are soldered pairwise to connect the ground of the two sides. A major nuisance of this bias tee is the fragility of the soldered junctions between the two SMA jacks, making it difficult to tighten both sides of the bias tee properly to the connecting coax without breaking the solder joints — and the space required for four of these in the tight space between mixing chamber and cold finger is also a limiting factor. Recently, both of these issues were solved by placing the bias tees, still in form of SMD resistors and capacitors, on the PCB sample holder, avoiding the PCB mount SMA connectors [224].

Since the cooling of the inner conductor in the coax for the pulse lines depends on

³The T^2 scaling of mixing chamber cooling power with temperature seems to hold at least for the temperature range $20 \text{ mK} \lesssim T \lesssim 200 \text{ mK}$, see Fig. 7.19 in reference [221]

⁴using a ceramic capacitor with C0G or NP0 spec. dielectric to minimize/avoid temperature dependence

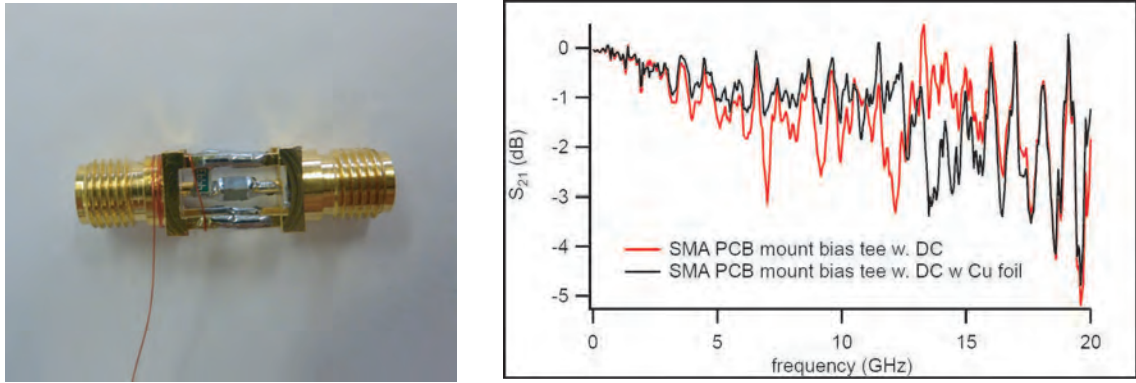


Figure A.2: (a) Picture of an assembled bias tee consisting of two SMA PCB mounts soft soldered at the mounting pins and with a 100 nF COG capacitor bridging the center pins and acting as a DC block. A 500 k Ω resistor is mounted ‘below’ the capacitor, up being signal source and down being sample, and acts as a AC block. (b) Transmission characteristic of an SMA bias tee identical to the one shown in (a). The 3dB point is \approx 20 GHz.

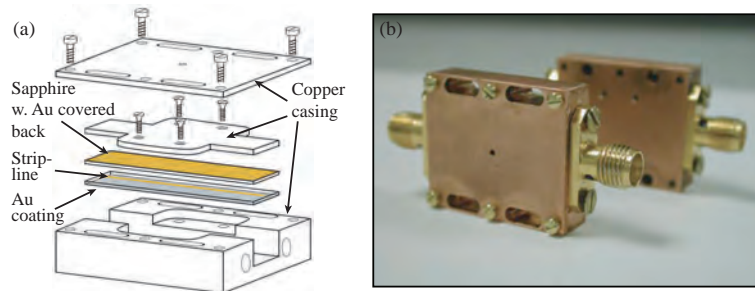


Figure A.3: Sapphire stripline heat sink for thermalization of inner conductor of coaxial cable while keeping 50 Ω matching. (a) Technical drawing of the assembly of the sapphire stripline heat sink. (b) Photograph of the assembled heat sink with SMA panel mount connectors. Adapted from[222].

attenuating the signal rather heavily, this approach is not applicable for the reflected signal line in the reflectometry read-out circuit as the signal reflected from the tank circuit is on the order of μ V [136]. Instead thermalization of the inner conductor relies on a breaking the coax by a section of sapphire stripline in a copper shielding with SMA connectors to keep the 50 Ω matching, see Fig. A.3. The copper box is thermally anchored to a stage in the fridge and cools the stripline through the sapphire dielectric, which has sufficient thermal conductivity to ensure thermalization [222]⁵. In addition the thermalization by the sapphire stripline, the directional coupler (ZX30-17-5+ from Mini-Circuits) provided a DC short to ground, which should also provide efficient thermalization.

of capacitance, though these are usually limited to capacitances of 1 pF to 100 nF

⁵Recently, Doug McClure and Patrick Gallagher experimented with replacing sapphire with diamond since the latter has much higher thermal conductivity.

Appendix A. Construction of a high frequency measurement setup

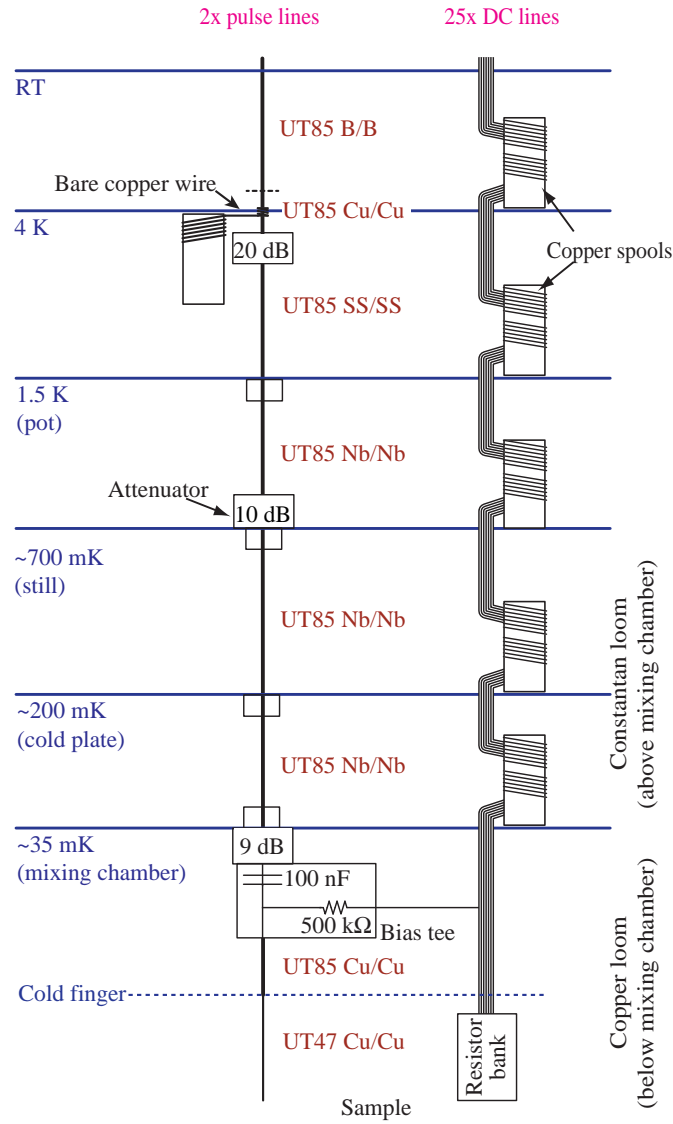


Figure A.4: Schematic of the high frequency pulse lines and DC lines in the Stanford dilution refrigerator (KelvinoxMX 100) prior to modifications. B=Berillium copper. SS=Stainless steel. Cu=Copper. Nb=Niobium.

A.1. Cryogenic wiring

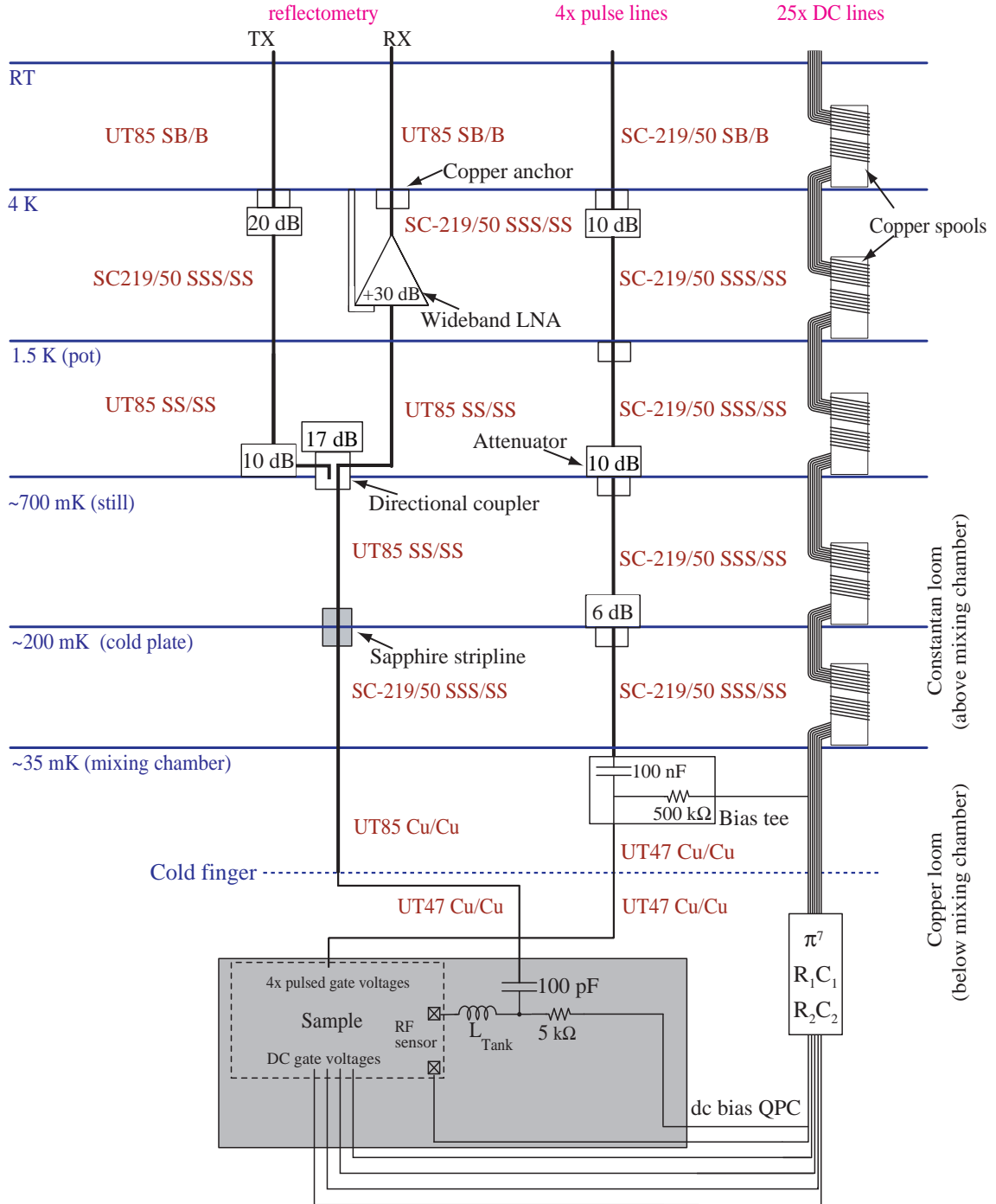


Figure A.5: Schematic of electronics inside the Stanford dilution refrigerator (KelvinMX 100) equipped with radio-frequency reflectometry read-out. The grey background indicates components mounted on the PC board. Key components are the home-built wideband low-noise amplifier; Home-built bias tees; directional coupler, Mini-circuits ZX30-17-5+. SB=silver plated beryllium copper. B=Berillium copper. SSS=Silver plated stainless steel. SS=Stainless steel. DC line filter: π^7 = seven stage LP π -filter 80 MHz (Mini-circuits LFCN-80), $R_1 = 1 \text{ k}\Omega$, $C_1 = 100 \text{ pF}$, $R_2 = 200 \Omega$, $C_2 = 100 \text{ pF}$.

Appendix A. Construction of a high frequency measurement setup

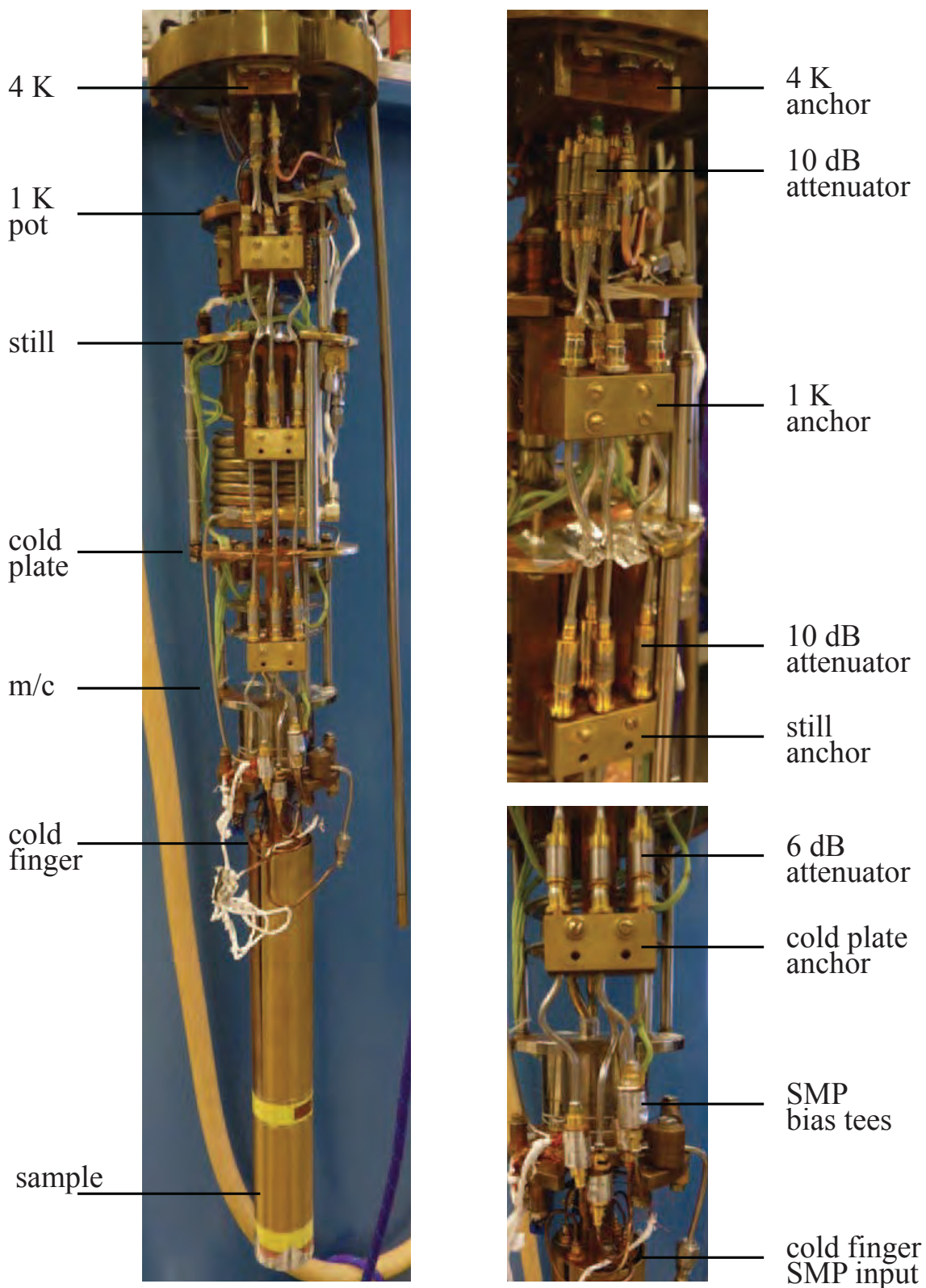


Figure A.6: Images showing the Stanford dilution fridge after modifications, with labels to indicate different elements.

Adding high frequency lines

The two existing RF pulse lines were mainly beryllium copper (B) and niobium (Nb), see Fig. A.4, and had -3 dB frequency of $\simeq 400$ MHz. In order to assure a low rise time of the applied square pulse we would like to improve the frequency bandwidth, but without increasing the heat load significantly, especially since the number of coaxial lines from RT would increase from two to six.

In order to fit four pulse lines and a reflectometry readout in the limited space available in the dilution insert it was necessary to find a smaller alternative to the SMA connectors, the de facto standard in cryogenic RF connectors. Based on availability of parts such as connectors, adaptors, attenuators and PCB mounts and a frequency range of DC to 40 GHz the SMP interface was chosen. Two unknown in this choice were the stability of the push-on/snap-on connector style employed in the SMP connectors and the low-temperature performance of the attenuators, as shorts to ground due to parts becoming superconducting at low temperature was a known issue with some brands of SMA attenuators [222], and not something that was specified by the manufacturer, but only be found out by trial and error (or learning from others experience). It turned out that the first attenuators we tried (Aeroflex/Inmet, see list of manufacturers page 109) did not short at the low temperatures in the cryostat. For the reflectometry circuit SMA connectors were used when space allowed.

To improve the frequency response the section from RT to 4 K was changed from beryllium copper/beryllium copper (B/B) inner/outer to silver plated beryllium copper/beryllium copper (SB/B) gaining a little in frequency response, see Table A.1, especially considering the long length of this stretch ($\simeq 1$ m), exploiting the cooling power of the 4 K stage. The remaining sections of the pulse lines from 4 K to mixing chamber were changed from niobium/niobium (Nb/Nb) and stainless steel/stainless steel (SS/SS) coax to silver plated stainless steel/stainless steel (SSS/SS) coax giving a large improvement in frequency response with minimal (if any) increase in heat load⁶, see table A.1. Below the mixing chamber good thermal contact to the sample is desired, so copper/copper (Cu/Cu) coax is used, going down from a outer diameter of 2.19 mm to 1.19 mm to increase the flexibility of the coax, making connecting to and disconnecting from the sample easier at the expense of some bandwidth. These choices resulted in frequency response with a -3 dB frequency of $\simeq 2$ GHz, see Fig. A.7.

For the reflectometry lines, the demands to the bandwidth are not so strict as the applied carrier frequencies are limited to around $\simeq 100$ -1000 MHz. Hence, the less expensive SS/SS was used instead of SSS/SS for the main parts between 4 K and mixing chamber, and again Cu/Cu was used below the mixing chamber.

⁶even though Nb has a critical temperature $T_c \simeq 9$ K the thermal conductivity of niobium stay higher than that of stainless steel down to $T \simeq 80$ mK according to data from table 3.21 in reference [221], although the thermal conductivity of both materials will depend strongly on purity and structure.

Appendix A. Construction of a high frequency measurement setup

Table A.1: Comparing the specifications for two types of coaxial cable (stainless steel and beryllium copper) to their silver plated counterparts. Coaxial cable from Coax Co., Ltd, Japan. Data taken from [225]

Part number		SC219/50-B-B	SC219/50-SB-B	SC219/50-SS-SS	SC219/50-SSS-SS	SC219/50-Nb-Nb
Outer conductor	Diameter [mm]	2.19	2.19	2.19	2.19	2.19
	Material	Beryllium copper	Beryllium copper	Stainless steel (SU304)	Stainless steel (SU304)	Niobium
Dielectric	Diameter [mm]	1.67	1.67	1.67	1.67	1.67
	Material	PTFE (Teflon)	PTFE	PTFE	PTFE	PTFE
Center conductor	Diameter [mm]	0.51	0.51	0.51	0.51	0.51
	Material	Beryllium copper	Silver plated beryllium copper	Stainless steel (SU304)	Silver plated stainless steel (SU304)	Niobium
Characteristic impedance [Ω]		50 ± 2	50 ± 2	50 ± 2	50 ± 2	50 ± 1.5
Capacitance (Average) [pF/m]		95.2	95.2	95.6	95.2	95.2
Attenuation [dB/m]	0.5 GHz	0.92	0.57	2.96	1.01	1.44
	1.0 GHz	1.32	0.81	4.19	1.44	2.05
	5 GHz	3.03	1.89	9.44	3.30	4.66
	10 GHz	4.39	2.76	13.5	4.75	6.68
	20 GHz	6.33	4.07	19.2	6.88	9.61

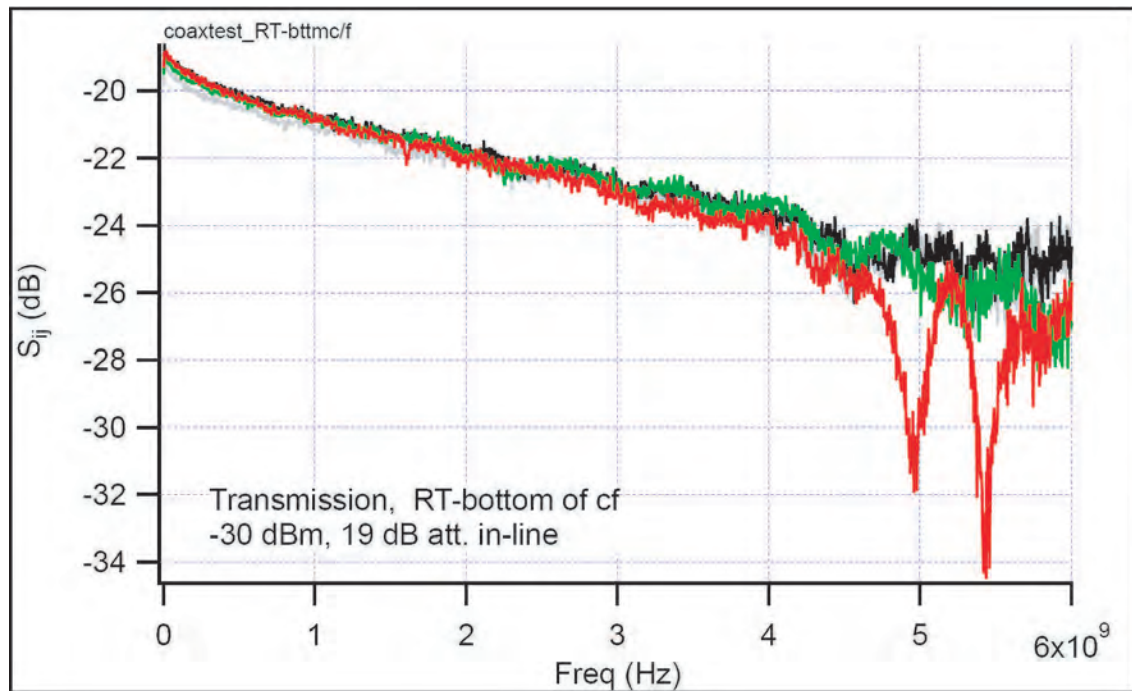


Figure A.7: Transmission characteristics of pulse lines after modifications to dilution refrigerator.

A.2 Reflectometry readout

The design of the reflectometry circuit was as stated earlier based on that described by David Reilly [189] with guidance from the descriptions in the theses of Edward Laird [130] and Christian Barthel [136], and the addition of a wideband low-noise amplifier (WB LNA) assembled by the author based on a design from reference [226] with a few modifications⁷.

Detecting changes in occupancy in quantum dots by charge sensing e.g. using a proximal QPC [188] is a very sensitive and non-invasive method for reading out charge states in double quantum dots. Operating such a sensor at high frequencies would further increase the signal-to-noise ratio, by lowering the $1/f$ noise contribution. In addition, having a high bandwidth of the read-out circuit would be an advantage as it gives a faster response time (lower rise time) of the sensing signal to the changes in the occupation. This would allow measurement of single tunneling events and system evolution [98, 227] rather than obtaining an ensemble average measurement, depending on the signal-to-noise ratio being high enough to allow a signal integration time shorter than the event timescale.

Obtaining a high bandwidth readout using unshielded wire and a QPC charge sensor is hindered by the large rise time (RC time) made up by the high sensor resistance ($\simeq 50$ - 100 k Ω) and the capacitance of the wire wound to several stages of the fridge being on the order of several hundred picofarads.

The trick in a reflectometry measurement is to measure the change in resistance of the charge sensor indirectly, by measuring the reflection of a resonant high frequency signal from an RCL circuit incorporating the QPC sensor [228], see Fig.A.8 (b). Reflection of the signal at the RCL circuit depends on the impedance mismatch between the signal source — a coaxial line designed to have $Z_0 = 50 \Omega$ — and the RCL circuit — being $Z = \frac{L}{RC}$ at resonance in the shown configuration — with the reflection coefficient for the voltage amplitude at the load given as [223]

$$\Gamma = \frac{Z - Z_0}{Z + Z_0}.$$

Changing the resistance, R , of the QPC will change the impedance⁸, $Z = \frac{L}{RC}$, of the RCL circuit leading to a change in the amplitude of the reflected signal, the signal being fully absorbed for impedance matching with $Z = Z_0 = 50 \Omega$, see Fig. A.8 (a).

The reflectometry measurement is most sensitive to change in QPC impedance around matching, which is achieved by choosing the appropriate inductance, L , as matching should be achieved around $R = 50$ - 100 k Ω where the QPC is most sensitive and the capacitance,

⁷Later, this home built WB LNA was replaced with one bought from the Weinreb group, see list of manufacturers, page 109

⁸This is the impedance of the shown RCL circuit at resonance frequency $\omega = \sqrt{\frac{1}{LC} - \frac{1}{(RC)^2}} \approx \frac{1}{\sqrt{LC}}$ for large R and C , determined by the input impedance $Z = i\omega L + \frac{1}{1/R + i\omega C} = \frac{1/R}{1/R^2 + \omega^2 C^2} + i\omega \left(L - \frac{C}{1/R^2 + \omega^2 C^2} \right)$ being purely real.

Appendix A. Construction of a high frequency measurement setup

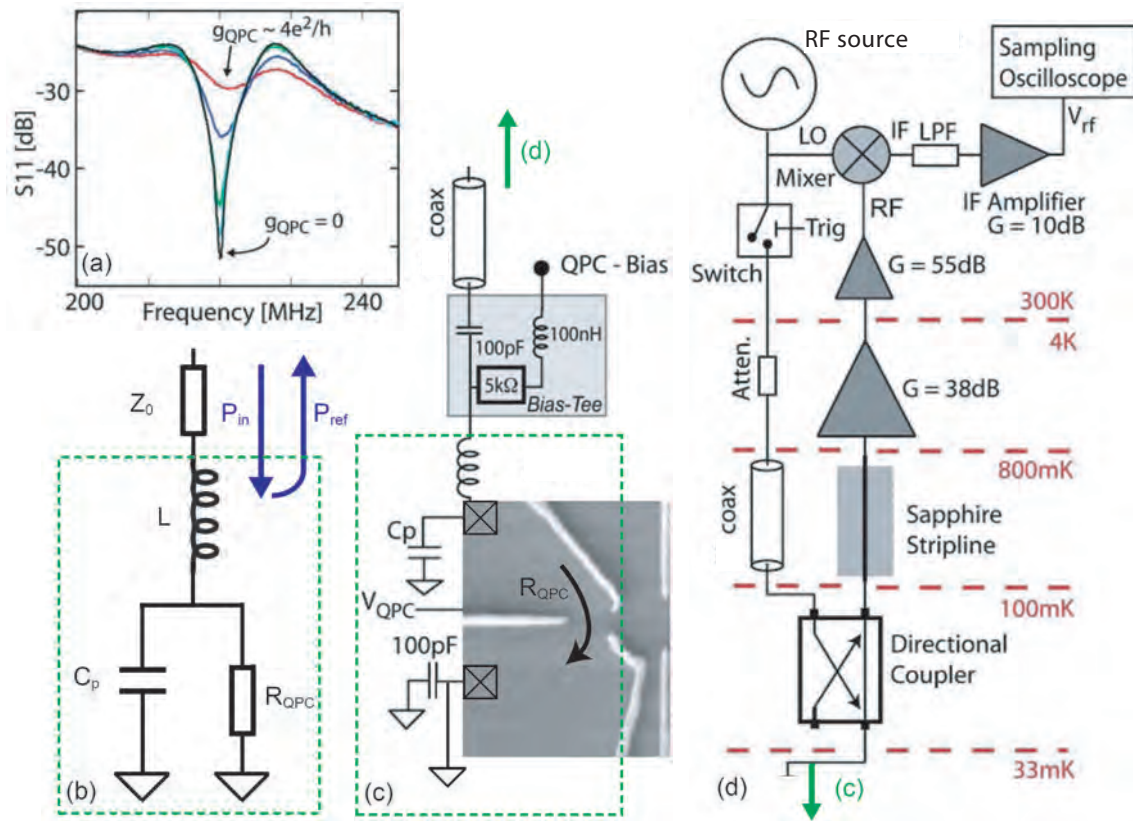


Figure A.8: Reflectometry. (a) A reflectometry measurement showing the dependence of the reflected signal power, $S_{11} \propto \Gamma^2$, from the tank circuit on the conductance ($1/R$) of the sensor QPC around the resonance frequency of the tank circuit, $\omega = 220$ MHz. (b) Schematic representation of the RCL tank circuit (green box), with a QPC as resistive element, R , and the capacitive element, C_p , dominated by parasitic capacitances of bond wire and bond pads. The capacitance and inductance, L , usually determine the resonance frequency and the resistance for matching of the input impedance, Z , to the source impedance, Z_0 ; varying R_{QPC} varies the amplitude of the signal reflected from the tank circuit. (c) Illustration of reflectometry circuit below the mixing chamber with bias-tee and tank circuit, the QPC sensor of the tank circuit show as SEM image of a device. Green dotted box corresponds to the box in (b), and the circuit from the mixing chamber and up is shown in panel (d), as indicated. (d) Simplified schematic illustration of the reflectometry read-out circuit in the fridge down to the mixing chamber and the demodulation circuit outside the fridge. Section below mixing chamber is shown in panel (c), as indicated by the green arrow. Adapted from [136].

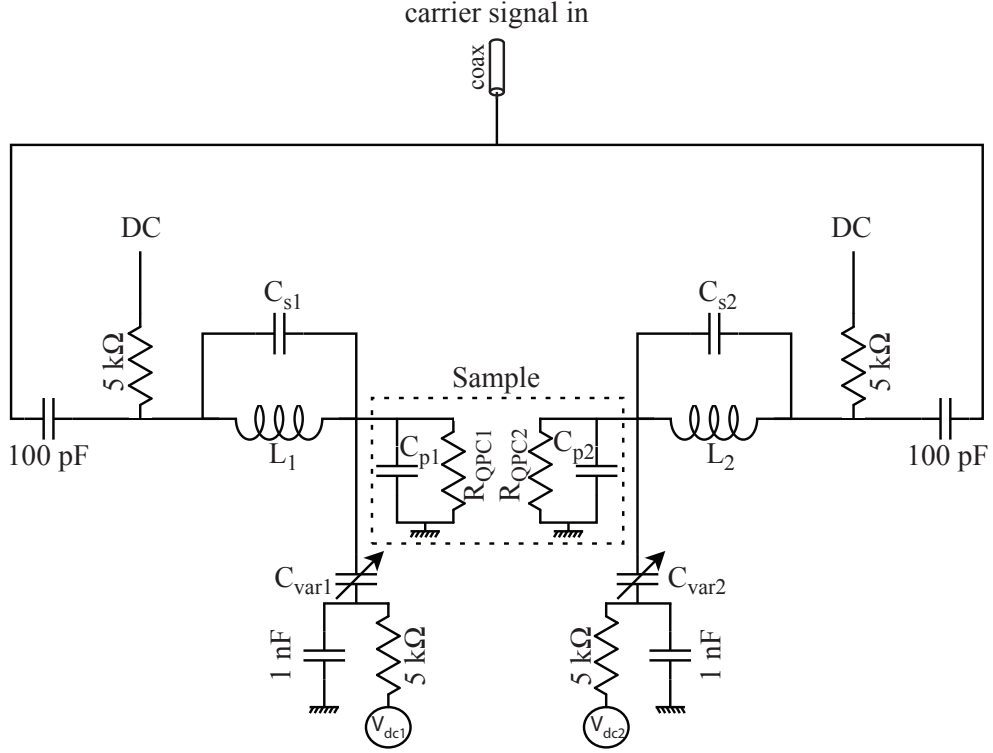


Figure A.9: Multiplexing. Schematic representation of multiplexing with parallel read-out from two tank circuits, each incorporating a sensor QPC. Note that the demodulation circuit outside the fridge also changes for multiplexed read-out [130].

$C \sim 1$ pF, is dominated by the stray capacitance of the bonding wire and ohmic contacts to ground, and thus not free parameters under our control. The resonance frequency of the tank circuit, $\omega \approx \frac{1}{\sqrt{LC}}$, is not crucial, as long as it is within the bandwidth of the reflectometry circuit including the cold amplifier (1-1500 MHz) and the directional coupler (5-2000 MHz); usually, we aimed for $\omega = 100$ -1000 MHz.

For multiplexed measurements [229], where two or more RF resonator circuits of different resonance frequency are measured simultaneously, the resonator circuits are simply connected in parallel to the same transmission line, see Fig. A.9. The carrier waves for each resonance frequency is only absorbed at the corresponding, impedance matching circuit. Assuming that the charge sensor QPC in each circuit is operated at approximately the same resistance, R , the ratio L/C is set by the requirement for 50Ω matching as $L/C = Z_0 R$. Obtaining different resonance frequencies by varying LC , keeping L/C constant, is hindered by C being dominated by stray capacitances not under our control. Therefore, variable capacitors, varactors, can be useful in tuning the capacitances, C , of the tank circuits, modulating the resonance frequencies in order to give well separated resonances.

Lately, reflectometry charge sensing of a double quantum dot via a LC resonator coupled to a gate electrode has been tested. Here, the reflected signal changes in response to the change in capacitance, C , of the resonator when charge occupancy changes in the

Appendix A. Construction of a high frequency measurement setup

double dot. This avoids the need for a dedicated charge sensor QPC, by coupling the resonator to one of the depletion gates.

The signal reflected from the tank circuit is fed to the amplifier at 4K with out attenuation, through a sapphire stripline and the in-out ports of the directional coupler. The introduction of a wide band cold amplifier has eased the task of tank circuit design, and especially multiplexing, significantly, as the frequency range within which the resonances should fall has been expanded form ~ 100 MHz [136] to ~ 1000 MHz (~ 1500 MHz), by changing to the home-built[226] (later changed to a amplifier bought from the Weinreb lab, CITLF1) wide band amplifier, see Fig. A.10.

Outside the cryostat the reflectometry signal from the fridge is demodulated in the circuit shown in Fig. A.11, performing homodyne detection of the signal at the carrier frequency, yielding a dc signal proportional to the amplitude of the reflected carrier signal. The signal from the RF source (HP8654B) is split by a directional coupler (ZEDC-15-2B) into local oscillator (LO, -2 dB) and carrier (IN, -15 dB). The carrier signal is attenuated and low- and high-pass filtered before entering the fridge. The reflected signal exiting from the fridge passes through high- and low-pass filters and is amplified (2 x ZFL-1000LN+) before being combined with the local oscillator signal in a mixer (ZP-3MH, 0.15-400 MHz) to yield a DC voltage. The phase of the local oscillator relative to the signal from the fridge is adjusted via a phase shifter (Pulsar SO-06-411, frequency range 150-280 MHz) to maximize the DC signal. Inside/outside DC blocks (Midwest Microwave DCB-3537-IO-SMA-02) on the input to and output from fridge suppress ground loops. The dc signal from the mixer is low pass filtered before being fed to a fast sampling oscilloscope (Agilent MSO8104A). Alternatively, data logging can be done by using a 8-lane PCI express waveform digitizing PC card (AlazarTech ATS9440, 4 channels, 125 MS/s, 14 bit resolution⁹, 1.6 GBs streaming rate to PC memory) mounted in the PC controlling the measurement.

A.3 Printed circuit board sample holders

Printed circuit boards (PCB) designed in house were used as sample holders, as they allow for easy interfacing between high frequency (RF) signals and sample by using PCB mount RF connectors to get the signal onto the board with minimum reflection. Both high frequency and DC lines run on the board to the sample bonding area, with the RF signals on the top and bottom layer; the width of the lines for the RF signals is designed to give 50Ω impedance with respect to the neighboring ground plane based on the thickness and the dielectric constant of the separating layer of Rogers 4003, see Fig. A.12 (a). The 25 DC lines run predominantly on the inner layers as these can make transitions between the layers without suffering reflection.

⁹this corresponds to a maximum acquisition rate of $4 \text{ channels} \times 125 \text{ MS}/(\text{s channel}) \times 2 \text{ B/S} = 1 \text{ GB/s}$

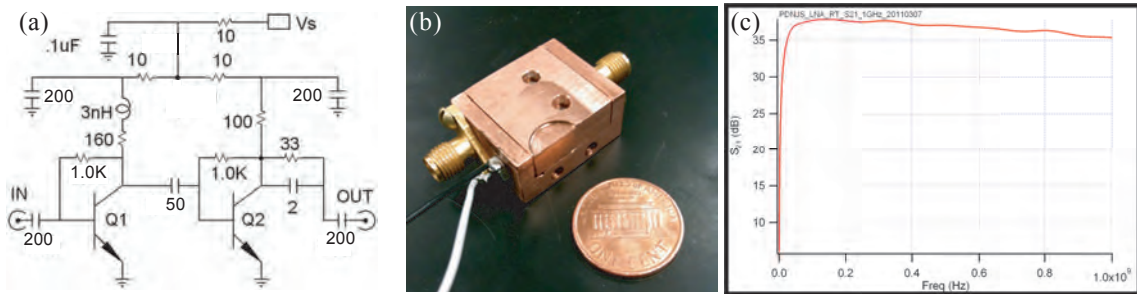


Figure A.10: Wide band low-noise amplifier. (a) Circuit diagram of the LNA. Capacitances are in pF and resistances in Ω . The two transistors, Q1 and Q2, are both NXP BFU725A transistors. All other components are standard surface mount components that are soldered to a Rogers 5880 0.762 mm thick PC board [226]. The layout of the circuit board and the choice of components have been optimized for impedance matching of input and output and a flat frequency response over a GHz range. (b) The assembled amplifier in a Cu shield that minimizes the input-to-output coupling. SMA connectors are shown, but the amplifier mounted in the Stanford fridge had SMP connectors. The pin beside the SMA connector is for transistor bias, V_S . (c) Performance of the assembled LNA at room temperature before mounting in fridge. Note the almost flat frequency response for frequencies $f \sim 50 - 1000$ MHz with amplification $S_{21} \approx 35$ dB. (a) Adapted from [226].

A.4 List of manufacturers

A.4.1 Attenuators

SMA m-f attenuators, DC-18 GHz, 2 W
 XMA Corp
 150 Dow Street
 Manchester, NH 03101
 +1 603-232-9088

part numbers:
 XMA-2080-6418-XX
 XX=dB value, e.g. 03 or 10

SMP m-f attenuators, DC-18 GHz, 2 W
 Aeroflex/Inmet
 300 Dino Drive
 Ann Arbor, MI 48103
 +1 734-426-5553

Appendix A. Construction of a high frequency measurement setup

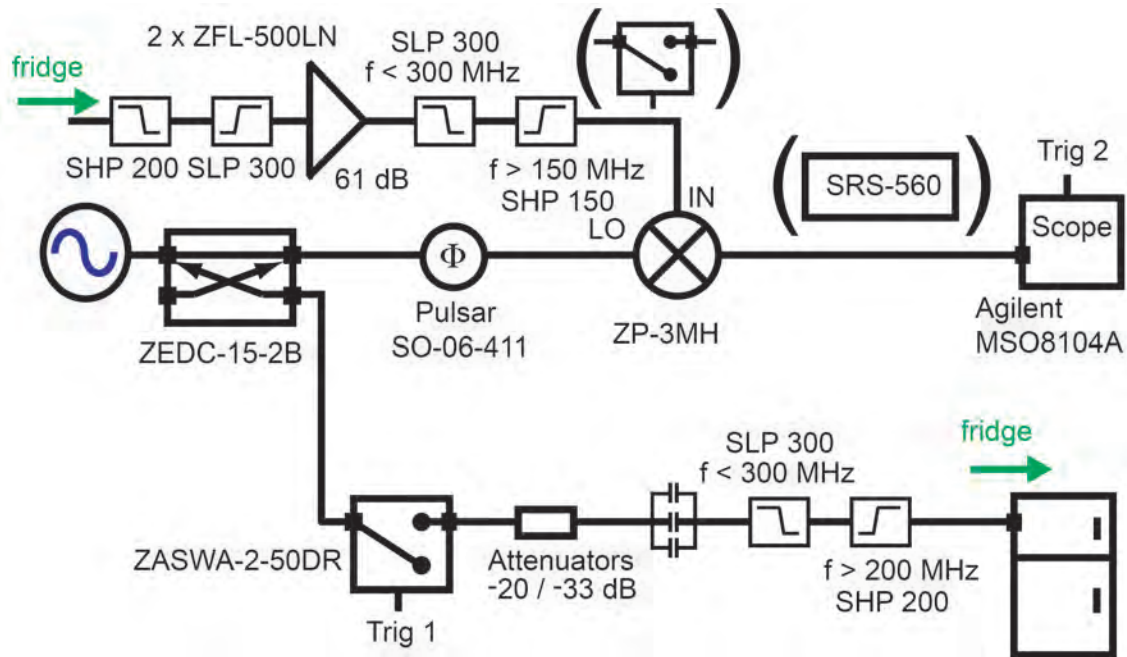


Figure A.11: Schematic representation of the setup outside the cryostat used to demodulate the reflectometry signal from the fridge. The signal from the RF source (HP8654B) is split by a directional coupler (ZEDC-15-2B) into local oscillator (LO, -2 dB) and carrier (IN, -15 dB). The carrier signal is attenuated and low- and high-pass filtered before entering the fridge. The reflected signal from the fridge passes through high- and low-pass filters and is amplified (2 x ZFL-1000LN+) before being combined with the local oscillator signal in a mixer (ZP-3MH, 0.15-400 MHz) to yield a DC voltage. The phase of the local oscillator relative to the signal from the fridge is adjusted via a phase shifter (Pulsar SO-06-411, frequency range 150-280 MHz) to maximize the DC signal. The dc signal is low pass filtered and logged by a fast sampling oscilloscope (Agilent MSO8104A). Inside/outside DC blocks (Midwest Microwave DCB-3537-IO-SMA-02) on both input to and output from fridge suppress ground loops. Adapted from [136].

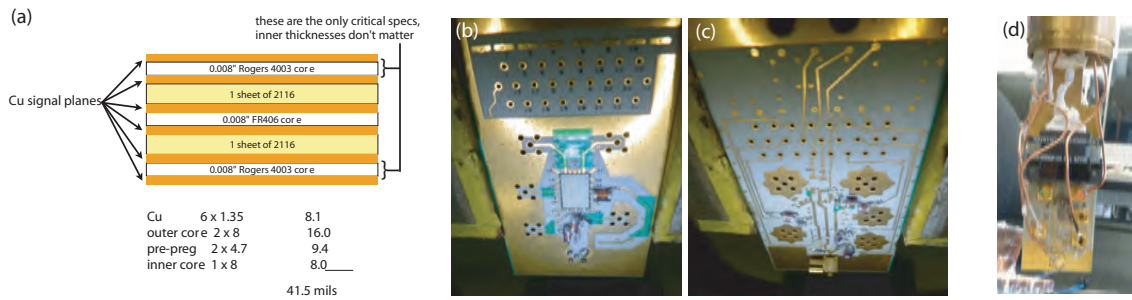


Figure A.12: Six layer printed circuit board. (a) Stack-up of the six-layer PCB designed by the author and Javad Shabani. The RF signals run on the top and bottom layer. The width of the lines for the RF signals is designed to give 50Ω impedance with respect to the neighboring ground plane based on the thickness and the dielectric constant of the separating layer of Rogers 4003. The 25 DC lines run predominantly on the inner layers. (b) Photograph of the sample side of the board. The 25 holes in the top of the image are the mounting holes for the micro D-sub connector from Cristek Interconnects, Inc. Below, five sets of unfilled mounting holes for PCB mount coax connectors can be seen. These five positions are for the pulse line RF signals. These lead to the sample mounting area in the center, bounded by a dark rectangle and bonding pads. (c) Photograph of the 'back side' of the PCB. In the bottom, a mounted MMCX type PCB mount coax connector is seen. This is for the carrier signal for the reflectometry read-out. In both (b) and (c) surface mount components for four tank circuits for the reflectometry read-out are visible. (d) Photograph of a PCB similar to the one in (b) and (c) mounted on the cold finger of the Stanford dilution refrigerator. Four pulse lines and the reflectometry line are connected to PCB mount connectors of the SMP type.

Appendix A. Construction of a high frequency measurement setup

part numbers:

18P-XX

Semi rigid coax

UT-85C (silver plated copper inner conductor and copper outer, 0,0865" outer diameter).

Microstock, Inc.

P.O. Box 91

West Point, PA 19486-0091

www.microstock-inc.com

SC-219/50-SB-B (silver plated beryllium copper center conductor and beryllium copper outer conductor, 2.19 mm (= 0.086") outer diameter.

SC-219/50-SSS-SS (silver plated stainless steel center conductor and stainless steel outer conductor, 2.19 mm (= 0.086") outer diameter.

Coax Co., Ltd.

2-31 Misuzugaoka, Aoba-ku, Yokohama-shi, Kanagawa

225-0016 Japan

<http://www.coax.co.jp/english/>

A.4.2 RF parts, passive electronics, SMC

Mini-circuits

<http://www.minicircuits.com>

Amplifiers

ZFL-1000LN+, 0.1 – 1000 MHz

ZFL-500LN+, 0.1 – 500 MHz

Low-pass filters

SLP-1.9+, 50 Ω , DC-1.9 MHz

SLP-1000+, 50 Ω , DC-900 MHz

High-pass filters

SHP-100+, 50 Ω , 90 – 2000 MHz

Mixers

ZP-3MH, 0.15 – 400 MHz

Directional couplers

ZEDC-15-2B, 50 Ω 1 – 1000 MHz

ZX30-17-5+, 50 Ω 5 – 2000 MHz

DC-blocks

BLK-18-S+, 50 Ω , 0.01 – 18 GHz

Susumu Co., Ltd. (SMC resistors)

<http://www.susumu.co.jp/english/>

SMC resistors showing constant resistance down to sub-kelvin temperatures: Susumu RR-series (C0G temperature coefficient).

Vishay Intertechnology, Inc. (SMC resistors and capacitors)

www.vishay.com/

SMC resistors useful at low temperatures: TNPW series (C0G temperature coefficient).

Non-magnetic SMC capacitors useful at low temperatures: VJ Non-Magnetic Series (C0G temperature coefficient).

Murata (SMC capacitors)

<http://www.murata.com>

SMC capacitors useful at low temperatures: Murata GRM and GCM series (C0G temperature coefficient).

American Technical Ceramics (ATC) (SMC capacitors)

<http://www.atceramics.com>

Non-magnetic SMC capacitors for low temperature use: atc 700B series (0.1 pF to 5100 pF).

Coilcraft, Inc. (SMC inductors)

<http://www.coilcraft.com>

EPCOS AG (SAW resonators)

<http://www.epcos.com>

Appendix A. Construction of a high frequency measurement setup

Varactor Tuning Diode
M/A-COM Technology Solutions
Part number: MA46600-134

Wideband low-noise amplifier
CITLF1, Cryogenic SiGe Low Noise Amplifier
RF frequency: 0.001-1.5 GHz
Weinreb Lab
California Institute of Technology
MS 136-93
1200 E. California Blvd
Pasadena, CA, 91125

Rosenberger (RF connectors)

Fairview (RF connectors)

Amphenol (RF connectors)

Tyco (RF connectors)

Emerson Network Power (=Midwest Microwave and Johnson) (RF connectors)

Pulsar (Phase shifters for demodulation)
Part number: SO-06-411

Cristek Interconnects, Inc.
Micro-D 25 pin plastic shell right angle PCB mount (PBR-1(or2)-025-054)

Glenair, Inc.
Nano-D connector, non-magnetic 51 pin R/A PCB mount

Part number: 891-008-51PS-BRT1T
Connector cable, nano-D connector
Part number: 891-002-25SA2-0A7-18J

A.4.3 Printed Circuit Boards

R & D Circuits Inc.
3601 South Clinton Avenue
South Plainfield, NJ 07080
<http://www.rdcircuits.com/>

Advanced Circuits
21101 E. 32nd Parkway
Aurora, CO 80011
<http://www.4pcb.com/>

Bibliography

- [1] Mark Bohr and Kaizad Mistry. Intel's Revolutionary 22 nm Transistor Technology. Technical report, 2011.
- [2] L. L. Sohn, L. P. Kouwenhoven, and G. Schön, editors. *Mesoscopic electron transport*. Kluwer, 1997.
- [3] Leo P. Kouwenhoven, Charles M. Marcus, Paul L. McEuen, Seigo Tarucha, Robert M. Westervelt, and Ned S. Wingreen. Electron transport in quantum dots. In L. L. Sohn, L. P. Kouwenhoven, and G. Schön, editors, *Mesoscopic Electron Transport*, volume 345, pages 105–214. Kluwer, 1997.
- [4] M. Kastner. The single-electron transistor. *Reviews of Modern Physics*, 64(3):849–858, July 1992.
- [5] Marc Monthieux and Vladimir L. Kuznetsov. Who should be given the credit for the discovery of carbon nanotubes? *Carbon*, 44(9):1621–1623, August 2006.
- [6] W. Han. Synthesis of Gallium Nitride Nanorods Through a Carbon Nanotube-Confined Reaction. *Science*, 277(5330):1287–1289, August 1997.
- [7] Jiangtao Hu, Teri Wang Odom, and Charles M. Lieber. Chemistry and Physics in One Dimension: Synthesis and Properties of Nanowires and Nanotubes. *Accounts of Chemical Research*, 32(5):435–445, May 1999.
- [8] HW Kroto, JR Heath, SC O'Brien, RF Curl, and RE Smalley. C60: Buckminsterfullerene. *Nature*, 318(6042):162, November 1985.
- [9] A. P. Alivisatos. Semiconductor clusters, nanocrystals, and quantum dots. *Science*, 271(5251):933–937, February 1996.
- [10] M H Huang, S Mao, H Feick, H Yan, Y Wu, H Kind, E Weber, R Russo, and P Yang. Room-temperature ultraviolet nanowire nanolasers. *Science*, 292(5523):1897–9, June 2001.
- [11] X Duan, Y Huang, Y Cui, J Wang, and C M Lieber. Indium phosphide nanowires as building blocks for nanoscale electronic and optoelectronic devices. *Nature*, 409(6816):66–9, January 2001.

Bibliography

- [12] Xiangfeng Duan, Yu Huang, Ritesh Agarwal, and Charles M Lieber. Single-nanowire electrically driven lasers. *Nature*, 421(6920):241–5, January 2003.
- [13] H Pettersson, J Trägårdh, A I Persson, L Landin, D Hessman, and L Samuelson. Infrared photodetectors in heterostructure nanowires. *Nano Letters*, 6(2):229–32, February 2006.
- [14] Maarten H M van Weert, Nika Akopian, Umberto Perinetti, Maarten P van Kouwen, Rienk E Algra, Marcel A Verheijen, Erik P A M Bakkers, Leo P Kouwenhoven, and Val Zwiller. Selective excitation and detection of spin states in a single nanowire quantum dot. *Nano Letters*, 9(5):1989–93, May 2009.
- [15] Hadas Shtrikman, Ronit Popovitz-Biro, Andrey Kretinin, Lothar Houben, Moty Heiblum, Małgorzata Bukała, Marta Galicka, Ryszard Buczek, and Perła Kacman. Method for suppression of stacking faults in Wurtzite III-V nanowires. *Nano Letters*, 9(4):1506–10, April 2009.
- [16] MT Björk, BJ Ohlsson, T Sass, AI Persson, C Thelander, MH Magnusson, K. Depfert, LR Wallenberg, and L. Samuelson. One-dimensional heterostructures in semiconductor nanowhiskers. *Applied Physics Letters*, 80(6):1058, 2002.
- [17] Mark S Gudiksen, Lincoln J Lauhon, Jianfang Wang, David C Smith, and Charles M Lieber. Growth of nanowire superlattice structures for nanoscale photonics and electronics. *Nature*, 415(6872):617–20, March 2002.
- [18] Lincoln J Lauhon, Mark S Gudiksen, Deli Wang, and Charles M Lieber. Epitaxial core-shell and core-multishell nanowire heterostructures. *Nature*, 420(6911):57–61, November 2002.
- [19] H-Y Li, O Wunnicke, M T Borgström, W G G Immink, M H M van Weert, M A Verheijen, and E P A M Bakkers. Remote p-doping of InAs nanowires. *Nano Letters*, 7(5):1144–8, May 2007.
- [20] Philippe Caroff, Maria E Messing, B Mattias Borg, Kimberly A Dick, Knut Deppert, and Lars-Erik Wernersson. InSb heterostructure nanowires: MOVPE growth under extreme lattice mismatch. *Nanotechnology*, 20(49):495606, December 2009.
- [21] C. Thelander, P. Agarwal, S. Brongersma, J. Eymery, L.F. Feiner, A. Forchel, M. Scheffler, W. Riess, B.J. Ohlsson, U. Gösele, and L. Samuelson. Nanowire-based one-dimensional electronics. *Materials Today*, 9(10):28–35, October 2006.
- [22] Yat Li, Fang Qian, Jie Xiang, and Charles M. Lieber. Nanowire electronic and optoelectronic devices. *Materials Today*, 9(10):18–27, 2006.
- [23] Tomás Palacios. Applied physics: Nanowire electronics comes of age. *Nature*, 481(7380):152–3, January 2012.

-
- [24] L Hofstetter, S Csonka, J Nygård, and C Schönenberger. Cooper pair splitter realized in a two-quantum-dot Y-junction. *Nature*, 461(7266):960–3, October 2009.
- [25] S Nadj-Perge, S M Frolov, E P A M Bakkers, and L P Kouwenhoven. Spin-orbit qubit in a semiconductor nanowire. *Nature*, 468(7327):1084–7, December 2010.
- [26] V. Mourik, K. Zuo, S. M. Frolov, S. R. Plissard, E. P. A. M. Bakkers, and L. P. Kouwenhoven. Signatures of Majorana fermions in hybrid superconductor-semiconductor nanowire devices. *Science*, 336(6084):1003–7, May 2012.
- [27] Supriyo Datta and B. Das. Electronic analog of the electro-optic modulator. *Applied Physics Letters*, 56(7):665–667, 1990.
- [28] Daniel Loss and D.P. DiVincenzo. Quantum computation with quantum dots. *Physical Review A*, 57(1):120, 1998.
- [29] S A Wolf, D D Awschalom, R A Buhrman, J M Daughton, S von Molnár, M L Roukes, A Y Chtchelkanova, and D M Treger. Spintronics: A Spin-Based Electronics Vision for the Future. *Science*, 294(5546):1488–95, November 2001.
- [30] I. Zutic and Jaroslav Fabian. Spintronics: Fundamentals and applications. *Reviews of Modern Physics*, 76(April):323–410, 2004.
- [31] Richard P. Feynman. Simulating physics with computers. *International Journal of Theoretical Physics*, 21(6-7):467–488, June 1982.
- [32] Michael A. Nielsen and Isaac L. Chuang. *Quantum Computation and Quantum Information*. Cambridge University Press, Cambridge, 10th anniv edition, 2010.
- [33] T D Ladd, F Jelezko, R Laflamme, Y Nakamura, C Monroe, and J L O’Brien. Quantum computers. *Nature*, 464(7285):45–53, March 2010.
- [34] Ari Mizel, Daniel Lidar, and Morgan Mitchell. Simple Proof of Equivalence between Adiabatic Quantum Computation and the Circuit Model. *Physical Review Letters*, 99(7):070502, August 2007.
- [35] Robert Raussendorf and Hans J. Briegel. A One-Way Quantum Computer. *Physical Review Letters*, 86(22):5188–5191, May 2001.
- [36] P Walther, K J Resch, T Rudolph, E Schenck, H Weinfurter, V Vedral, M Aspelmeyer, and A Zeilinger. Experimental one-way quantum computing. *Nature*, 434(7030):169–76, March 2005.
- [37] A.Yu. Kitaev. Fault-tolerant quantum computation by anyons. *Annals of Physics*, 303(1):2–30, January 2003.
- [38] Chetan Nayak, Ady Stern, Michael Freedman, and Sankar Das Sarma. Non-Abelian anyons and topological quantum computation. *Reviews of Modern Physics*, 80(3):1083–1159, September 2008.

Bibliography

- [39] Peter W. Shor. Polynomial-Time Algorithms for Prime Factorization and Discrete Logarithms on a Quantum Computer. *SIAM Journal on Computing*, 26(5):1484–1509, October 1997.
- [40] Lov K. Grover. A fast quantum mechanical algorithm for database search. In *Proceedings of the twenty-eighth annual ACM symposium on Theory of computing - STOC '96*, pages 212–219, New York, New York, USA, July 1996. ACM Press.
- [41] D. P. DiVincenzo. Quantum Computation. *Science*, 270(5234):255–261, October 1995.
- [42] David P. DiVincenzo. The Physical Implementation of Quantum Computation. *Fortschritte der Physik*, 48(9-11):771–783, September 2000.
- [43] Jeremy L O'Brien. Optical quantum computing. *Science*, 318(5856):1567–70, December 2007.
- [44] JI Cirac and P Zoller. Quantum computations with cold trapped ions. *Physical Review Letters*, 74(20):4091–4094, 1995.
- [45] H Häffner, C Roos, and R Blatt. Quantum computing with trapped ions. *Physics Reports*, 469(4):155–203, December 2008.
- [46] C. Monroe, D. Meekhof, B. King, W. Itano, and D. Wineland. Demonstration of a Fundamental Quantum Logic Gate. *Physical Review Letters*, 75(25):4714–4717, December 1995.
- [47] Gavin Brennen, Carlton Caves, Poul Jessen, and Ivan Deutsch. Quantum Logic Gates in Optical Lattices. *Physical Review Letters*, 82(5):1060, February 1999.
- [48] Q. Turchette, C. Hood, W. Lange, H. Mabuchi, and H. Kimble. Measurement of Conditional Phase Shifts for Quantum Logic. *Physical Review Letters*, 75(25):4710–4713, December 1995.
- [49] R Miller, T E Northup, K M Birnbaum, A Boca, A D Boozer, and H J Kimble. Trapped atoms in cavity QED: coupling quantized light and matter. *Journal of Physics B: Atomic, Molecular and Optical Physics*, 38(9):S551–S565, May 2005.
- [50] Neil A. Gershenfeld and Isaac L. Chuang. Bulk Spin-Resonance Quantum Computation. *Science*, 275(5298):350–356, January 1997.
- [51] D. G. Cory, A. F. Fahmy, and T. F. Havel. Ensemble quantum computing by NMR spectroscopy. *Proceedings of the National Academy of Sciences of the United States of America*, 94(5):1634–9, March 1997.
- [52] Isaac Chuang, Neil Gershenfeld, and Mark Kubinec. Experimental Implementation of Fast Quantum Searching. *Physical Review Letters*, 80(15):3408–3411, April 1998.

-
- [53] L. Vandersypen and I. Chuang. NMR techniques for quantum control and computation. *Reviews of Modern Physics*, 76(4):1037–1069, January 2005.
- [54] John Clarke and Frank K Wilhelm. Superconducting quantum bits. *Nature*, 453(7198):1031–42, June 2008.
- [55] J R Weber, W F Koehl, J B Varley, A Janotti, B B Buckley, C G Van de Walle, and D D Awschalom. Quantum computing with defects. *Proceedings of the National Academy of Sciences of the United States of America*, 107(19):8513–8, May 2010.
- [56] F. Jelezko, T. Gaebel, I. Popa, A. Gruber, and J. Wrachtrup. Observation of Coherent Oscillations in a Single Electron Spin. *Physical Review Letters*, 92(7):076401, February 2004.
- [57] William F Koehl, Bob B Buckley, F Joseph Heremans, Greg Calusine, and David D Awschalom. Room temperature coherent control of defect spin qubits in silicon carbide. *Nature*, 479(7371):84–7, November 2011.
- [58] B. E. Kane. A silicon-based nuclear spin quantum computer. *Nature*, 393(6681):133–137, May 1998.
- [59] Jarryd J. Pla, Kuan Y. Tan, Juan P. Dehollain, Wee H. Lim, John J. L. Morton, David N. Jamieson, Andrew S. Dzurak, and Andrea Morello. A single-atom electron spin qubit in silicon. *Nature*, 489(7417):541–545, September 2012.
- [60] S Bertaina, S Gambarelli, A Tkachuk, I N Kurkin, B Malkin, A Stepanov, and B Barbara. Rare-earth solid-state qubits. *Nature nanotechnology*, 2(1):39–42, January 2007.
- [61] Guido Burkard, Hans-Andreas Engel, and Daniel Loss. Spintronics and Quantum Dots for Quantum Computing and Quantum Communication. *Fortschritte der Physik*, 48(9-11):965–986, September 2000.
- [62] Ronald Hanson and David D Awschalom. Coherent manipulation of single spins in semiconductors. *Nature*, 453(7198):1043–9, June 2008.
- [63] Robert Andrzej Zak, Beat Röthlisberger, Stefano Chesi, and Daniel Loss. Quantum computing with electron spins in quantum dots. *La Rivista del Nuovo Cimento*, 33(7):345–399, 2010.
- [64] BM Maune, MG Borselli, B Huang, and TD Ladd. Coherent singlet-triplet oscillations in a silicon-based double quantum dot. *Nature*, 481(7381):344–347, 2012.
- [65] Yongjie Hu, Ferdinand Kuemmeth, Charles M Lieber, and Charles M Marcus. Hole spin relaxation in Ge-Si core-shell nanowire qubits. *Nature Nanotechnology*, 7(1):47–50, January 2012.

Bibliography

- [66] A. Imamoglu, D. D. Awschalom, G. Burkard, D. P. DiVincenzo, D. Loss, M. Sherwin, and A. Small. Quantum Information Processing Using Quantum Dot Spins and Cavity QED. *Physical Review Letters*, 83(20):4204–4207, November 1999.
- [67] Mete Atatüre, Jan Dreiser, Antonio Badolato, Alexander Högele, Khaled Karrai, and Atac Imamoglu. Quantum-dot spin-state preparation with near-unity fidelity. *Science*, 312(5773):551–3, April 2006.
- [68] Enrique Martín-López, Anthony Laing, Thomas Lawson, Roberto Alvarez, Xiao-Qi Zhou, and Jeremy L. O’Brien. Experimental realization of Shor’s quantum factoring algorithm using qubit recycling. *Nature Photonics*, 6(11):773–776, October 2012.
- [69] Peter Dahl Nissen. Characterization of InAs Nanowires by Electron Transport Measurements, 2009.
- [70] Martin Aagesen. *MBE grown nanorods and nanoplates*. PhD thesis, University of Copenhagen, 2007.
- [71] Peter Krogstrup. *Dynamical theory and experiments on GaAs nanowire growth for photovoltaic applications*. PhD thesis, University of Copenhagen, 2012.
- [72] Morten Hannibal Madsen. *Indium Arsenide Nanowires – Fabrication, Characterization, and Biological Applications*. PhD thesis, University of Copenhagen, 2012.
- [73] V. G. Dubrovskii, G. E. Cirlin, I. P. Soshnikov, A. A. Tonkikh, N. V. Sibirev, Y. B. Samsonenko, and V. M. Ustinov. Diffusion-induced growth of GaAs nanowiskers during molecular beam epitaxy: Theory and experiment. *Physical Review B*, 71(20):205325, 2005.
- [74] Frank Glas, Jean-Christophe Harmand, and Gilles Patriarche. Why Does Wurtzite Form in Nanowires of III-V Zinc Blende Semiconductors? *Physical Review Letters*, 99(14):3–6, October 2007.
- [75] M. Björk, a. Fuhrer, A. Hansen, M. Larsson, L. Fröberg, and L. Samuelson. Tunable effective g factor in InAs nanowire quantum dots. *Physical Review B*, 72(20):201307, November 2005.
- [76] Hannah J Joyce, Jennifer Wong-Leung, Qiang Gao, H Hoe Tan, and Chennupati Jagadish. Phase perfection in zinc Blende and Wurtzite III-V nanowires using basic growth parameters. *Nano letters*, 10(3):908–15, March 2010.
- [77] Stevan Nadj-Perge. *Single spins in semiconductor nanowires*. PhD thesis, Delft Technical University, 2010.
- [78] I Vurgaftman, JR Meyer, and LR Ram-Mohan. Band parameters for III–V compound semiconductors and their alloys. *Journal of Applied Physics*, 89(11):5815, 2001.

-
- [79] Z Zanolli, F Fuchs, J. Furthmüller, U. von Barth, and F Bechstedt. Model GW band structure of InAs and GaAs in the wurtzite phase. *Physical Review B*, 75(24):245121, 2007.
- [80] Zeila Zanolli and Ulf von Barth. All-electron study of InAs and GaAs wurtzite: structural and electronic properties. *Arxiv preprint arXiv:cond-mat/0610066v2*, 2007.
- [81] S. Bhargava, H.-R. Blank, V. Narayanamurti, and H. Kroemer. Fermi-level pinning position at the Au–InAs interface determined using ballistic electron emission microscopy. *Applied Physics Letters*, 70(6):759, February 1997.
- [82] Cedric Affentauschegg and Harry H Wieder. Properties of InAs/InAlAs heterostructures. *Semiconductor Science and Technology*, 16(8):708–714, August 2001.
- [83] M.T. Björk, Claes Thelander, A.E. Hansen, L.E. Jensen, M.W. Larsson, L.R. Wallenberg, and Lars Samuelson. Few-electron quantum dots in nanowires. *Nano Letters*, 4(9):1621–1625, 2004.
- [84] C.E. Pryor and M.E. Flatté. Landé g factors and orbital momentum quenching in semiconductor quantum dots. *Physical Review Letters*, 96(2):026804, 2006.
- [85] A. De and C.E. Pryor. Calculation of Landé g factors for III-V nanowhisker quantum dots and comparison with experiment. *Physical Review B*, 76(15):155321, 2007.
- [86] Till Andlauer, Richard Morschl, and Peter Vogl. Gauge-invariant discretization in multiband envelope function theory and g factors in nanowire dots. *Physical Review B*, 78(7):1–13, August 2008.
- [87] Charles Kittel. *Introduction to solid state physics*. Wiley, Hoboken NJ, 8. edition, 2005.
- [88] A. See, I. Pilgrim, B. Scannell, R. Montgomery, O. Klochan, A. Burke, M. Aagesen, P. Lindelof, I. Farrer, D. Ritchie, R. Taylor, A. Hamilton, and A. Micolich. Impact of Small-Angle Scattering on Ballistic Transport in Quantum Dots. *Physical Review Letters*, 108(19):196807, May 2012.
- [89] Alexander Comstock Johnson. *Charge Sensing and Spin Dynamics in GaAs Quantum Dots*. PhD thesis, Harvard University, 2005.
- [90] R. C. Ashoori. Electrons in artificial atoms. *Nature*, 379(6564):413–419, February 1996.
- [91] M. Bockrath. Single-Electron Transport in Ropes of Carbon Nanotubes. *Science*, 275(5308):1922–1925, March 1997.
- [92] J Salfi, S Roddaro, D Ercolani, L Sorba, I Savelyev, M Blumin, H E Ruda, and F Beltram. Electronic properties of quantum dot systems realized in semiconductor nanowires. *Semiconductor Science and Technology*, 25(2):024007, February 2010.

Bibliography

- [93] R. Hanson, J. R. Petta, S. Tarucha, and L. M. K. Vandersypen. Spins in few-electron quantum dots. *Reviews of Modern Physics*, 79(4):1217–1265, October 2007.
- [94] W. G. van der Wiel, S. De Franceschi, J. M. Elzerman, T. Fujisawa, S. Tarucha, and L. P. Kouwenhoven. Electron transport through double quantum dots. *Reviews of Modern Physics*, 75(1):1, 2003.
- [95] K Ono, DG Austing, Y Tokura, and S. Tarucha. Current rectification by Pauli exclusion in a weakly coupled double quantum dot system. *Science*, 297(5585):1313–1317, 2002.
- [96] Alexander Comstock Johnson, JR Petta, CM Marcus, MP Hanson, and AC Gossard. Singlet-triplet spin blockade and charge sensing in a few-electron double quantum dot. *Physical Review B*, 72(16):165308, 2005.
- [97] J. M. Taylor, H.-A. Engel, W. Dür, A. Yacoby, C. M. Marcus, P. Zoller, and M. D. Lukin. Fault-tolerant architecture for quantum computation using electrically controlled semiconductor spins. *Nature Physics*, 1(3):177–183, December 2005.
- [98] M. D. Shulman, O. E. Dial, S. P. Harvey, H. Bluhm, V. Umansky, and A. Yacoby. Demonstration of Entanglement of Electrostatically Coupled Singlet-Triplet Qubits. *Science*, 336(6078):202–205, April 2012.
- [99] Frank Henricus Louis Koppens. *Coherence and control of a single electron spin in a quantum dot*. PhD thesis, Delft Technical University, 2007.
- [100] J. Medford, Ł. Cywiński, C. Barthel, C. M. Marcus, M. P. Hanson, and A. C. Gossard. Scaling of Dynamical Decoupling for Spin Qubits. *Physical Review Letters*, 108(8):086802, February 2012.
- [101] FHL Koppens, C Buizert, KJ Tielrooij, IT Vink, KC Nowack, T Meunier, LP Kouwenhoven, and LMK Vandersypen. Driven coherent oscillations of a single electron spin in a quantum dot. *Nature*, 442:766, 2006.
- [102] EA Laird, C Barthel, EI Rashba, CM Marcus, MP Hanson, and AC Gossard. Hyperfine-mediated gate-driven electron spin resonance. *Physical Review Letters*, 99(24):246601, 2007.
- [103] FHL Koppens, JA Folk, JM Elzerman, R. Hanson, LH van Beveren, IT Vink, H.P. Tranitz, W. Wegscheider, L.P. Kouwenhoven, and LMK Vandersypen. Control and detection of singlet-triplet mixing in a random nuclear field. *Science*, 309(5739):1346, 2005.
- [104] F. H. L. Koppens, C. Buizert, I. T. Vink, K. C. Nowack, T. Meunier, L. P. Kouwenhoven, and L. M. K. Vandersypen. Detection of single electron spin resonance in a double quantum dot. *Journal of Applied Physics*, 101(8):081706, April 2007.

-
- [105] Lorenza Viola and Seth Lloyd. Dynamical suppression of decoherence in two-state quantum systems. *Physical Review A*, 58(4):2733–2744, October 1998.
- [106] Richard Liboff. *Introductory quantum mechanics*. Addison-Wesley, San Francisco, 4th ed. edition, 2003.
- [107] R. J. Elliott. Theory of the Effect of Spin-Orbit Coupling on Magnetic Resonance in Some Semiconductors. *Physical Review*, 96(2):266–279, October 1954.
- [108] G. Dresselhaus. Spin-Orbit Coupling Effects in Zinc Blende Structures. *Physical Review*, 100(2):580–586, October 1955.
- [109] Yu A Bychkov and E I Rashba. Oscillatory effects and the magnetic susceptibility of carriers in inversion layers. *Journal of Physics C: Solid State Physics*, 17(33):6039–6045, November 1984.
- [110] M. I. D’Yakonov and V. I. Perel’. Spin Orientation of Electrons Associated with the Interband Absorption of Light in Semiconductors. *Soviet Journal of Experimental and Theoretical Physics*, 33(5):1053, 1971.
- [111] K C Nowack, F H L Koppens, Yuli V Nazarov, and L M K Vandersypen. Coherent control of a single electron spin with electric fields. *Science*, 318(5855):1430–3, November 2007.
- [112] AE Hansen, MT Björk, C Fasth, C Thelander, and L Samuelson. Spin relaxation in InAs nanowires studied by tunable weak antilocalization. *Physical Review B*, 71(20):205328, 2005.
- [113] C. Fasth, A. Fuhrer, L. Samuelson, Vitaly N. Golovach, and Daniel Loss. Direct Measurement of the Spin-Orbit Interaction in a Two-Electron InAs Nanowire Quantum Dot. *Physical Review Letters*, 98(26):266801, June 2007.
- [114] J. Danon and Yu. V. Nazarov. Pauli spin blockade in the presence of strong spin-orbit coupling. *Physical Review B*, 80(4):041301, July 2009.
- [115] S. Nadj-Perge, S. M. Frolov, J. W. W. van Tilburg, J. Danon, Yu. V. Nazarov, R. Algra, E. P. A. M. Bakkers, and L. P. Kouwenhoven. Disentangling the effects of spin-orbit and hyperfine interactions on spin blockade. *Physical Review B*, 81(20):201305(R), May 2010.
- [116] J R Petta, Alexander Comstock Johnson, JM Taylor, EA Laird, A. Yacoby, MD Lukin, CM Marcus, MP Hanson, and AC Gossard. Coherent manipulation of coupled electron spins in semiconductor quantum dots. *Science*, 309(5744):2180, September 2005.
- [117] O. E. Dial, M. D. Shulman, S. P. Harvey, H. Bluhm, V. Umansky, and A. Yacoby. Electrometry Using Coherent Exchange Oscillations in a Singlet-Triplet-Qubit. *arXiv:1208.2023v4*, August 2012.

Bibliography

- [118] E. Laird, J. Taylor, D. DiVincenzo, C. Marcus, M. Hanson, and A. Gossard. Coherent spin manipulation in an exchange-only qubit. *Physical Review B*, 82(7):075403, August 2010.
- [119] L. Gaudreau, G. Granger, A. Kam, G. C. Aers, S. A. Studenikin, P. Zawadzki, M. Pioro-Ladrière, Z. R. Wasilewski, and A. S. Sachrajda. Coherent control of three-spin states in a triple quantum dot. *Nature Physics*, 8(1):54–58, November 2011.
- [120] R. Brunner, Y.-S. Shin, T. Obata, M. Pioro-Ladrière, T. Kubo, K. Yoshida, T. Taniyama, Y. Tokura, and S. Tarucha. Two-Qubit Gate of Combined Single-Spin Rotation and Interdot Spin Exchange in a Double Quantum Dot. *Physical Review Letters*, 107(14):146801, September 2011.
- [121] K C Nowack, M Shafiei, M Laforest, G E D K Prawiroatmodjo, L R Schreiber, C Reichl, W Wegscheider, and L M K Vandersypen. Single-shot correlations and two-qubit gate of solid-state spins. *Science*, 333(6047):1269–72, September 2011.
- [122] I. van Weperen, B. Armstrong, E. Laird, J. Medford, C. Marcus, M. Hanson, and A. Gossard. Charge-State Conditional Operation of a Spin Qubit. *Physical Review Letters*, 107(3):030506, July 2011.
- [123] D P DiVincenzo, D Bacon, J Kempe, G Burkard, and K B Whaley. Universal quantum computation with the exchange interaction. *Nature*, 408(6810):339–42, November 2000.
- [124] M. Pioro-Ladrière, John Davies, A. Long, A. Sachrajda, Louis Gaudreau, P. Zawadzki, J. Lapointe, J. Gupta, Z. Wasilewski, and S. Studenikin. Origin of switching noise in GaAs/Al_xGa_{1-x}As lateral gated devices. *Physical Review B*, 72(11):115331, September 2005.
- [125] Christo Buizert, Frank H. L. Koppens, Michel Pioro-Ladrière, Hans-Peter Tranitz, Ivo T. Vink, Seigo Tarucha, Werner Wegscheider, and Lieven M. K. Vandersypen. In Situ Reduction of Charge Noise in GaAs/Al_xGa_{1-x}As Schottky-Gated Devices. *Physical Review Letters*, 101(22):226603, November 2008.
- [126] Joe Salfi, Nicola Paradiso, Stefano Roddaro, Stefan Heun, Selvakumar V Nair, Igor G Savelyev, Marina Blumin, Fabio Beltram, and Harry E Ruda. Probing the gate-voltage-dependent surface potential of individual InAs nanowires using random telegraph signals. *ACS nano*, 5(3):2191–9, March 2011.
- [127] M. R. Sakr and X. P. A. Gao. Temperature dependence of the low frequency noise in indium arsenide nanowire transistors. *Applied Physics Letters*, 93(20):203503, 2008.
- [128] Jeremy Levy. Universal Quantum Computation with Spin-1/2 Pairs and Heisenberg Exchange. *Physical Review Letters*, 89(14):147902, September 2002.
- [129] A Abragam. *The principles of nuclear magnetism*. Clarendon Press, Oxford, 1961.

-
- [130] Edward Alexander Laird. *Electrical control of quantum dot spin qubits*. PhD thesis, Harvard University, 2009.
- [131] M Pioro-Ladrière, T Obata, Y Tokura, Y.-S. Shin, T Kubo, K Yoshida, T Taniyama, and S. Tarucha. Electrically driven single-electron spin resonance in a slanting Zeeman field. *Nature Physics*, 4(10):776–779, 2008.
- [132] Toshiaki Obata, Michel Pioro-Ladrière, Yasuhiro Tokura, Yun-sok Shin, Toshihiro Kubo, Katsuhara Yoshida, Tomoyasu Taniyama, and Seigo Tarucha. Coherent Manipulation of Individual Electron Spin in a Double Quantum Dot Integrated with a Micro-Magnet. *Physical Review B*, 81(08):085317, 2010.
- [133] J. M. Taylor, J. R. Petta, A. C. Johnson, A. Yacoby, C. M. Marcus, and M. D. Lukin. Relaxation, dephasing, and quantum control of electron spins in double quantum dots. *Physical Review B*, 76(3):035315, July 2007.
- [134] M. Pioro-Ladrière, Y. Tokura, T. Obata, T. Kubo, and S. Tarucha. Micromagnets for coherent control of spin-charge qubit in lateral quantum dots. *Applied Physics Letters*, 90(2):024105, 2007.
- [135] Sandra Foletti, Hendrik Bluhm, Diana Mahalu, Vladimir Umansky, and Amir Yacoby. Universal quantum control of two-electron spin quantum bits using dynamic nuclear polarization. *Nature Physics*, 5(12):903–908, 2009.
- [136] Christian Barthel. *Control and fast Measurement of Spin Qubits*. PhD thesis, Harvard University, 2010.
- [137] Hendrik Bluhm, Sandra Foletti, Izhar Neder, Mark Rudner, Diana Mahalu, Vladimir Umansky, and Amir Yacoby. Dephasing time of GaAs electron-spin qubits coupled to a nuclear bath exceeding 200 μ s. *Nature Physics*, 7(2):109–113, December 2011.
- [138] K. D. Petersson, L. W. McFaul, M. D. Schroer, M. Jung, J. M. Taylor, A. A. Houck, and J. R. Petta. Circuit quantum electrodynamics with a spin qubit. *Nature*, 490(7420):380–3, May 2012.
- [139] D B Suyatin, C Thelander, M T Björk, I Maximov, and L Samuelson. Sulfur passivation for ohmic contact formation to InAs nanowires. *Nanotechnology*, 18(10):105307, March 2007.
- [140] VN Bessolov and MV Lebedev. Chalcogenide passivation of III–V semiconductor surfaces. *Semiconductors*, 32(11):1141–1156, 1998.
- [141] D.Y. Petrovykh, M.J. Yang, and L.J. Whitman. Chemical and electronic properties of sulfur-passivated InAs surfaces. *Surface Science*, 523(3):231–240, January 2003.
- [142] Andrey V Kretinin, Ronit Popovitz-Biro, Diana Mahalu, and Hadas Shtrikman. Multimode Fabry-Perot conductance oscillations in suspended stacking-faults-free InAs nanowires. *Nano Letters*, 10(9):3439–45, September 2010.

Bibliography

- [143] Juriaan Wilhelmus Wouter van Tilburg. *Electron Spins in Nanowire Quantum Dots*. PhD thesis, Technische Universiteit Delft, July 2010.
- [144] Michael D Schroer. *Charge and Spin Manipulation in InAs Nanowires*. PhD thesis, Stanford University, 2012.
- [145] C Thelander, MT Björk, MW Larsson, AE Hansen, LR Wallenberg, and L Samuelson. Electron transport in InAs nanowires and heterostructure nanowire devices. *Solid State Communications*, 131(9-10):573–579, 2004.
- [146] C Thelander, K A Dick, M T Borgström, L E Fröberg, P Caroff, H A Nilsson, and L Samuelson. The electrical and structural properties of n-type InAs nanowires grown from metal-organic precursors. *Nanotechnology*, 21(20):205703, May 2010.
- [147] Carina Fasth, Andreas Fuhrer, M.T. Björk, and Lars Samuelson. Tunable double quantum dots in InAs nanowires defined by local gate electrodes. *Nano Letters*, 5(7):1487–1490, 2005.
- [148] Yong-Joo Doh, Jordan A van Dam, Aarnoud L Roest, Erik P A M Bakkers, Leo P Kouwenhoven, and Silvano De Franceschi. Tunable supercurrent through semiconductor nanowires. *Science*, 309(5732):272–5, July 2005.
- [149] Marc Scheffler, Stevan Nadj-Perge, Leo P. Kouwenhoven, Magnus T. Borgström, and Erik P. A. M. Bakkers. Diameter-dependent conductance of InAs nanowires. *Journal of Applied Physics*, 106(12):124303, 2009.
- [150] Thomas Sand Jespersen, Martin Aagesen, Claus Sørensen, Poul Erik Lindelof, and Jesper Nygård. Kondo physics in tunable semiconductor nanowire quantum dots. *Physical Review B*, 74(23):233304, December 2006.
- [151] Peter Dahl Nissen, Thomas Sand Jespersen, Kasper Grove-Rasmussen, Attila Márton, Shivendra Upadhyay, Morten Hannibal Madsen, Szabolcs Csonka, and Jesper Nygård. Comparison of gate geometries for tunable, local barriers in InAs nanowires. *Journal of Applied Physics*, 112(8):084323, 2012.
- [152] Andreas Pfund, Ivan Shorubalko, Renaud Leturcq, Magnus T. Borgström, Fabian Gramm, Elisabeth Müller, and Klaus Ensslin. Fabrication of Semiconductor Nanowires for Electronic Transport Measurements. *CHIMIA International Journal for Chemistry*, 60(11):729–734, November 2006.
- [153] I Shorubalko, A Pfund, R Leturcq, M T Borgström, F Gramm, E Müller, E Gini, and K Ensslin. Tunable few-electron quantum dots in InAs nanowires. *Nanotechnology*, 18(4):044014, January 2007.
- [154] S Csonka, L Hofstetter, F Freitag, S Oberholzer, C Schönenberger, T S Jespersen, M Aagesen, and J Nygård. Giant fluctuations and gate control of the g-factor in InAs nanowire quantum dots. *Nano Letters*, 8(11):3932–5, November 2008.

-
- [155] L Hofstetter, S Csonka, J Nygård, and C Schönenberger. Supplementary information: Cooper pair splitter realized in a two-quantum-dot Y-junction. *Nature*, 461(7266):960–3, October 2009.
- [156] M D Schroer and J R Petta. Correlating the nanostructure and electronic properties of InAs nanowires. *Nano Letters*, 10(5):1618–22, May 2010.
- [157] Shadi A. Dayeh, Darija Susac, Karen L. Kavanagh, Edward T. Yu, and Deli Wang. Structural and Room-Temperature Transport Properties of Zinc Blende and Wurtzite InAs Nanowires. *Advanced Functional Materials*, 19(13):2102–2108, July 2009.
- [158] X. Zhou, S. A. Dayeh, D. Aplin, D. Wang, and E. T. Yu. Direct observation of ballistic and drift carrier transport regimes in InAs nanowires. *Applied Physics Letters*, 89(5):053113, August 2006.
- [159] Alexandra C Ford, Johnny C Ho, Yu-Lun Chueh, Yu-Chih Tseng, Zhiyong Fan, Jing Guo, Jeffrey Bokor, and Ali Javey. Diameter-dependent electron mobility of InAs nanowires. *Nano Letters*, 9(1):360–365, 2009.
- [160] Alexandra C Ford, S Bala Kumar, Rehan Kapadia, Jing Guo, and Ali Javey. Observation of degenerate one-dimensional sub-bands in cylindrical InAs nanowires. *Nano Letters*, 12(3):1340–3, March 2012.
- [161] Dong Liang, Mohammed R Sakr, and Xuan P A Gao. One-dimensional weak localization of electrons in a single InAs nanowire. *Nano Letters*, 9(4):1709–12, April 2009.
- [162] Sajal Dhara, Hari Solanki, Vibhor Singh, Arjun Narayanan, Prajakta Chaudhari, Mahesh Gokhale, Arnab Bhattacharya, and Mandar Deshmukh. Magnetotransport properties of individual InAs nanowires. *Physical Review B*, 79(12):121311, March 2009.
- [163] Sajal Dhara, Shamashis Sengupta, Hari S. Solanki, Arvind Maurya, Arvind Pavan R., M. R. Gokhale, Arnab Bhattacharya, and Mandar M. Deshmukh. Facile fabrication of lateral nanowire wrap-gate devices with improved performance. *Applied Physics Letters*, 99(17):173101, 2011.
- [164] Anindya Das, Yuval Ronen, Yonatan Most, Yuval Oreg, Moty Heiblum, and Hadas Shtrikman. Evidence of Majorana fermions in an Al-InAs nanowire topological superconductor. *Arxiv preprint arXiv:1205.7073v2*, 2012.
- [165] Stefano Roddaro, Andrea Pescaglini, Daniele Ercolani, Lucia Sorba, and Fabio Beltram. Manipulation of electron orbitals in hard-wall InAs/InP nanowire quantum dots. *Nano Letters*, 11(4):1695–9, December 2011.

Bibliography

- [166] Lorenzo Romeo, Stefano Roddaro, Alessandro Pitanti, Daniele Ercolani, Lucia Sorba, and Fabio Beltram. Electrostatic spin control in InAs/InP nanowire quantum dots. *Nano Letters*, 12(9):4490–4, August 2012.
- [167] Eduardo J. H. Lee, Xiaocheng Jiang, Ramon Aguado, Giorgos Katsaros, Charles M. Lieber, Silvano De Franceschi, and Silvano De Franceschi. Zero-bias anomaly in a nanowire quantum dot coupled to superconductors. *ArXiv preprint arXiv:1207.1259v1*, July 2012.
- [168] Thomas Sand Jespersen. *Electron Transport in Semiconductor Nanowires and Electrostatic Force Microscopy on Carbon Nanotubes*. PhD thesis, University of Copenhagen, 2007.
- [169] Alessandro Pitanti, Stefano Roddaro, Miriam S. Vitiello, and Alessandro Tredicucci. Contacts shielding in nanowire field effect transistors. *Journal of Applied Physics*, 111(6):064301, March 2012.
- [170] S.A. Dayeh, D.P.R. Aplin, Xiaotian Zhou, P.K.L. Yu, E.T. Yu, and Deli Wang. High Electron Mobility InAs Nanowire Field-Effect Transistors. *Small*, 3(2):326–332, 2007.
- [171] Y Cui, Q Wei, H Park, and C M Lieber. Nanowire nanosensors for highly sensitive and selective detection of biological and chemical species. *Science*, 293(5533):1289–92, August 2001.
- [172] Christian Flindt, A.S. Sørensen, and Karsten Flensberg. Spin-orbit mediated control of spin qubits. *Physical Review Letters*, 97(24):240501, 2006.
- [173] T. Sand-Jespersen, M. Aagesen, C. B. Sørensen, P. E. Lindelof, and J. Nygård. Tunable double dots and Kondo enhanced Andreev transport in InAs nanowires. *Journal of Vacuum Science & Technology B: Microelectronics and Nanometer Structures*, 26(4):1609, 2008.
- [174] L. Hofstetter, A. Geresdi, M. Aagesen, J. Nygård, C. Schönenberger, and S. Csonka. Ferromagnetic Proximity Effect in a Ferromagnet–Quantum-Dot–Superconductor Device. *Physical Review Letters*, 104(24):246804, June 2010.
- [175] Kristian Storm, Gustav Nylund, Lars Samuelson, and Adam P Micolich. Realizing lateral wrap-gated nanowire FETs: controlling gate length with chemistry rather than lithography. *Nano Letters*, 12(1):1–6, January 2012.
- [176] A. Pfund, I. Shorubalko, R. Leturcq, and K. Ensslin. Top-gate defined double quantum dots in InAs nanowires. *Applied Physics Letters*, 89(25):252106, December 2006.
- [177] M. Schroer, K. Petersson, M. Jung, and J. Petta. Field Tuning the g Factor in InAs Nanowire Double Quantum Dots. *Physical Review Letters*, 107(17):176811, October 2011.

-
- [178] S. E. Mohny, Y. Wang, M. A. Cabassi, K. K. Lew, S. Dey, J. M. Redwing, and T. S. Mayer. Measuring the specific contact resistance of contacts to semiconductor nanowires. *Solid-State Electronics*, 49(2):227–232, 2005.
- [179] E. Stern, G. Cheng, M. P. Young, and M. A. Reed. Specific contact resistivity of nanowire devices. *Applied Physics Letters*, 88(5):053106, 2006.
- [180] K. A. Matveev and L. I. Glazman. Coulomb blockade of activated conduction. *Physical Review B*, 54(15):10339–10341, October 1996.
- [181] T. S. Jespersen, M. L. Polianski, C. B. Sørensen, K. Flensberg, and J. Nygård. Mesoscopic conductance fluctuations in InAs nanowire-based SNS junctions. *New Journal of Physics*, 11(11):113025, November 2009.
- [182] S. M. Sze and Kwok K. Ng. *Physics of Semiconductor Devices*. John Wiley & Sons, Inc., Hoboken, NJ, USA, 3rd edition, October 2007.
- [183] É. I. Rau, E. N. Evstaf’eva, and M. V. Andrianov. Mechanisms of charging of insulators under irradiation with medium-energy electron beams. *Physics of the Solid State*, 50(4):621–630, May 2008.
- [184] S. Dueñas, H. Castán, H. García, J. Barbolla, K. Kukli, M. Ritala, and M. Leskelä. Comparative study on electrical properties of atomic layer deposited high-permittivity materials on silicon substrates. *Thin Solid Films*, 474(1-2):222–229, March 2005.
- [185] D. M. Hausmann and R. G. Gordon. Surface morphology and crystallinity control in the atomic layer deposition (ALD) of hafnium and zirconium oxide thin films. *Journal of Crystal Growth*, 249(1-2):251–261, 2003.
- [186] N. V. Nguyen, Albert V. Davydov, Deane Chandler-Horowitz, and Martin M. Frank. Sub-bandgap defect states in polycrystalline hafnium oxide and their suppression by admixture of silicon. *Applied Physics Letters*, 87(19):192903, November 2005.
- [187] Edwin Barnes, J. Kestner, N. T. Nguyen, and S. Das Sarma. Screening of charged impurities with multielectron singlet-triplet spin qubits in quantum dots. *Physical Review B*, 84(23):235309, December 2011.
- [188] L. DiCarlo, H. Lynch, A. Johnson, L. Childress, K. Crockett, C. Marcus, M. Hanson, and A. Gossard. Differential Charge Sensing and Charge Delocalization in a Tunable Double Quantum Dot. *Physical Review Letters*, 92(22):226801, June 2004.
- [189] D. J. Reilly, C. M. Marcus, M. P. Hanson, and A. C. Gossard. Fast single-charge sensing with a rf quantum point contact. *Applied Physics Letters*, 91(16):162101, 2007.

Bibliography

- [190] D. Goldhaber-Gordon, Hadas Shtrikman, D. Mahalu, David Abusch-Magder, U. Meirav, and M. A. Kastner. Kondo effect in a single-electron transistor. *Nature*, 391(6663):156–159, January 1998.
- [191] M Stopa and C M Marcus. Magnetic field control of exchange and noise immunity in double quantum dots. *Nano Letters*, 8(6):1778–82, June 2008.
- [192] K. Petersson, J. Petta, H. Lu, and A. Gossard. Quantum Coherence in a One-Electron Semiconductor Charge Qubit. *Physical Review Letters*, 105(24):246804, December 2010.
- [193] Erik Nielsen, Ralph Young, Richard Muller, and M. Carroll. Implications of simultaneous requirements for low-noise exchange gates in double quantum dots. *Physical Review B*, 82(7):075319, August 2010.
- [194] Shuo Yang and S. Das Sarma. Low-noise conditional operation of singlet-triplet coupled quantum dot qubits. *Physical Review B*, 84(12):121306, September 2011.
- [195] Erik Nielsen, Richard Muller, and Malcolm Carroll. Configuration interaction calculations of the controlled phase gate in double quantum dot qubits. *Physical Review B*, 85(3):035319, January 2012.
- [196] David P. DiVincenzo. Topics in Quantum Computers. In L. L. Sohn, L. P. Kouwenhoven, and G. Schön, editors, *Mesoscopic Electron Transport*. Kluwer, December 1996.
- [197] Serguei Vorojtsov, Eduardo Mucciolo, and Harold Baranger. Spin qubits in multi-electron quantum dots. *Physical Review B*, 69(11):115329, March 2004.
- [198] L.P. Kouwenhoven, DG Austing, and S Tarucha. Few-electron quantum dots. *Reports on Progress in Physics*, 64:701, 2001.
- [199] S.M. Reimann and Matti Manninen. Electronic structure of quantum dots. *Reviews of Modern Physics*, 74(4):1283, 2002.
- [200] S Tarucha, D G Austing, T Honda, R. J. van der Hage, and L. P. Kouwenhoven. Shell Filling and Spin Effects in a Few Electron Quantum Dot. *Physical Review Letters*, 77(17):3613–3616, 1996.
- [201] L H Willems van Beveren, R Hanson, I T Vink, F H L Koppens, L P Kouwenhoven, and L M K Vandersypen. Spin filling of a quantum dot derived from excited-state spectroscopy. *New Journal of Physics*, 7(1):182–182, August 2005.
- [202] Y. Alhassid. The statistical theory of quantum dots. *Reviews of Modern Physics*, 72(4):895–968, October 2000.

-
- [203] M Ciorga, AS Sachrajda, P Hawrylak, C Gould, P Zawadzki, S Jullian, Y Feng, and Z Wasilewski. Addition spectrum of a lateral dot from Coulomb and spin-blockade spectroscopy. *Physical Review B*, 61(24):16315–16318, 2000.
- [204] DR Stewart, D Sprinzak, CM Marcus, CI Duruöz, and J.S. Harris Jr. Correlations between ground and excited state spectra of a quantum dot. *Science*, 278(5344):1784–1788, 1997.
- [205] H Jeong, A M Chang, and M R Melloch. The Kondo effect in an artificial quantum dot molecule. *Science*, 293(5538):2221, October 2001.
- [206] D.G. Austing, T. Honda, K. Muraki, Y. Tokura, and S. Tarucha. Quantum dot molecules. *Physica B: Condensed Matter*, 249-251:206–209, June 1998.
- [207] Duncan R. Stewart. *Level Spectroscopy of a Quantum Dot*. PhD thesis, Stanford University, March 1999.
- [208] E A Laird, J R Petta, Alexander Comstock Johnson, C M Marcus, A Yacoby, M P Hanson, and A C Gossard. Effect of exchange interaction on spin dephasing in a double quantum dot. *Physical Review Letters*, 97(5):56801, 2006.
- [209] M. T. Björk, B. J. Ohlsson, T. Sass, A. I. Persson, C. Thelander, M. H. Magnusson, K. Deppert, L. R. Wallenberg, and L. Samuelson. One-dimensional Steeplechase for Electrons Realized. *Nano Letters*, 2(2):87–89, February 2002.
- [210] Kimberly A Dick, Claes Thelander, Lars Samuelson, and Philippe Caroff. Crystal phase engineering in single InAs nanowires. *Nano Letters*, 10(9):3494–9, September 2010.
- [211] Theodore Choi, Ivan Shorubalko, Simon Gustavsson, Silke Schön, and Klaus Ensslin. Correlated counting of single electrons in a nanowire double quantum dot. *New Journal of Physics*, 11(1):013005, January 2009.
- [212] Vivekanand Bhatt and Sudhir Chandra. Silicon Nitride Films Deposited by RF Sputtering for Microstructure Fabrication in MEMS. *Journal of Electronic Materials*, 38(9):1979–1989, June 2009.
- [213] H. Gleskova, S. Wagner, V. Gašparik, and P. Kováč. Low-temperature silicon nitride for thin-film electronics on polyimide foil substrates. *Applied Surface Science*, 175-176:12–16, May 2001.
- [214] Mircea Trif, Vitaly N. Golovach, and Daniel Loss. Spin dynamics in InAs nanowire quantum dots coupled to a transmission line. *Physical Review B*, 77(4):045434, January 2008.
- [215] Xuedong Hu, Yu-xi Liu, and Franco Nori. Strong coupling of a spin qubit to a superconducting stripline cavity. *Physical Review B*, 86(3):035314, July 2012.

Bibliography

- [216] Alexandre Blais, Ren-Shou Huang, Andreas Wallraff, S. Girvin, and R. Schoelkopf. Cavity quantum electrodynamics for superconducting electrical circuits: An architecture for quantum computation. *Physical Review A*, 69(6):1–14, June 2004.
- [217] R J Schoelkopf and S M Girvin. Wiring up quantum systems. *Nature*, 451(7179): 664–9, February 2008.
- [218] T. Frey, P. Leek, M. Beck, A. Blais, T. Ihn, K. Ensslin, and A. Wallraff. Dipole Coupling of a Double Quantum Dot to a Microwave Resonator. *Physical Review Letters*, 108(4), January 2012.
- [219] M. Delbecq, V. Schmitt, F. Parmentier, N. Roch, J. Viennot, G. Fève, B. Huard, C. Mora, A. Cottet, and T. Kontos. Coupling a Quantum Dot, Fermionic Leads, and a Microwave Cavity on a Chip. *Physical Review Letters*, 107(25):1–5, December 2011.
- [220] R.C. Richardson and E.N. Smith. *Experimental techniques in condensed matter physics at low temperatures*. Westview Press, 1998.
- [221] Frank Pobell. *Matter and methods at low temperatures*. Springer Verlag, Berlin, third edition, 2007.
- [222] Leonardo Di Carlo. *Mesoscopic Electronics Beyond DC Transport*. PhD thesis, Harvard University, 2007.
- [223] David M Pozar. *Microwave engineering*. John Wiley & Sons, Inc., third edition, 2005.
- [224] Hugh Olen Hill Churchill. *Quantum Dots in Gated Nanowires and Nanotubes*. PhD thesis, Harvard University, 2012.
- [225] Coax Co. Ltd. SC-219 series, <http://www.coax.co.jp/english/semi/219.html>, 2010.
- [226] S Weinreb, J Bardin, H Mani, and G Jones. Matched wideband low-noise amplifiers for radio astronomy. *Review of Scientific Instruments*, 80(4):044702, April 2009.
- [227] C. Barthel, D. Reilly, C. Marcus, M. Hanson, and A. Gossard. Rapid Single-Shot Measurement of a Singlet-Triplet Qubit. *Physical Review Letters*, 103(16):160503, October 2009.
- [228] R. J. Schoelkopf, P Wahlgren, A. A. Kozhevnikov, P Delsing, and D. E. Prober. The radio-frequency single-electron transistor (RF-SET): A fast and ultrasensitive electrometer. *Science*, 280(5367):1238–42, May 1998.
- [229] T. R. Stevenson, F. A. Pellerano, C. M. Stahle, K. Aidala, and R. J. Schoelkopf. Multiplexing of radio-frequency single-electron transistors. *Applied Physics Letters*, 80(16):3012, April 2002.